Petrophysical Characterization of the Jo Mill Submarine Fan Complex, Spraberry Trend,

Midland Basin, Texas

By:

Benjamin Frederic Rogers

Presented to the Faculty of the Graduate School of

The University of Texas at Arlington

of the Requirement

for the Degree of

MASTER OF SCIENCE IN

Geology

THE UNIVERSITY OF TEXAS AT ARLINGTON

November 2017

Acknowledgements

Abstract

Petrophysical Characterization of the Jo Mill Submarine Fan Complex, Spraberry Trend,

Midland Basin, Texas.

Ben Rogers, MS

The University of Texas at Arlington, 2017

Supervising Professor: Dr. Qinhong Hu

Understanding and quantifying reservoir quality require a new suite of knowledge when approaching the nanometer sized pore-networks of unconventional reservoirs. These low porosity and permeability reservoirs have been produced in major basins all over the world, but characterizing their pore networks has been fairly recent in its application. One of the challenges of quantifying reservoir characteristics like porosity, pore size distribution, permeability, and tortuosity in unconventional reservoirs is the abundance of their nanometer-sized pore systems. Pore systems in these rocks tend to behave differently and with less predictability than the conventional reservoir. The Spraberry Formation in the Midland Basin of West Texas has become one of the world's leading unconventional plays, especially when coupled with the underlying Wolfcamp Formation. The pore systems in the Spraberry Formation lead to steep production decline and low sweep efficiency. Samples from the lower Spraberry, in a zone known as the Jo Mill submarine fan complex, were taken to better understand these pore systems and to quantify their characteristics. Four samples of various lithological and organic matter properties, but of close stratigraphic relation to the Jo Mill zone in the

Nobles 3202 well in Midland County, Texas, were analyzed. The methodologies used to investigate these nanometer sized pore systems were developed in an attempt to quantify properties such as porosity, pore size distribution, permeability and tortuosity, and their relation to hydrocarbon presence and mineralogy. The tests used included x-ray diffraction, pyrolysis and total organic carbon (TOC), helium porosity and permeability, mercury intrusion porosimetry, low-pressure nitrogen physisorption, contact angle analysis, fluid imbibition, and well logging analysis for porosity, TOC, and water saturation.

The variety of sample size and the diversity of experimentation conducted are the keys to investigating the complex nature of the pore networks in the Jo Mill zone. The samples taken with various lithology and organic matter content give insight to a multitude of pore systems that can occur in the Jo Mill zone. The petrophysical properties of this unconventional reservoir are the foundation for understanding the behavior of fluid movement within its pores. Results from each experiment shed light on the benefits and precautions of certain methods. Overall, the Jo Mill samples exhibit quantifiable correlations between pore size distribution, porosity, and permeability with grain size distribution, lithofacies, and TOC.

Table of Contents

List of Illustrations

List of Tables

Chapter 1. Introduction

The Spraberry Formation has been at the center of major investigation ever since its discovery in 1949. The Spraberry covers an area of more than 25,000 square miles (64,000 sq. km) including six counties (Lorenz et al., 2002) (Figs. 1-1 and 1-2). This formation contains a variety of lithological units and displays northeast-trending structural tendencies, characteristic of its previous tectonic influences. The Spraberry Formation has yielded more than 1.5 billion barrels (bbl) of cumulative oil production since its discovery (EIA, 2013). The Spraberry has an estimated 6 to 10 billion bbl of original oil in place (OOIP), an average formation pressure of 800-900 psi, and average matrix porosities of 6-15%, and an estimated ultimate recovery factor of 10-15%, (Lorenz et al., 2002). These low recovery factors and average matrix permeability of typically < 0.1 md (Mohan and Leonard, 2013) can be attributed to the fine grain size, high quartz and dolomite cement, and presence of pore-bridging clay minerals such as chlorite and illite that are typical of Spraberry Formation mineral composition (Montgomery et al., 2000). While technological advances in recovery techniques have improved the Spraberry Formation. performance, the challenge that continues to persist is the mobilization of oil from this low permeability matrix (Montgomery et al., 2000).

This difference in lithology creates different zones within the Spraberry Formation that are economically attractive in their respective ways. As far as the source of the hydrocarbons in the Spraberry Formation, there has been studies to suggest that the oils in the Spraberry are from more mature sources, but also that the Spraberry shales exhibit source rock characteristics themselves (Scott and Hussain, 1988). Whether or not the source of mature hydrocarbons in the Spraberry is autochthonous may affect the

pore pressure and pore types (Guevara, 1988). The overall play potential is enhanced by the prevalence of naturally fractured zones within the formation, which help offset this low matrix permeability.

The specific zone of the Spraberry Formation that will be addressed in this study is the Jo Mill zone, a submarine fan complex in the Lower Spraberry. The cored interval is from the Jo Mill zone of the Nobles 3202 well within the Nobles lease in Midland County, Texas. The Nobles lease has a production history beginning in 2008, with an average production of 89.01 bbl/d of oil and 86.03 mcf/d of gas (Table 1-1). The Jo Mill field, which is located comparatively closer to the Northern shelf of the Midland Basin, has yielded a cumulative production of more than 150 million bbl (Fig. 1-3). This field is separate from the rest of the Spraberry Trend Area, and is the 42nd largest oil field in the Permian Basin (RRC, 2013). Meanwhile, the Spraberry Trend Area, as a whole, is ranked as the fourth largest in the Permian Basin with a cumulative production of more than 1.5 billion bbl (RRC, 2013) (Fig. 1-3).

One of the very first steps in understanding the attractiveness and the potential of an oil play is quantifying the petrophysical attributes of the zone in question. This is because the production, especially in the Spraberry Formation, is heavily influenced by secondary migration and fluid transport from the matrix to the fracture network. Properties such as porosity and permeability are the driving factors that characterize the behavior of reservoir production. These properties can be better understood by investigating the mineralogy, total organic content (TOC) and maturity, fluid affinity, pore connectivity and size distribution (found using mercury porosimetry, and gas physisorption), and fluid imbibition rates of the rock. Different techniques need to be

used to quantify these properties, as there are many strengths and weaknesses to different experiments.
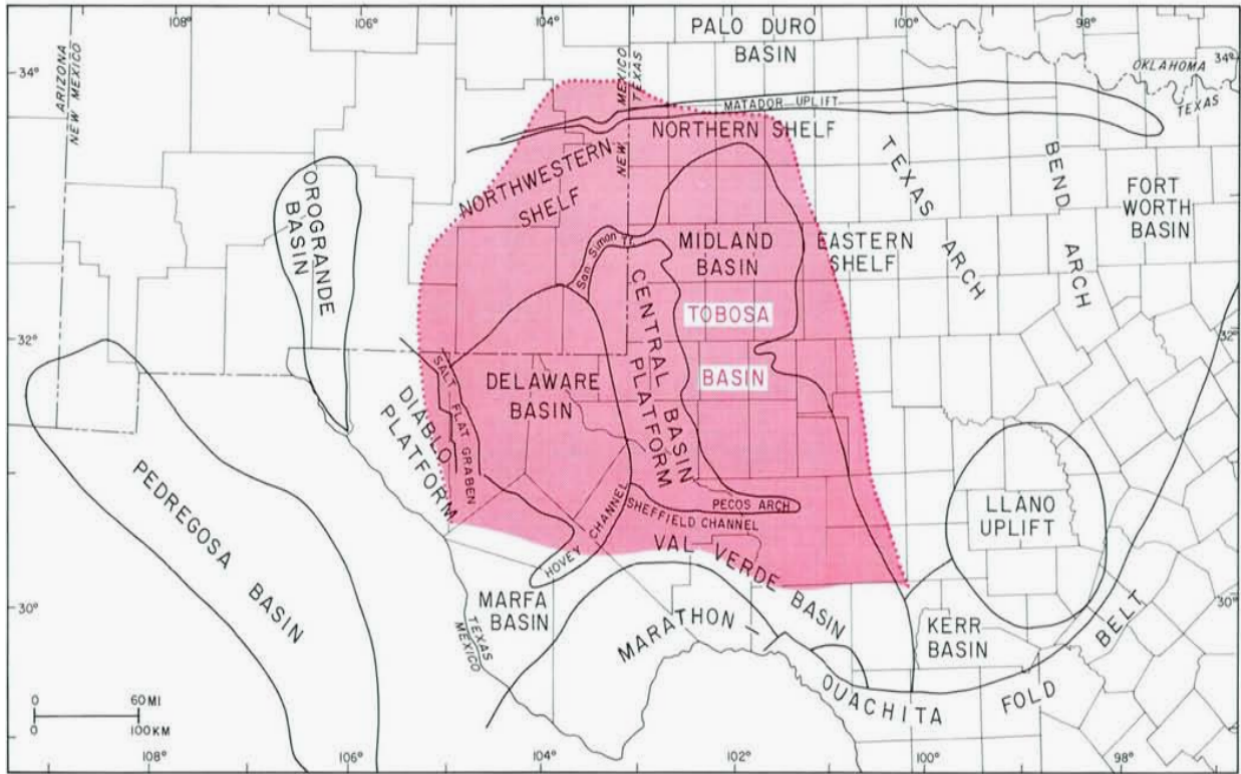
Figure 1-1 Regional structure map of the Permian Basin (from Sloss, 1988).
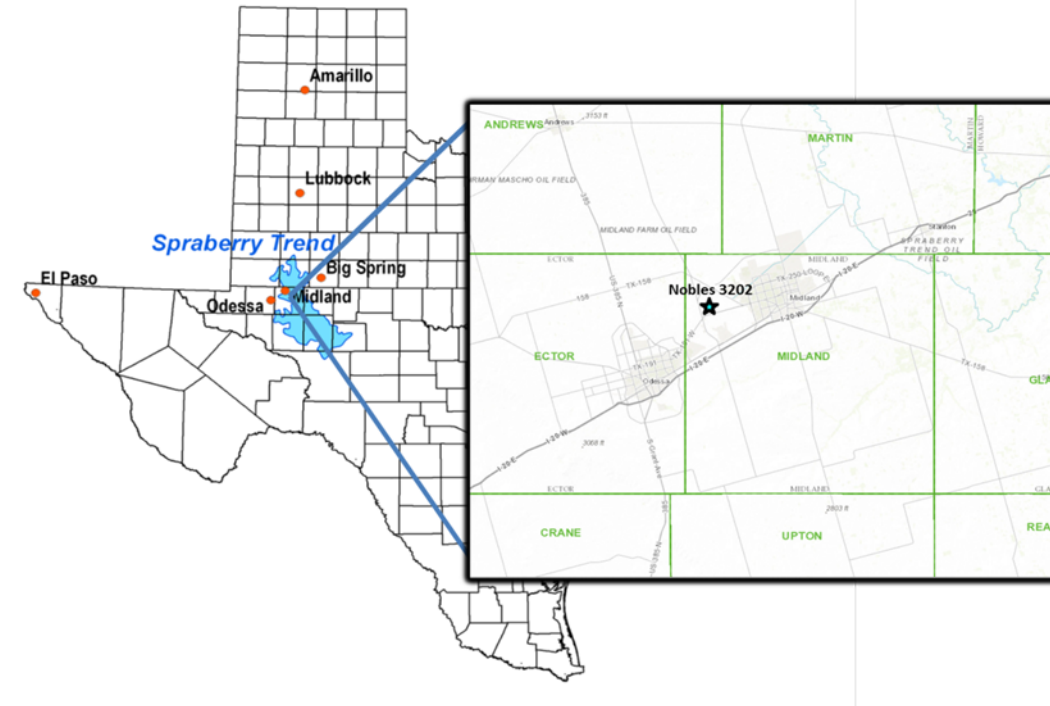
Figure 1-2 Study area of Nobles 3202 Well, Midland County, TX.
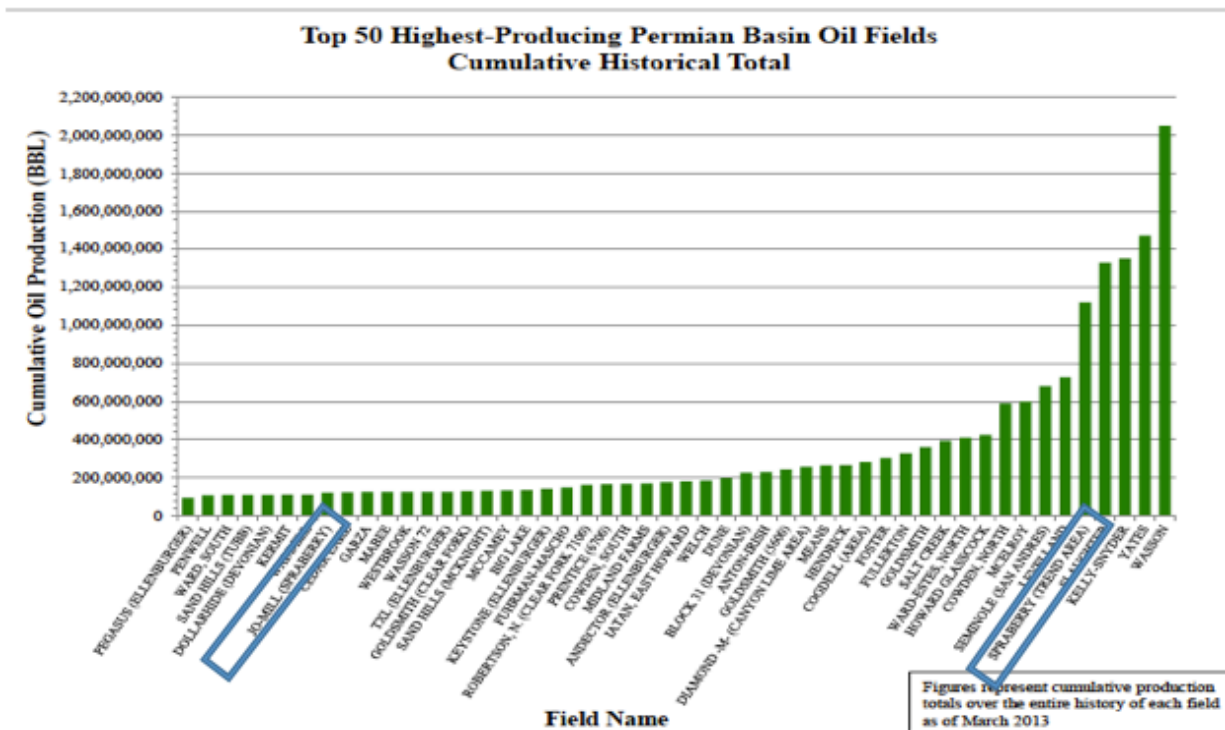
Figure 1-3 Railroad Commission of Texas cumulative oil production statistics by March 2013.

Table 1-1 Annual production history of the Nobles lease, Midland Co., TX (from DrillingInfo, 12017).

Nobles Lease Production					Nobles 3202		
Production Year	Avg. Bbls/month	Annual Bbls	Avg. Mcf/Month	Annual Mcf	Well Completion	Well-Stimulation	Depth Stimulated
2008	2,706	8,118	2,615	7,846	10/1/08	-	-
2009	20,994	251,931	24,524	294,284	-	-	-
2010	48,886	586,627	75,672	908,064	-	-	-
2011	38,007	456,081	76,392	916,708	-	10/5/11	8240'-10750'
2012	38,839	466,064	81,515	978,178	-	-	-
2013	24,856	298,266	61,601	739,209	-	-	-
2014	24,042	288,499	47,549	570,592	-	-	-
2015	27,317	327,799	35,451	425,417	-	-	-
2016	71,639	859,664	90,219	1,082,626	-	-	-
2017	91,459	640,212	124,895	874,266	-	-	-
Cumulative Production	-	4,183,261	-	6,797,190	-	-	-

Chapter 2. Geologic Setting

The study area (Fig. 1-2) is located close to the center of the Spraberry Trend in Midland County, Texas. The Spraberry Formation is a stratigraphic unit of the Permian Basin, which includes three structurally and stratigraphically unique areas, including the Delaware Basin, Central Basin Platform and Midland Basin, respectively, from west to east (Fig. 1-1, Fig. 2-1). The separation and formation of the Midland and Delaware basins was initiated by the rise of a Pennsylvanian median ridge, or uplifted basement block, from the lower lying Tobosa Basin (Adams, 1965) (Hoak et al., 1998), and this is known as the Central Basin Platform. The Central Basin Platform also provides a

mechanism for deposition, in that it produced carbonate sediments from reef building, that would not have been available in the earlier low-lying Tobosa Basin.

The Delaware Basin is characterized by deeper and wider extent of deposition than the Midland Basin, and this is seen by stratigraphic analysis of the basins' correlating lithological units. The other major features of the Permian Basin that define geographic variability and depositional trends are the Northwestern shelf, which is a northern extension of the Central Basin Platform (Fig. 1-1), and the Horseshoe Atoll, which is a carbonate reef structure that is encompassed by the Midland Basin, and lies to the north of the Spraberry Trend area. The Midland Basin deepens to the west, and the western boundary is defined by the faults and folds associated with the eastern margin of the Central Basin Platform (Hoak et al., 1998).

The Late Cretaceous-early Cenozoic Laramide Orogeny was the only significant tectonic event after the Permian, and has influenced the majority of the fracture networks in the Permian Basin (Lorenz et al., 2002). This orogenic event was the only major deformational influence acting on the Spraberry Formation. This is supported by that the northeastern trends of the Laramide compressional regime match the fracture patterns within the Spraberry (Lorenz et al., 2002).

The Leonardian Spraberry Formation is categorized by pulses of terrigenous clastic input throughout its life (Guevara, 1988), which were controlled dominantly by Leonardian paleobathymetric changes in the Midland Basin. The deposition of this formation alternated between carbonate and siliciclastics. The first Permian deposition is characterized by the outbuilding of carbonate reef structures off the north, east, and western flanks of the Central Basin Platform and Midland Basin (Tyler et al., 1997).

16

These carbonate platforms served as large barriers to deposition of clastic sediment

deeper into the basin. Terrigenous depositional sources were dominant during the Early

Permian to Leonardian age. The sandstone percentage in the Spraberry Formation

shows a general northward thickening and coarsening pattern, first observed by Schmitt

(1954), and later by Handford (1981). It has been suggested these sand grains were

from a northern source (Handford, 1981). The alternating depositional activity was

during middle to late Leonardian time (about 276-271 Ma) (Fig. 2-1), and is responsible

for the variety of lithology throughout the Spraberry Formation.
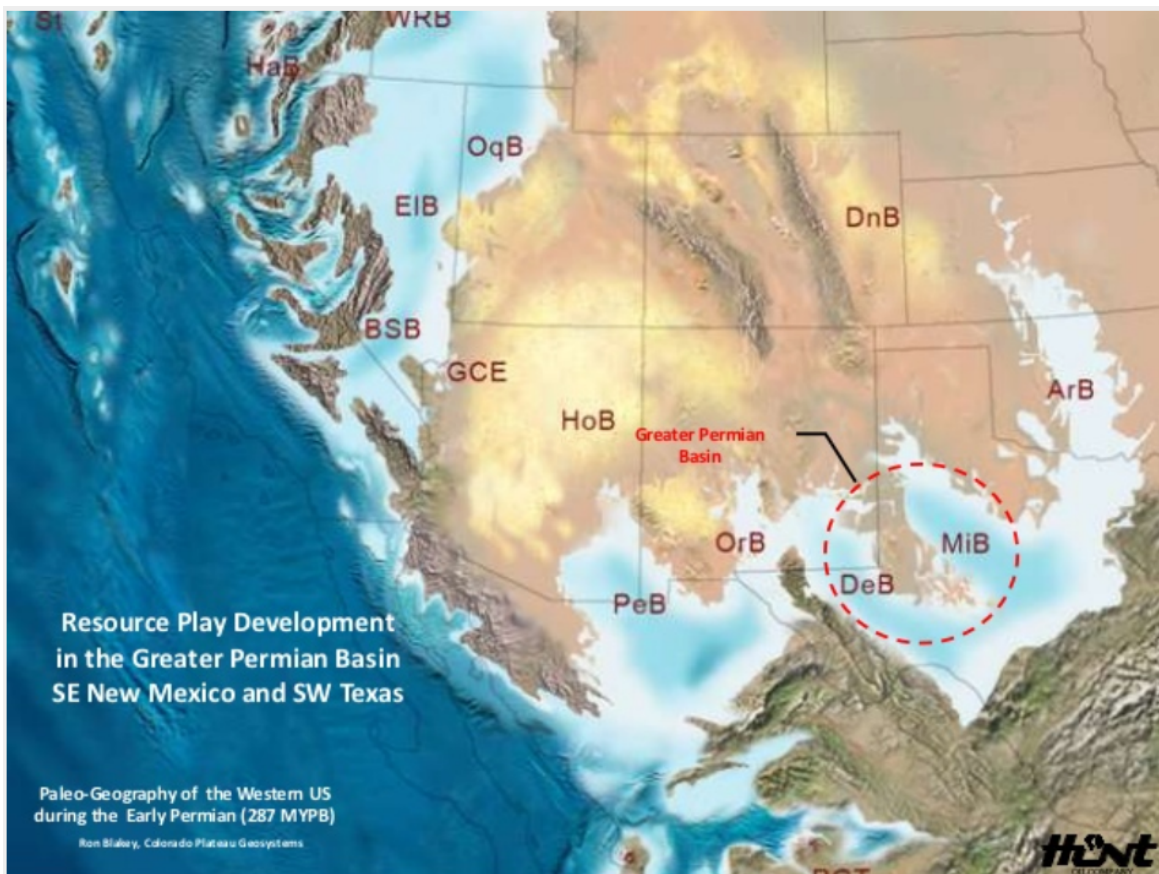
Figure 2-1 Paleogeographic representation of the Permian Basin, Early Permian (~ 290 Ma, from Davies, 2012).

Chapter 3. Stratigraphy

The Spraberry Formation represents a large section of Lower Permian strata in the Midland Basin that lies below Leonard and Glorieta Formations, and is equivalent to, or sometimes below, the Central Basin Platform's Clearfork Formation. The Formation lies above the Dean Sandstone and Wolfcamp Shale in the Midland Basin (Fig. 3-1, Fig. 3-2). The Spraberry is typically broken down into three main units known as the upper, middle, and lower Spraberry Fm., with depths ranging anywhere from 7,000 ft. to 9,000 ft. The Spraberry Formation contains interbedded carbonates, organic-rich mudstones, sandstones, and siltstones. The presence of different lithology depends on the location within the Midland basin, and the environment that was active during the time of deposition. According to Guevara (1988), the lower Spraberry is mainly composed of terrigenous clastics, and that is what is present in the Jo Mill submarine fan complex.
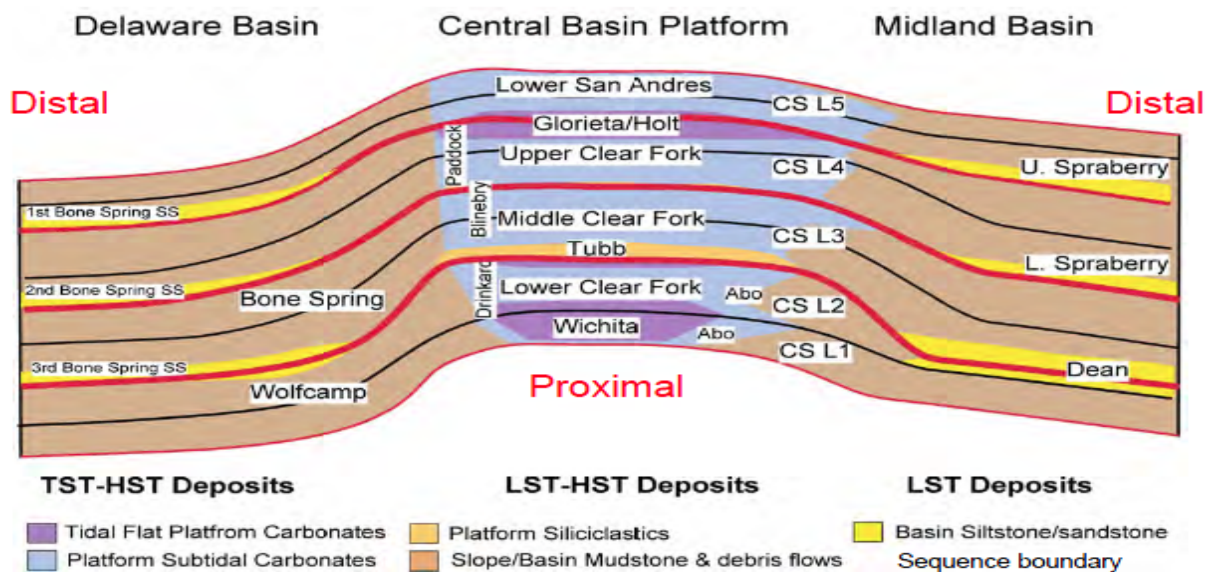
Figure 3-1 Cross-section of the Permian Basin stratigraphic relationships (from Ruppel, 2017).

The sandstones and siltstones of the Spraberry Formation exhibit little compositional or textural variation throughout the Midland Basin, and therefore the lithology can be generalized by four widely occurring lithofacies based on sedimentary structures (Handford, 1981). These lithofacies are massive to parallel and cross-laminated sandstone and siltstone, laminated sandstone and siltstone, bioturbated sandstone and siltstone, and black, organic-rich shale. Carbonate lithofacies are also present, and are in the lower member of the Dean and the basal strata of the Lower and Upper Spraberry Formation. The depositional process of the Lower Spraberry terrigenous clastics includes saline density underflow and interflow currents, turbidity currents (Handford, 1981; Tyler et al., 1997), suspension settling of marine organic matter and airborne silt (Hamlin and Baumgardner, 2012). The entire Spraberry Formation is up to 1,000 ft. thick in some areas of Midland County, which include the study area of this project. The Jo Mill submarine fan system can be up to 120 ft. thick in the same region (Guevara, 1988).

The Lower Spraberry can be divided into different units (Fig. 3-3), depending on the location within the Midland Basin, and can vary between different reports. Within the Lower Spraberry, the Jo Mill submarine fan system can also be subdivided into different units, for example, units 1L-3L (Fig. 3-3) which separate the section based on sandstone and siltstone percentage, as well as upward-fining or upward-coarsening sequences. The Lower Spraberry units 2L-3L, for the Guevara (1988) system, exhibit upward-coarsening sequences and large sandstone and siltstone percentages, while the unit 1L displays an upward-fining sequence. However, the Jo Mill is also classified based on its overall sandstone percentage and its geographic source of sediment (Tyler et al., 1997), and is broken down into genetic units 2L and 1L based on these criteria. In the Nobles 3202

well, the Jo Mill zone exhibits an overlying organic-rich shale interval, underlain by two coarsening-upward sequences (Fig. 4-1). The different units within the Jo Mill represent different environments of deposition, and subsequently different producing intervals, as they have varying petrophysical properties that correlate with their lithologies (Fig. 3-2). Overall, the Lower Spraberry sandstone beds occur at the top of these upward coarsening units 2L and 3L (Guevara, 1988).
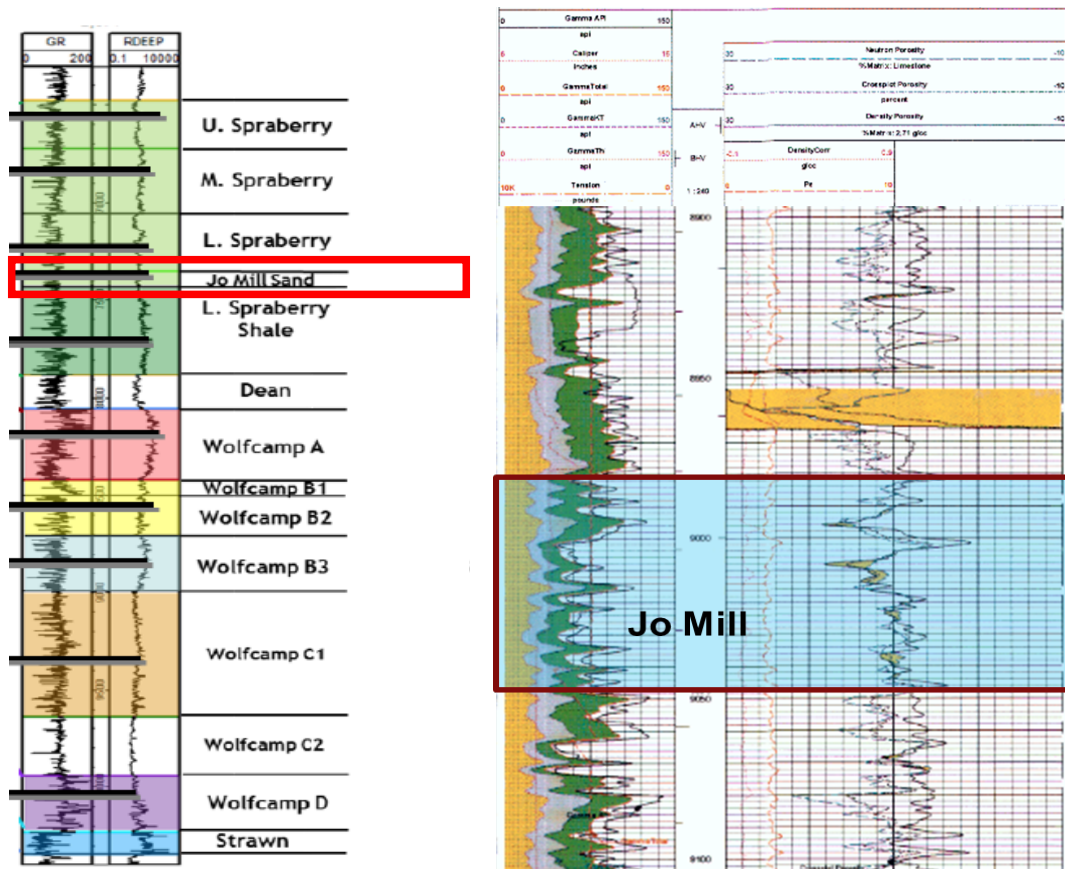
Figure 3-2 Spraberry and Wolfcamp targets in the Midland Basin (modified from Scott et al., 2015) (Left); Nobles 3202 Midland, TX Jo Mill section (8980'MD-9045'MD)(Right).

McLennan and Bradley (1951)	Senning (1951)	Bartley (1951)	Mardock and Myers (1951)	Warn and others (1952)	Wilkinson (1953)	Handford (1981 b,c)	Matchus and Jones (1984)	This Report * **
FIRST SAND ZONE	UPPER SPRABERRY — FLOYD SAND	UPPER SPRABERRY — 1 SAND, 2, 3	UPPER SPRABERRY	UPPER SPRABERRY	UPPER SPRABERRY	UPPER SPRABERRY	FIRST SPRABERRY	UPPER SPRABERRY — 1U (a,b,c), 2U, 3U, 4U, 5U (1), 6U — FLOYD SUBMARINE FAN / DRIVER SUBMARINE FAN
	INTERMEDIATE ZONE	MIDDLE SPRABERRY — FLOYD SAND	MIDDLE SPRABERRY	MIDDLE SPRABERRY	MIDDLE SPRABERRY	MIDDLE SPRABERRY — 4		MIDDLE SPRABERRY — 1M
SECOND SAND ZONE						5		2M, 3M, 4M, 5M
	LOWER SPRABERRY — 1, 2, 3, 4	LOWER SPRABERRY	LOWER SPRABERRY	LOWER SPRABERRY	LOWER SPRABERRY	SECOND SPRABERRY		LOWER SPRABERRY — 1L (r, s), 2L (v), 3L — JO MILL SUBMARINE FAN
	LOWER SPRABERRY							

* Operational unit   ** Sandstone zone

Figure 3-3 Spraberry Formation subdivisions from various literature (from Guevara, 1988).

Chapter 4. Methods

Overview

XTO Energy, Inc. provided the Jo Mill samples from sidewall cores taken from the Nobles 3202 well. The Jo Mill core selections under evaluation (Fig. 4-1) are from depths ranging from 8,987' to 9,030' in the Lower Spraberry section of the Nobles 3202 well in Midland County, Texas. The well is located in a close proximity to the Central Basin Platform, and is in the Northern half of the Midland Basin near the shelf -derived sediment sources identified by Handford (1981) and Schmitt (1954). The four samples were selected (Fig. 4-1) based on their correlation with the lithology and lithofacies described by Handford (1981).

The techniques used in evaluating the Jo Mill section of the Nobles 3202 well are aimed at quantifying the mineralogy, TOC and organic maturity, porosity, pore size distribution, permeability, tortuosity, wettability, and the pore network connectivity of the samples. The methods used were contact angle measurement, X-Ray Diffraction (XRD), permeability and porosity using helium gas, pyrolysis and TOC from Weatherford's Rock-Eval method and the Shimadzu Institute for Research Technology (SIRT), Mercury Injection Capillary Pressure (MICP), spontaneous fluid imbibition, and low-pressure N_2 physisorption. These tests were conducted at multiple locations including the laboratory at the University of Texas at Arlington (GS Rm. 124), and the Shimadzu Institute for Research Technologies (SIRT) at The University of Texas at Arlington. Collaborating labs in China were the China University of Geosciences (CUG), and the Chengdu University of Technology (CDUT).

Core Description

The Nobles 3202 core is a 66 ft. section from 8980' to 9046' in the Lower Spraberry Jo Mill zone (Fig. 3-2). The core was separated by 1' intervals, and broken into a variety of sizes. The amount of sample taken was anywhere from 470 grams to 1757 grams. The descriptions of the individual samples are as follows:

N8987-S (for sample of 8987' at Nobels well for Spraberry formation): Dark gray to black shale, with few subtle discontinuous laminations of interbedded siltstone. No other sedimentary structures were present. This sample represents a gamma ray peak on the core gamma ray signature (Fig. 4-1).

N8995-S: Dark grey to black shale with finely laminated, interbedded, light grey siltstone. No other sedimentary structures were present. This sample represents a gamma ray peak on the core gamma ray signature (Fig. 4-1).

N9009-S: Dark grey to light grey, coarse to fine siltstone, with fine parallel laminations, moderate to severe bioturbation, and well-sorted grains. This sample represents a gamma ray trough on the core gamma ray signature (Fig. 4-1).

N9029-S: Massive bedded light grey siltstone to very fine sandstone, no bioturbation and well sorted grains. No other sedimentary structures were present. This sample represents a transition zone between a gamma ray peak and trough on the core gamma ray signature (Fig. 4-1).
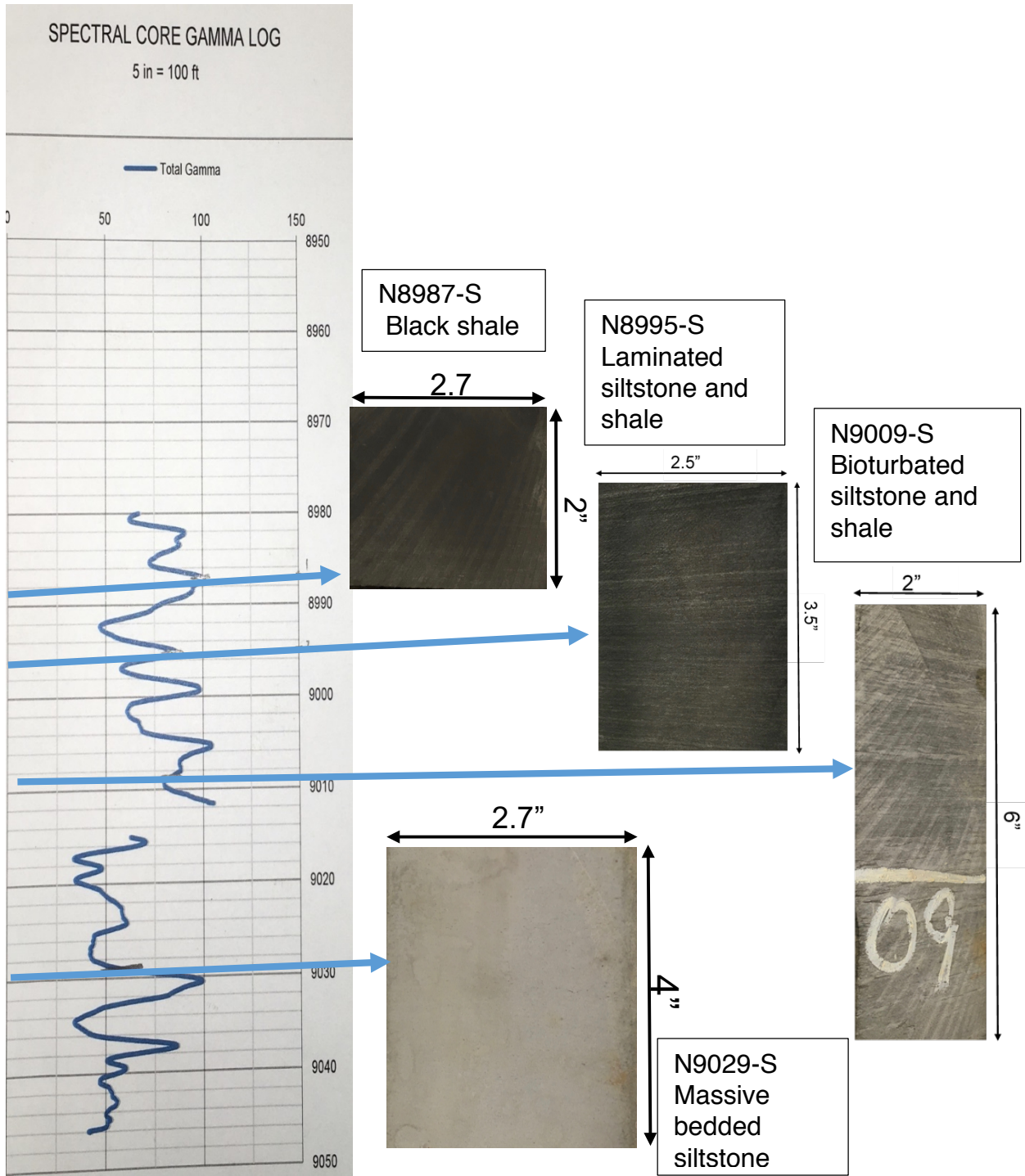
Figure 4-1 Core gamma ray signature of Jo Mill Sandstone, Nobles 3202 (Left); Individual core selections of N8987-S, N8995-S, N9009-S, and N9029-S from top to bottom.

Sample Processing

The samples were taken from the core after a careful analysis of the Spraberry lithology and lithofacies that were present. The amount of sample mass taken was relative to the demands of the individual laboratory tests. Figs. 4-2- and 4-5 represent the various size fractions of the reduced core that were prepared for the helium porosity and permeability, contact angle analysis, mercury intrusion porosimetry, low-pressure N_2 physisorption, XRD, TOC and pyrolysis, respectively.

Figure 4-2 Core plug size fraction 1" x 2" taken from depths 8995 ft. and 9009 ft.
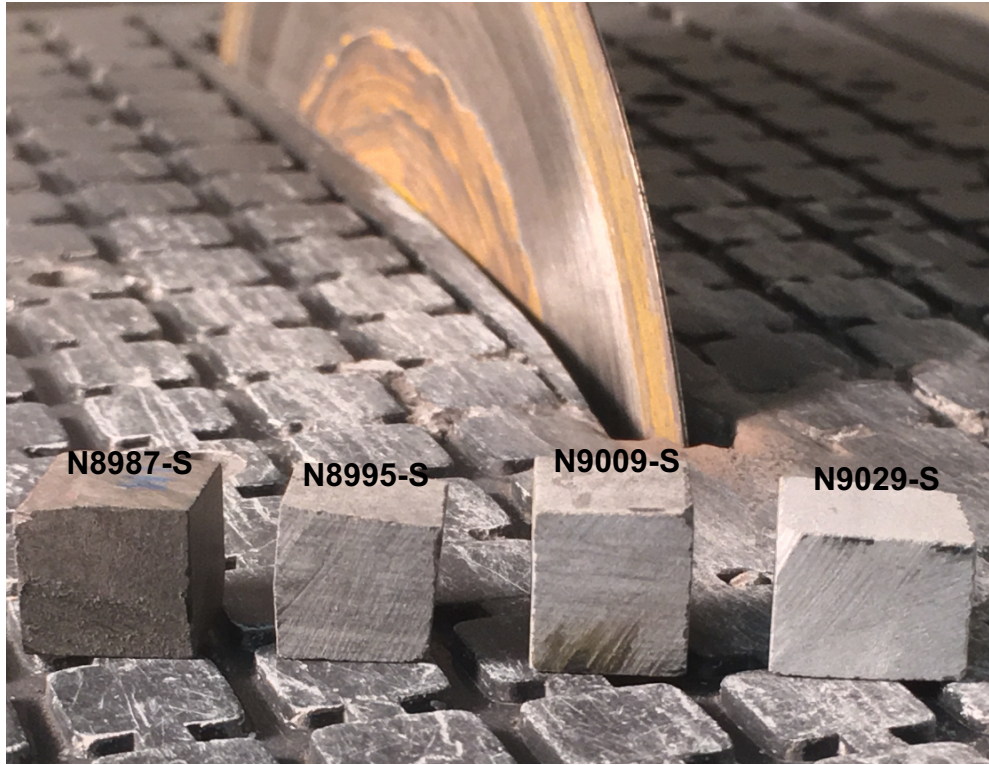
Figure 4-3 Cubic samples of 10mm x 10mm x 10mm.
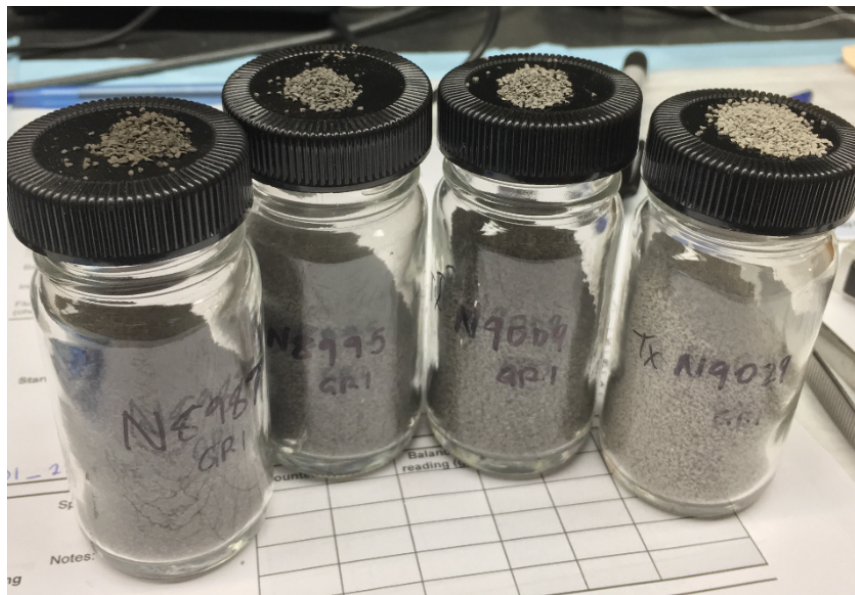
Figure 4-4 Sample size fraction of #20-#35 mesh (500-850 µm).

Figure 4-5 Powder fraction of <#200 mesh (<75 µm).

Mineralogy

The mineralogy analysis was performed using X-ray diffraction (XRD) and sample size of <#200 mesh (<75 µm) (Fig. 4-5) from all four samples. XRD analyses utilized the MaximaX XRD-7000 Shimadzu X-ray Diffractometer at the SIRT (see Appendix A for the procedure). Different intensity peaks correlate to different mineral assemblages, and results in a full profile of mineral percentage that makes up the rock. The data are used to characterize the lithology as described by the sCore classification scheme for organic mudstones (Gamero-Diaz et al., 2012). This is used in conjunction with TOC and pyrolysis data to better understand their effects on the pore structure of the Jo Mill submarine fan complex.

TOC and Pyrolysis

Geochemical analysis for the Nobles 3202 samples includes total organic carbon (TOC) weight percentage and pyrolysis results. Both tests were done using <#200 mesh (<75 μm) sample size (Fig. 4-5). The TOC values were obtained from both the Shimadzu TOC-V$_{ws}$ SSM-5000A instrument (see Appendix B for the procedure) at the SIRT, and the OGE-V instrument (CUG). Pyrolysis data was collected at the CUG using the OGE-V instrument. The SIRT method for TOC analysis involved measuring the inorganic carbon as well as the total carbon and taking the difference of the two (Eq. 1).

$$TOC\% = TC\% - TIC\% \tag{1}$$

The pyrolysis results from the CUG yielded measurements such as T_{max}, S1, S2, and S4 peaks, as well as the TOC percentage of the samples, which was also measured at the SIRT. T_{max} is the temperature at which the maximum release of hydrocarbons from cracking of kerogen during pyrolysis occurs. The S1 peak represents the quantity (in mg hydrocarbon/g rock) of free hydrocarbons (oil and gas) present in the rock, which become volatilized below 300° C. The S2 peak gives the amount of hydrocarbon-type compounds (in mg hydrocarbon/g rock) produced by the cracking of kerogen as the temperature increases to 600° C. This also shows the potential for production of hydrocarbons in this rock should burial and maturation continue. The S3 peak shows the quantity of CO_2 (measured in mg CO_2/g rock) produced from pyrolysis of the organic matter in the rock up to 390° C. The instrument did not record the S3 peak, therefore, it was not included in the analysis. The S4 peak shows the residual hydrocarbon content of the sample; this residual carbon content of sample has little or no potential to generate hydrocarbons due to a lack of hydrogen and

the chemical structure of the molecule. Using the measured pyrolysis values, certain

parameters such as hydrogen index (HI), productivity index (PI), and genetic potential

can be quantified (Eq. 2-4).

$$HI = \frac{S2}{TOC} \tag{2}$$

$$PI = \frac{S1}{(S1+S2)} \tag{3}$$

$$Genetic\ Potential = S1 + S2 \tag{4}$$

These values aid in finding and assessing the kerogen type and maturity of the

samples. The hydrogen index (HI) indirectly determines the ratio of hydrogen to carbon.

The productivity index (PI) characterizes the evolution level of the organic matter.

Genetic potential represents the hydrocarbon generating potential of the rock, and

quantifies the potential for the Spraberry shales to be considered good source rocks.

Other parameters such as oxygen index and the S2-S3 value, which determines organic

matter type in the rock, were not available due to the absence of S3 results from the

analysis.

Wettability

Wettability describes the preference of a solid to be in contact with one fluid rather

than another (Abdallah, 2007). This preference, or balance of surface forces on the

individual grains, is a major force that controls fluid flow into and out of the rock. The

surface is wetting to a specific fluid if the angle at which the fluid contacts the surface falls

within a particular range, and the same is true for non-wetting surfaces as well as partially

wetting surfaces (Fig. 4-6).

A number of different techniques have been used in the past to quantify the wettability of a rock. The contact angle method requires pure fluids and well-prepared surfaces (Thyne, 2013), so that the angle at which the fluid contacts the surface is properly measured. A slab of sample (roughly 10mm x 10mm x 2mm) (Fig. 4-3), with a symmetric and smoothed surface, is used with the Kino SL200KB|KS Optical Dynamic/Static Interfacial Tensiometer & Contact Angle Meter (Fig. 4-7). The Kino instrument measures the angle at which a droplet of one of the four fluids mentioned above encounters the surface (Fig. 4-8). The wettability test is done using deionized (DI) water, API (American Petroleum Institute) brine (8% NaCl and 2% $CaCl_2$ by weight), isopropyl alcohol (IPA) in DI water, and n-decane. The API brine is used to simulate a high salinity formation water along with DI water to simulate a control. The n-decane is used to simulate oil, and the IPA is used as a hydrophobic and hydrophilic control. All of these fluids are used to analyze the sample surface affinity towards different reservoir fluids. The test will determine whether the sample has hydrophobic or hydrophilic tendencies. The Spraberry is known to be weakly hydrophilic, and enhancing this affinity towards water can greatly enhance production techniques (Mohan and Leonard, 2013).
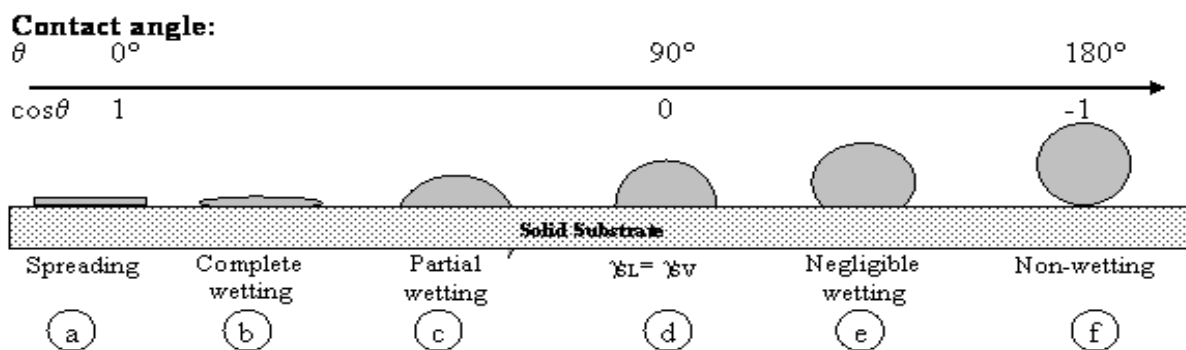
Figure 4-6 Defining contact angle values for wetting and non-wetting surfaces; $\gamma_{SL} = \gamma_{SV}$ represents the solid-liquid and solid-vapor interfacial tensions (from Njobuenwu et al., 2001).
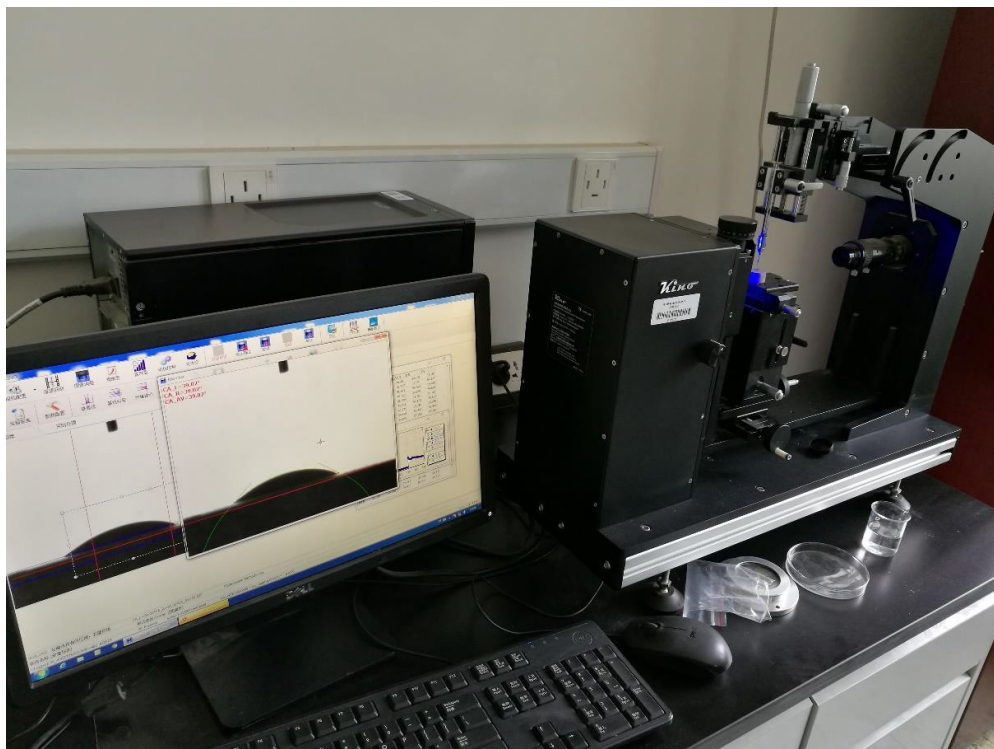
Figure 4-7 Kino SL200KB|KS Optical Dynamic/Static Interfacial Tensiometer & Contact Angle Meter.

CA_L=0.000° CA_R=0.000° CA_AV=0.000°

CA_L=47.611° CA_R=47.611° CA_AV=47.611°
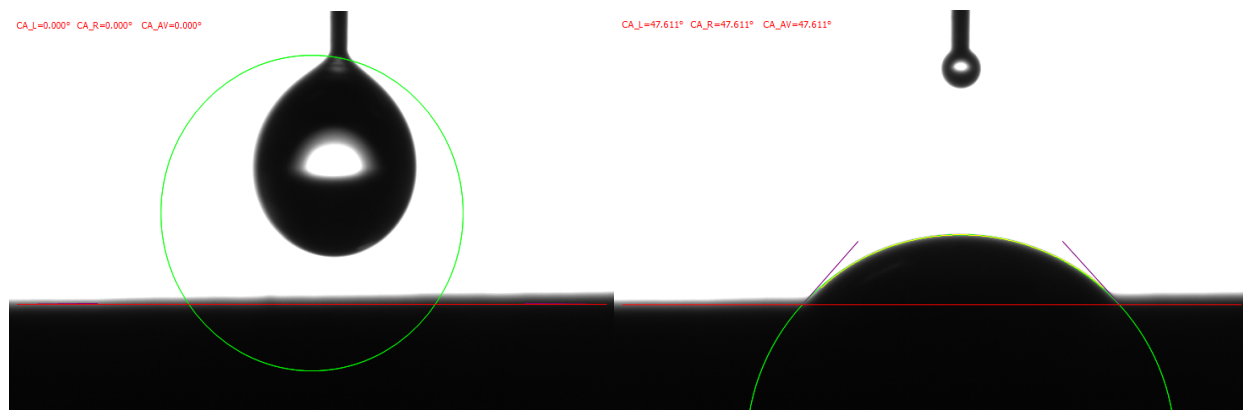
Figure 4-8 Contact angle measurement for DI Water on N8995-S sample.

Helium Porosity and Permeability

The helium porosity and permeability tests were conducted using the CoreTest Systems AP-608 Automated Permeameter-Porosimeter methodology available at CDUT. The analysis used a core plug roughly 2.5 cm in diameter and 4-5 cm in length (Fig. 4-2) from the N8995-S and N9009-S samples, as these were the samples with the most mass and which did not fracture in the process of plugging. The plugs taken were perpendicular to the observed bedding laminations. Using helium gas, the AP-608 methodology utilizes the theory of Boyle's law (Eq. 5) stating that an unknown volume can be determined by expanding a gas of known pressure and temperature condition into a void space of known volume and using the resulting pressure to calculate the unknown volume.

$$V1 = \frac{P2 \times V2}{P1}$$
(5)

Where,

V1= Unknown original volume (cm^3)

V2= Known secondary volume (cm^3)

P1= Known original pressure (psi)

P2= Known secondary pressure (psi)

This instrument has a confining pressure range of 500-9,500 psi, and a pore pressure range of 100-250 psi. The AP-608 measures porosity in a range from 0.1-40% and permeability from 0.001mD to 10,000 mD (Core-Test Systems, Inc., 2012). The overall porosity is obtained using the measured pore volume, and the bulk volume calculated from the measured dimensions of the core plugs. The measured parameters,

in this case, are equivalent gas permeability, pore volume of core sample, and overall porosity.

Low-Pressure Nitrogen Physisorption

The nitrogen adsorption and desorption analysis is carried out as a quantitative approach to understanding the pore surface area and pore size distribution of the rock. Samples were crushed into #20-#35 mesh size (500µm-850µm) (Fig. 4-4) for this experiment to eliminate the effects of micro-fractures in the rock and complete a test within a reasonable period (usually about 24 hrs) for N_2 reaching sample interior. The instrument used for this study is the Quantachrome QuadraSorb SI Pore Size Analyzer at CDUT (Fig. 4-9). In the experiment, pressure is increased as nitrogen condenses on to the smallest pore surfaces first and onto the larger pore surfaces, as the pressure is increased until the entire sample is saturated. As the pressure is decreased, gas evaporates from the system, and an isotherm is recorded from the adsorption and desorption measured. Sing (1985) characterizes the different types of isotherm curves as related to the amounts of micro-, meso-, and macro-pores in porous materials. The hysteresis curves characterized by Sing (1985) are due to the differences in the geometry of the pore structures in the sample. To yield the isotherm from this adsorption and desorption, a model uses the BET (Braunauer-Emmett-Teller) equation, which calculates a surface area's porous material (Sing et al., 1985; Li et al., 2016).

$$\frac{p}{n^a(p^o-p)} = \frac{1}{n_m^a * C} + \frac{(C-1)p}{n_m^a * C p^o} \tag{6}$$

Where,

n^a= Amount adsorbed at the relative pressure p/p^o (mL)

n_m^a= Monolayer capacity (mL)

C= Dimensionless constant, related exponentially to the enthalpy of the adsorption in the first adsorbed layer.

In this case, C is not used as a quantitative measurement of enthalpy, but an indication of the magnitude of the energy released during the interaction (Sing et al., 1985).

Figure 4-9 Quantachrome QuadraSorb SI Pore Size Analyzer.

Mercury Injection Capillary Pressure (MICP)

Capable of investigating the pore-throat size down to 2.8 nm, MICP measures the bulk density, particle density, porosity, pore throat size distribution, pore surface area, permeability, and tortuosity. The test uses 10mm x 10mm x 10mm cubes of each sample (Fig. 4-3). MIP analysis is achieved using an Autopore IV 9510 Automatic Mercury

Porosimeter (Micromeritics, Norcross, GA) (Fig. 4-10). The MIP method uses the relationship of capillary pressure within pore spaces to the intrusion of a non-wetting fluid. E.W. Washburn first quantified this relationship in 1921.

The Washburn equation (Eq. 7) relates pressure and pore throat size, finding that the diameter of the pore invaded by a non-wetting fluid is inversely proportional to the applied pressure; the higher the pressure applied, the smaller the pores invaded by the non-wetting fluid (Washburn, 1921; Gao and Hu, 2012). The reason why a non-wetting fluid is used, such as mercury, is to ensure that only when pressure is applied, does the fluid invade the medium. Washburn's relationship of mercury pressures to pore throat diameters is illustrated in Equation 7.

$$\Delta P = -\frac{2\gamma cos\theta}{R} \qquad (7)$$

Where,

ΔP= Pressure difference across the mercury interface (psia)

γ= Surface tension for mercury (dynes/cm)

θ= Contact angle between the mercury and the porous media (degrees)

R= Radius of the pore throat (cm)

This equation can also be modified to account for variable contact angle and surface tensions that may be critical for nano-sized pores (Wang et al., 2016) (Eq. 8).

$$\Delta P = -\frac{2\gamma_{Hg}(R)cos\theta_{Hg}(R)}{R} \qquad (8)$$

Where,

γ_{Hg}= Liquid-vapor surface tension of the mercury droplets, as a function of R (dynes/cm)

θ_{Hg}= Contact angle as a function of R (degrees)

Equation 8 is based on the assumption that all the pores are cylindrical, which is not always the case (Gao and Hu, 2013).

The permeability of the sample can also be quantified from the following equation (Eq. 9), developed by Katz and Thompson (1986).

$$\kappa = \frac{1}{89} (L_{max})^2 \left(\frac{L_{max}}{L_C}\right) \phi S(L_{max}) \tag{9}$$

Where,

κ= Air permeability (m^2)

L_{max}= Pore-throat diameter where hydraulic conductance is a maximum (µm)

L_C= Pore throat diameter at the threshold pressure (µm)

ϕ= Porosity (fraction)

$S(L_{max})$= Mercury saturation at L$_{max}$ (fraction) (Gao and Hu, 2013).

MICP also generates the value of tortuosity by Equation 10 developed by Hager (1998).

$$\tau = \sqrt{\frac{p}{24k(1+pV_T)}} \int_{n=r_{c,min}}^{n=r_{c,max}} n^2 f_v(n) dn \tag{10}$$

Where,

τ= Tortuoisty (dimensionless)

p= Sample density (g/cm^3)

V_T= Total pore volume (mL/g)

r_c, max= Maximum detectable capillary radius for MIP (µm)

r_c, min= Minimum detectable capillary radius for MIP (µm)

$\int_{n=r_{c,min}}^{n=r_{c,max}} n^2 f_v(n) dn$= Pore throat volume probability density function (Hager, 1998)

Figure 4-10 Micromeritics Autopore IV 9510.

Spontaneous Fluid Imbibition

Spontaneous imbibition is the process by which the non-wetting fluid in a porous medium is displaced by a wetting fluid due to capillary forces (Gao and Hu, 2012). The variables such as the porosity, permeability, initial saturation, surface tension, fluid viscosities, and capillary pressure all affect the imbibition process. The analysis measures the quantity and the rate of liquid (in this case, DI water and n-decane) imbibed into the Nobles 3202 samples. The test utilizes the apparatus shown in Fig. 4-11. The

sample was suspended and attached to a Shimadzu AUW220D analytical balance (Fig. 4-11), which has a precision of 0.1 mg (UniBloc Analytical Balances Brochure, 2014). The exposed face of the sample is lowered into contact with the solution and the balance records the weight change over time at specified intervals. Spontaneous fluid imbibition uses fluids such as n-decane, and DI water that are imbibed into the 10mm x 10mm x 10mm-sized cubes (Fig. 4-3), each having epoxied sides, allowing the fluid movement to be observed in the direction parallel to laminations.
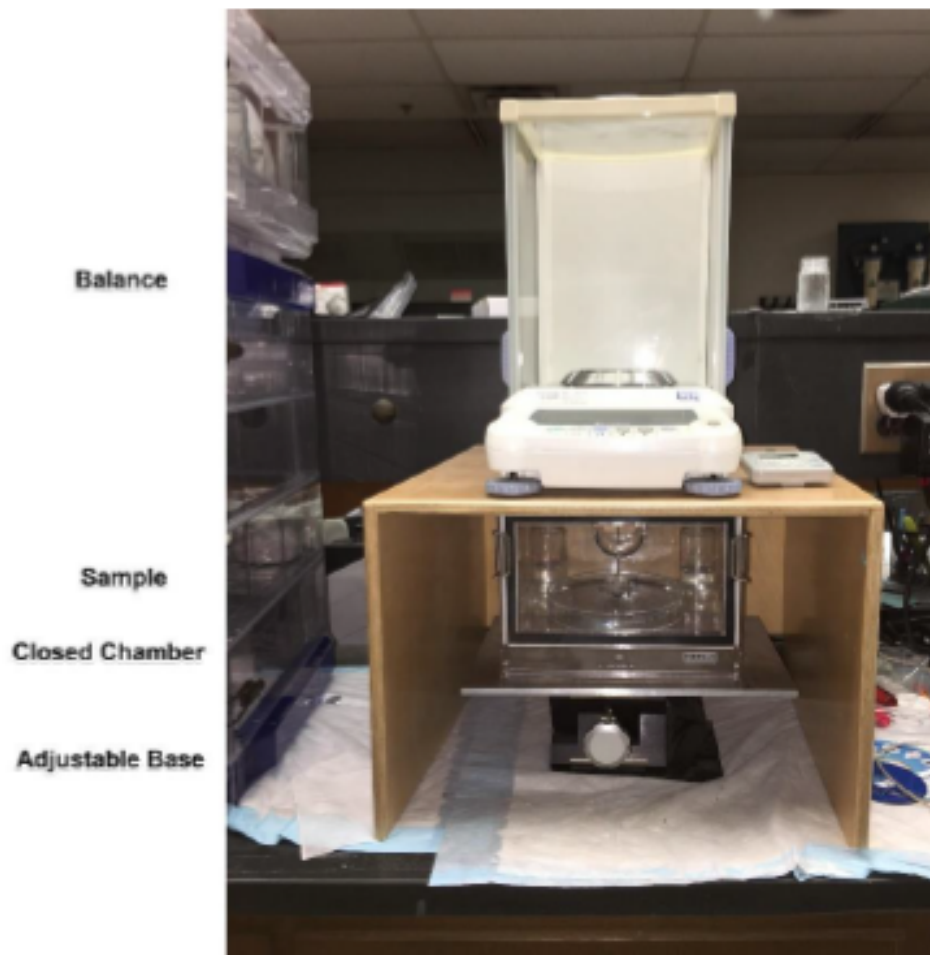
Figure 4-11 Imbibition/Vapor Absorption Test Setup; Shimadzu AUW220D Analytical Balance.

The quantitative imbibition can be expressed by plotting the cumulative imbibition vs. time (Eq. 11).

$$I(t) = St^{0.5} + At \qquad (11)$$

Where,

$I(t)$= Cumulative imbibition (m)

t= Time (s)

S= Sorptivity (m/s$^{0.5}$)

A= Empirically derived constant that is related to gravitational force

The constant A can be negligible when the sample length (0.9-1.0 cm) is less than the "sorptive length", due to the fact that the gravity potential gradient is less than the matrix potential gradient (Hu et al., 2001; Philip, 1957). Sorptivity, which is a function of the initial and boundary water contents, is the parameter that quantifies the rate of imbibition and is controlled by both capillary pressure and permeability (Hu et al., 2001).

A predicted permeability can also be obtained using the spontaneous imbibition method. This is done using the relationship, found by Kao and Hunt (1996) and Tokunaga and Wan (2001), between the wettability and sorptivity. When a medium has a perfect wettability to an imbibing fluid, there is seen a one-fourth power relationship between the permeability and the effective wetted distance (Kao and Hunt, 1996; Tokunaga and Wan, 2001). The advancement of the wetting front is shown by the slope of the log cumulative imbibition versus the log time and thus characterizes the connectivity of the pores. In rocks with low pore connectivity, the wetting front advances as approximately one-fourth

the power of time, and in rocks with well-connected pores, the wetting front advances with

the square-root-of time (t) (Eq. 11) (Hu et al., 2012).

Well Log Analysis

One of the first considerations in the log analysis that needs to be accounted for

is the fact that the gamma ray log taken from the core is offset by about 10 ft., when

compared to the wireline log section for the rest of the formation. The peaks and

troughs of the core gamma ray log were correlated to match the main log suite in Fig. 4-

12, and the samples were taken in correlation with the core gamma ray signature.
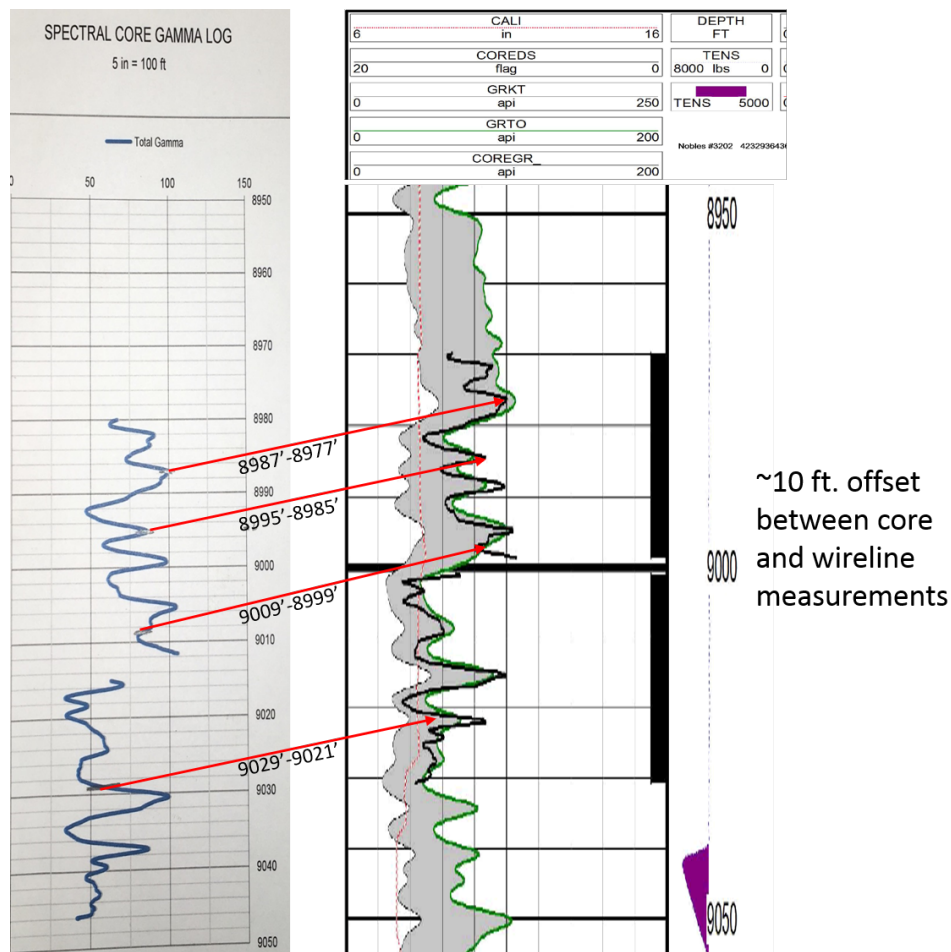
Figure 4-12 Offset correlation between direct core measurement and wireline measurement.

Well logging provides valuable insight into the rock properties at borehole conditions by directly measuring various characteristics. The suite of logs run on the Nobles 3202 well include gamma ray, spectral core gamma ray, shallow and deep resistivity logs and micro-spherically focused resistivity, neutron-density and bulk density, sonic time, and density and neutron porosity. These measurements are based on known physical and chemical relationships between the rock and the fluids that are inherent in the formation as well as the fluid used in the drilling operations. From the log measurements mentioned above, further characteristics can be quantified using various equations that have been developed over the years. Properties relating to the experiments in this study such as porosity, water saturation, and even TOC can be calculated from the log measurements. Rock properties from log analysis give insight into the various ways that one can come to these conclusions, and give the ability to analyze which source of analysis is the most useful for interpretation. All logs for the Nobles 3202 well were provided by XTO Energy and evaluated using the Petra licenses given to the University of Texas at Arlington.

The density-neutron porosity curves are the first method of quantifying the porosity of the formation. These curves are both run on a limestone matrix of 2.71 g/cm^3, which is common when logging in West Texas. However, this can be the cause of overestimating or underestimating the porosity in certain zones, if they are filled with hydrocarbons or are predominantly sandstone with a lower matrix density. Another obstacle to accurate porosity calculations, as well as water saturation calculations, is the clay-bound water that is expected when dealing with high clay percentages in shaly

formations (Asquith and Krygowski, 2004). This skews the real value of porosity and therefore requires a shale volume correction before calculating the effective porosity or subsequently the water saturation. The correction used from David et al. (2015) calculates a shale volume using the gamma ray signature from the log (Eq. 12).

$$GR\ V_{Shale} = \frac{(GR - GR_{Clean})}{(GR_{Shale} - GR_{Clean})} \tag{12}$$

Where,

V_{Shale} = Total shale volume of the formation (%)

GR = The log derived gamma ray signature of the formation (API)

GR_{Clean} = Gamma ray baseline for clean lithology, usually from carbonate or sandstone in the section (API)

GR_{Shale} = Gamma ray maximum for a shale baseline (API)

The shale volume, combined with the neutron-density cross-plot porosity ($PHIA$), can then calculate the effective porosity ($PHIE$) (Eq. 13).

$$PHIE = PHIA \times (1 - V_{Shale}) \tag{13}$$

Once the porosity is corrected for shale volume, the water saturation can be calculated using the new effective porosity ($PHIE$). Using the standard Archie's equation (Eq. 14) described in Asquith and Krygowski (2004), a value for water saturation in the formation can be obtained.

$$S_w = \left(\frac{a \times R_w}{R_t \times \phi^m}\right)^{\frac{1}{n}} \tag{14}$$

Where,

S_w = water saturation of the uninvaded zone (fraction)

a= tortuosity factor (dimensionless; Asquith and Krygowski, 2004)

R_w= resistivity of the formation water at formation temperature (ohm-m)

R_t= true formation resistivity (LLD log, ohm-m)

ϕ= cross-plot porosity, in this case effective porosity after shale volume correction

(fraction).

n= saturation exponent (dimensionless; Asquith and Krygowski, 2004)

m= cementation exponent (dimensionless; Asquith and Krygowski, 2004)

      The tortuosity factor (a) and the cementation exponent (m) are used according to lithology. Shaly sands, like the lithology seen here in the Jo Mill, are given the tortuosity factor of 1.65, as opposed to the carbonate value of 1, and they are given a cementation exponent of 1.33 as opposed to the carbonate value of 2 (Asquith and Krygowski, 2004). The formation resistivity (R_t) is obtained from the log measured deep resistivity (LLD). A formation water resistivity (R_w) of 0.045 ohm-m is used for equation 14, obtained using the Pickett plot method and equation 15 (Asquith and Krygowski, 2004).

$$R_w = \frac{R_o \times \varphi^m}{a} \tag{15}$$

      Where,

R_w= formation water resistivity (ohm-m)

R_o = resistivity of the undisturbed, water bearing zone (LLD), (ohm-m)

a= tortuosity factor (dimensionless; Asquith and Krygowski, 2004)

m= cementation exponent (dimensionless; Asquith and Krygowski, 2004)

      Using the water saturation, effective porosity, and shale volume calculations, a subsequent bulk volume water and clay bound water percentage can be calculated.

Bulk volume water (BVW) represents both the mobile water portion and immobile or

irreducible water bound to the matrix of the rock while clay bound water (CBW)

represents the latter. The BVW calculation is simply the product of the effective porosity

($PHIE$) and the water saturation (S$_w$). The CBW calculation is the product of the BVW

and the shale volume (V$_{shale}$).

The final log derived measurement used is that of total organic carbon (TOC)

from the sonic log and the true formation resistivity log (LLD) (Passey et al., 1990) (Eq.

16).

$$\Delta LogR = \log_{10}\left(\frac{R_t}{R_{tbaseline}}\right) + 0.02{\times}(\Delta t - \Delta t_{baseline}) \tag{16}$$

Where,

$\Delta LogR$= curve separation measured in logarithmic resistivity cycles (Passey et al., 1990)

R_t= deep resistivity measured by the logging tool (LLD) (ohm-m)

$R_{tbaseline}$= resistivity baseline value corresponding to the Δt baseline value (ohm-m)

Δt= measured transit time from the compressional sonic log (μsec/ft.)

$\Delta t_{baseline}$ = corresponding transit time baseline in non-source, clay-rich rocks (μsec/ft.)

(Passey et al., 1990)

This equation then allows the calculation of TOC based on the previous $\Delta LogR$

determination. The level of organic maturity (LOM) included in equation. 17 represents

the organic maturity level in the rock. This variable comes from empirically derived

values associated with the S2 value from pyrolysis analysis and TOC (Passey et al.,

1990). An LOM of 7 in this case represents the onset of maturity for oil-prone kerogen,

and an $LOM$of 12 represents the onset of over maturity for oil-prone kerogen. The LOM

used in this analysis was 9, as it corresponds to the related maturity level seen in

pyrolysis data for the Nobles 3202 samples.

$$TOC = (\Delta LogR) \times 10^{(2.297 - 0.1688 \times LOM)} \tag{17}$$

Where,

TOC= total organic carbon (%)

$\Delta LogR$= curve separation measured in logarithmic resistivity cycles (Passey et al., 1990)

LOM= level of organic maturity

Chapter 5. Results

Mineralogy

XRD analysis at SIRT yields mineral weight percentage results for the Nobles

3202 samples (Fig. 5-1-Fig. 5-3) (Table 5-1). The results show a variation of clay

minerals and micas in the samples, a dominant percentage of quartz, feldspar,

carbonate minerals, and evaporites, as well as some sulfides and oxides. Quartz is

present in every sample, making up more than 53% of the total mineralogy. Albite and

ankerite are also present in every sample, making up a percentage of more than 18%

and 12% of the total mineralogy, respectively (Fig. 5-1). Albite is a feldspar that

represents the sodium end-member of the plagioclase series. Ankerite is an iron (II)

and/or manganese rich carbonate mineral, closely related to dolomite, which is present

in the samples, along with the presence of another manganese-rich end member of

dolomite, kutnohorite. The intergranular cements in the Nobles 3202 samples, from

their mineral percentages, are composed of either quartz or ankerite, which are common in Spraberry sandstone turbidite deposits (Hamlin and Baumgardner, 2013).

Using Schlumberger's ternary lithofacies diagram for mudstones (Fig. 5-3), the XRD results yield specific lithofacies for the Nobles 3202 samples. The slight differences in the amounts of quartz, carbonates, micas, and feldspars, make the samples carbonate-rich siliceous mudstones, silica dominated lithotypes, or mixed siliceous mudstones. In the ternary plot, quartz, feldspar, mafic minerals, and clay minerals, including some micas in this case, define the QFM (quartz, feldspar, and mafic) percentages. When analyzing the clay content in the Nobles 3202 samples, there must be some caution when deciphering the XRD intensity peaks. Structurally illite is quite similar to muscovite, with elemental differences in the amount of silicon, magnesium, iron, aluminum, and potassium. Many times the diffraction peaks that characterize illite and non-illite micas of similar composition and structure, like muscovite, can overlap (Gharrabi et al., 1998). Therefore, clay identified in XRD analysis is compared with the other phyllosilicate minerals observed. Many times in literature and in common definition, clay can be loosely referred to as the presence of clay size grains (<2 μm in diameter) in a sample. When the effects on pore structure are in question, this grain size is of great importance, as its prevalence should correlate with pores of a specific size range.
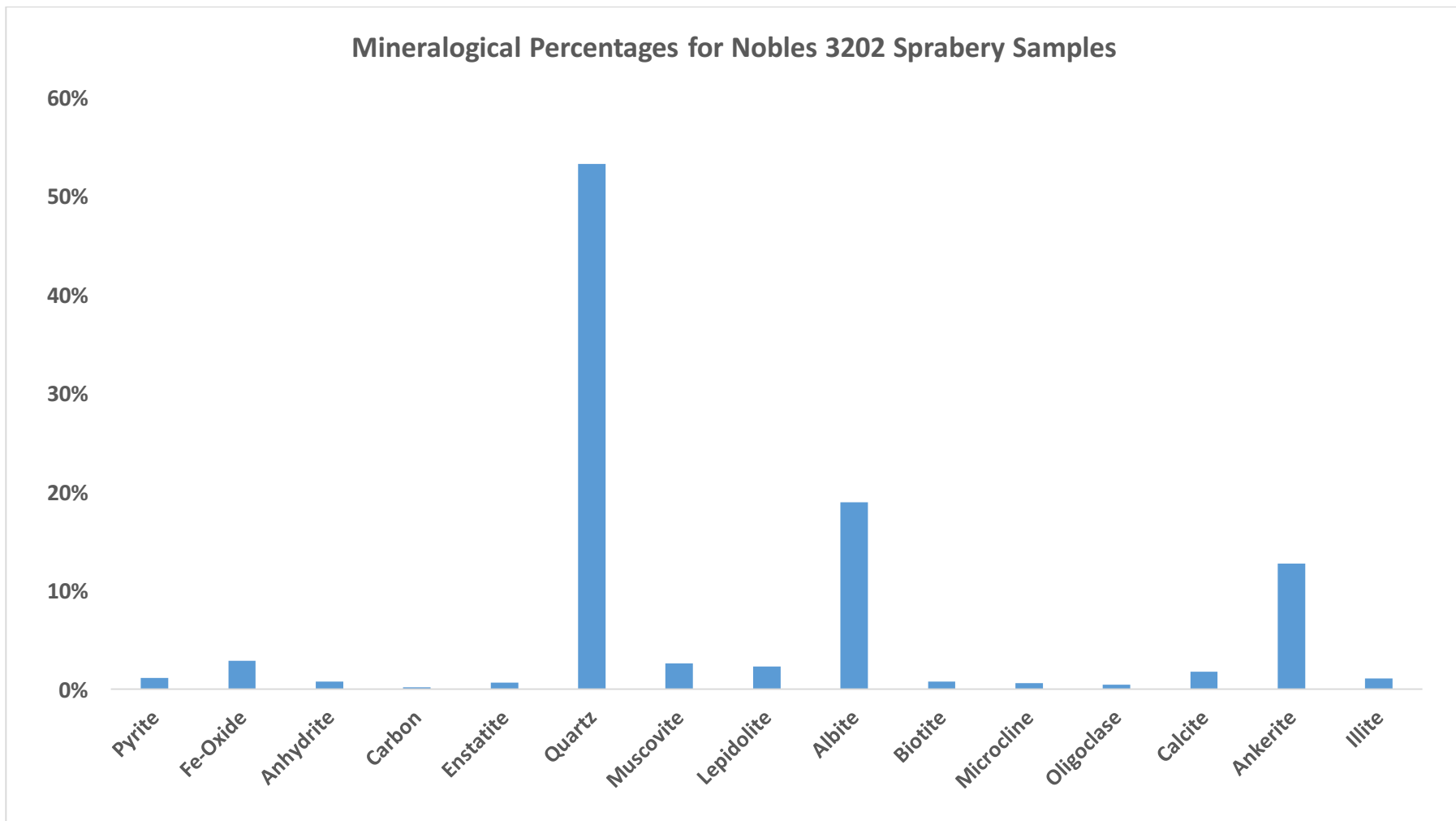
Figure 5-1 Total mineralogy percentage of Nobles 3202 Spraberry samples.

Table 5-1 Mineral weight percentage of individual Spraberry sample from XRD analys

Phase	Type	N8987-S Wt%	N8995-S Wt%	N9009-S Wt%	N9029-S Wt%
Quartz	Silica	44.9	55.8	59	53
Albite	Feldspar	17.3	18.4	21.5	18.7
Anorthite	Feldspar		0.1		
Microcline	Feldspar		2.5		
Oligoclase	Feldspar			1.8	
Enstatite	Pyroxene				2.6
Pyrite	Sulfide	3.1	1.5	2	
Anhydrite	Sulfate			3.3	
Iwakiite (Fe-Oxide)	Oxide	7.5	3.9		
Calcite	Carbonate	0.7	1.6		3.1
Ankerite	Carbonate	9.5	10.6	8.1	11.2
Kutnohorite	Carbonate				11.4
Muscovite	Mica	7.9	2.6		
Biotite	Mica		3.1		
Lepidolite	Mica	9.1			
Illite	Clay			4.3	
		Mixed Siliceous Mudstone	Carbonate-rich siliceous mudstone	Silica-dominated lithotype	Carbonate-rich siliceous mudstone
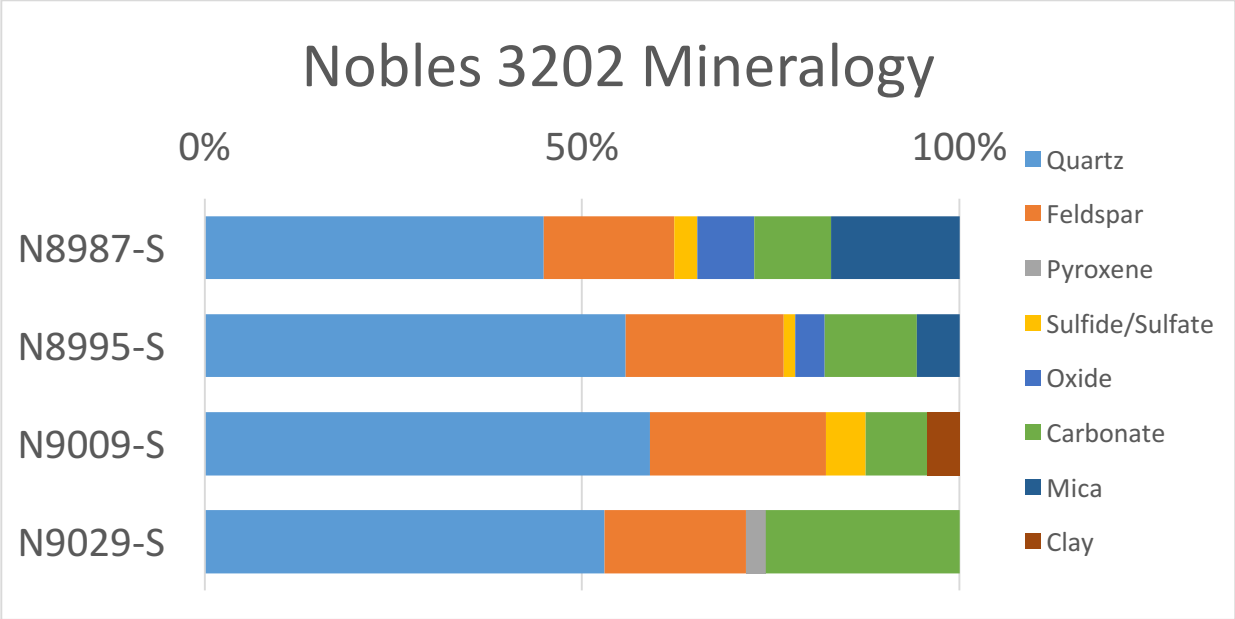
Figure 5-2 Mineral percentage of individual Spraberry samples.
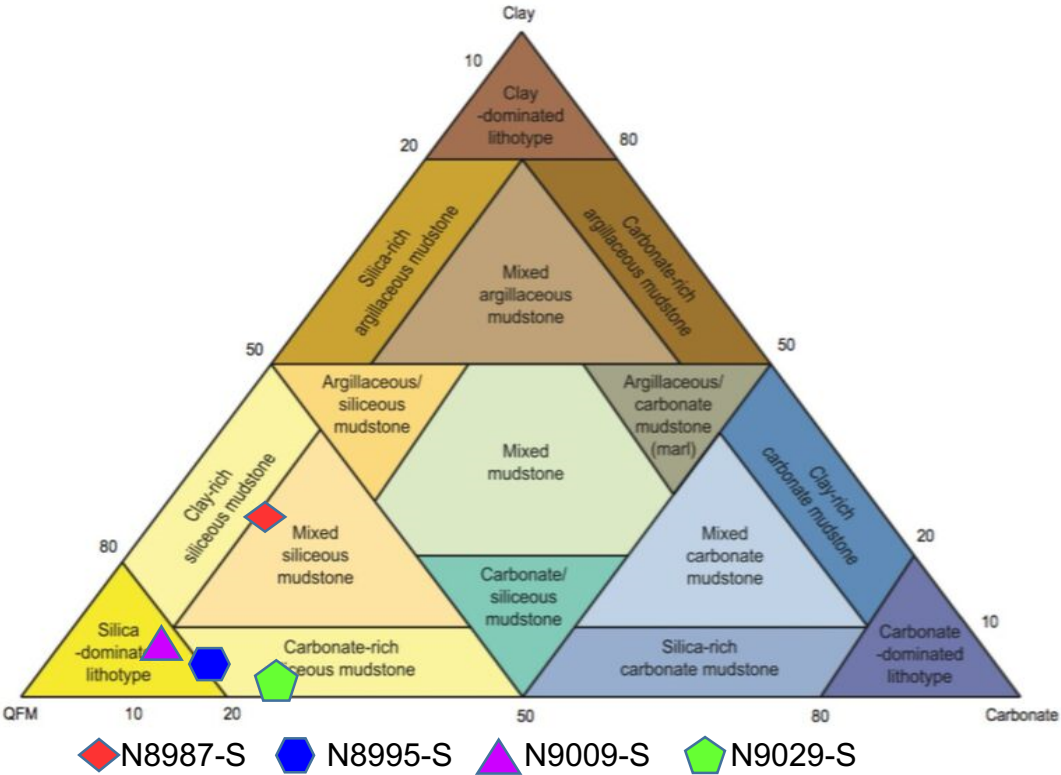
Figure 5-3 Ternary diagram of sCore Lithofacies classification scheme for organic mudstones (from Schlumberger, 2014).

TOC and Pyrolysis

Shown in Table 5-2 are the values from the pyrolysis analysis, obtained at collaborating labs in China, as well as the TOC values from the SIRT. Fig. 5-4 is a modified Van Krevelen diagram that plots the Hydrogen Index against the T_{max} (°C). This diagram shows the kerogen type and the level of organic maturity based on these values.

The different TOC values seen in Table 5-2 are from the collaborating lab in China, well-log analysis using the ΔlogR method, and the SIRT at the University of Texas at Arlington. The TOC values from both labs are similar except for the value for the N9029-S sample, which varies from 0.22% to 2.30%. These discrepancies in values are common, and when using different instruments and standards, TOC can be seen to have a variability of upwards of 8% in weight percentage (King et al., 2015). The machine used solely for the TOC analysis at the SIRT was a wet chemical TOC analyzer whereas the pyrolysis done at the collaborating lab in China was a Rock-Eval method, loss on ignition (LOI) technique. The wet chemistry technique is reported to include positive errors in TOC estimations when the sample includes a certain amount of iron (II) (Fe^{2+}) or chromium (Cr) (Schumacher, 2002). The SIRT analysis also includes inorganic carbon in the results, which is not included in the Rock-Eval method. The N9029-S sample has the largest abundance of carbonate minerals ankerite and kutnohorite, which both are unique in series with dolomite due to iron (II) (Fe^{2+}) and manganese (Mn) commonly replacing magnesium their composition. Kutnohorite is only seen in the N9029-S sample. This could be the source of discrepancy between the TOC values seen from the SIRT and from China. In either case, however, the kerogen

type and maturity characterization is not affected greatly, as the hydrogen index (HI) (Table 5-2) is only changed from 1.33 (mg/g) when using the LOI technique to 13.64 (mg/g) when using the SIRT results. This difference still puts the N9029-S sample well within the immature Type IV inert kerogen type (Fig. 5-4).

Overall, the Nobles 3202 samples showed a wide variety of kerogen type (Fig. 5-4), TOC weight percentage, and S1, S2, and S4 values from sample to sample (Table 5-2). The source rock potential is then quantified by the hydrogen index vs. T_{max} modified Van Krevelen diagram, the productivity index (PI), the vitrinite reflectance (R_o) and the genetic potential (Table 5-2, Fig. 5-4). The samples show to be decreasing in oil proneness with differences in lithology and with increasing depth (Fig. 5-4). Certain ranges that correspond to source rock potential should be taken into account for the T_{max}, TOC percentage, genetic potential, and vitrinite reflectance (R_o) values. The TOC low point for clastic source rocks is 0.5%, the T_{max} for mature source rock starts at 435ºC, the genetic potential value for moderate source rock begins at 2 kg/ton (2000-6000 ppm), and the vitrinite reflectance (R_o) value for mature source rock begins at 0.5 (Tissot and Welte, 1978). According to Scott and Hussain, 1988, Spraberry shales extracted from the Jo Mill field indicated Type II kerogen, immature to early maturation of oils, and a discrepancy between the organic maturity of the Spraberry shales and the oil present within them. The values for N8987-S and N8995-S, which lead to Type II-III kerogen, are in agreement with the findings of Scott and Hussain (1988). While the averages show a relatively mature and moderate source rock potential, the distinction between the N8987-S and N8995-S sample values and the others must be taken into account.

Table 5-2: TOC & Pyrolysis results from various methods.

Sample	TOC			Pyrolysis							
	SIRT TOC (wt. %)	ΔLogR TOC (wt. %)	TOC CUG (wt. %)	S1 (mg/g)	S2 (mg/g)	S4 (mg/g)	R_o (%)	PI (S1/S1+S2)	HI (S2/TOC)	Genetic Potential (S1+S2)	TMAX (°C)
N8987-S	3.23	4.34	4.43	2.04	10.57	33.85	0.71	0.16	238.60	12.61	437
N8995-S	0.81	3.08	0.98	0.53	1.41	8.15	0.78	0.27	143.88	1.94	441
N9009-S	0.34	0.75	0.27	0.21	0.27	2.31	0.72	0.44	100.00	0.48	438
N9029-S	2.30	1.58	0.22	0.04	0.03	2.10	0.69	0.57	13.64	0.07	436
Average	1.98	2.44	1.48	0.71	3.07	11.60	0.72	0.36	124.03	3.78	438
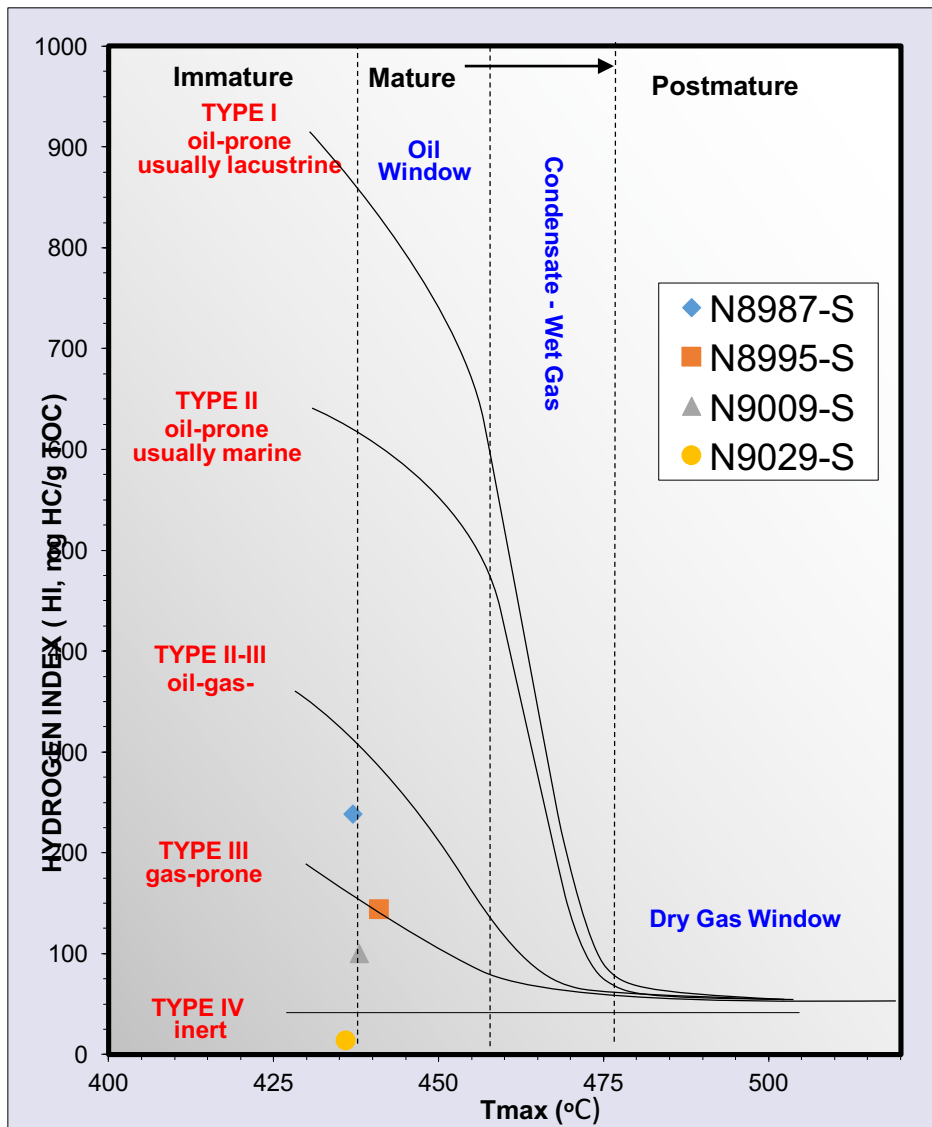
Figure 5-4 Kerogen type and maturity plot for Nobles 3202 samples.

Wettability

The individual contact angle measurements vs. time for DI water, API brine, 20% Isopropyl alcohol (IPA), and n-decane are shown below (Fig. 5-5; Table 5-3) for the Nobles 3202 samples. This method used smoothed surfaces and pure fluids, as ignoring these factors can greatly diminish the integrity of the results (Thyne, 2013). All of the samples show a very low contact angle for n-decane, and a low angle for the 20% IPA, excluding the N9009-S sample (Fig. 5-5). The N9009-S and N9029-S samples show the lowest contact angles for all of the fluids. The mineralogy exhibits an effect in the N9009-S sample, as it has the lowest contact angle to DI Water. This is expected for its comparatively high percentages of quartz, as it is known that quartz tends to be generally water-wet (Habibi et al., 2016).

Overall, the results yield low contact angles for all the fluids used, especially for n-decane and IPA, which suggests relatively heterogeneous wetting characteristics of the samples with slight hydrophobic tendencies. This heterogeneity of wetting characteristics is expected within the complex lithology, hydrocarbon coatings, and organic particles that are often observed in the Spraberry (Buckley et al., 1996).

Table 5-3: Contact angles at 30 seconds for Nobles 3202 samples; at 30 seconds n-decane contact angle fell below the decision limit of the instrument.

Contact Angle (degrees)				
Sample ID	DI Water	API Brine	20% IPA	n-Decane
N8987-S	48.90	55.54	27.12	0.41
N8995-S	26.44	16.89	17.39	1.16
N9009-S	8.61	14.40	21.08	4.02
N9029-S	16.20	23.33	12.03	0.00
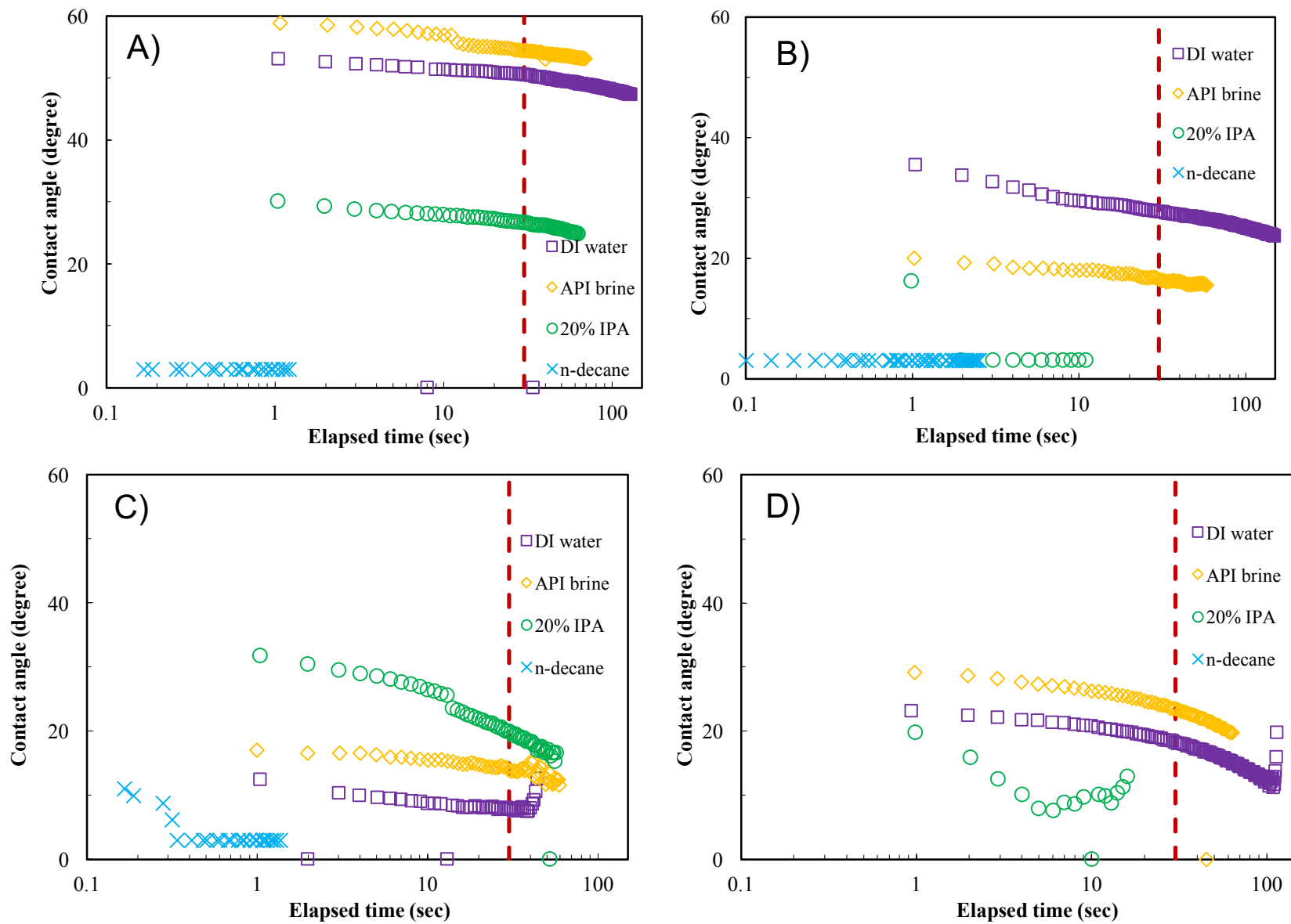
Figure 5-5 Contact angle measurement vs. time. A) N8987-S, B) N8995-S, C) N9009-S, D) N9029-S

Helium Porosity and Permeability

The resulting values from the AP-608 helium porosity and permeability analysis are shown in Table 5-4. This analysis used the plug sample size, and. Due to the larger sample size, factors such as small and large-scale fractures, as well as bedding planes contribute to the overall measured porosity and permeability. The influence of these factors are evident in the results, as the MICP and well-log measured porosity and permeability are smaller than observed in the helium method. Pl

Table 5-4: Helium Porosity and Permeability values.

Sample ID	Testing Direction	Porosity (%)	Permeability (µD)
N8995-S	Transverse	3.314	0.6
N9009-S	Transverse	6.125	1.0

Low-Pressure Nitrogen Physisorption

Low-pressure nitrogen physisorption yields the pore size distribution, physisorption isotherms, and hysteresis loop charts presented as Fig. 5-6 to Fig. 5-8. This comprehensive analysis through the adsorption and desorption behavior of the nitrogen gas molecule onto the surface of the Nobles 3202 samples. Pore size classification for materials containing nanometer-sized pores includes macropores (>50 nm), mesopores (2-50 nm), and micropores (<2 nm) (Zdravkov et al., 2007). The N_2 method measures the larger macropores and mesopores, as well as the micropore occurrences in the rock (Clarkson et al., 2013). The isotherms and resulting hysteresis loops, as seen in Fig. 5-8, help identify and predict certain pore network characteristics such as specific pore shapes and pore size tendencies (Sing et al., 1985). The type of

isotherm shape is dependent upon the extent and the restriction of the adsorbent throughout the medium, and the hysteresis loop usually results from the capillary condensation in mesopore structures (Sing et al., 1985).

The Nobles 3202 samples show pore sizes from as low as 1.45 nm to as large as 21 nm (Fig. 5-6). These sizes encompass the micropore and mesopore size range, but do not enter the macropore size range. The range of pore size distribution varies within the nitrogen method in regards to the BJH and DFT methods of quantifying the isotherms. The widest range of pore sizes, using the DFT method, occurs in the N8995-S sample, with pores from 1.45 nm to 21 nm. However, the N9029-S sample shows the most even distribution of porosity for different pore widths.

The physisorption isotherms can be classified as Type I through Type VI (Fig. 5-7) and the results in Fig. 5-8 show that the samples exhibit traits of Type II and Type III isotherms. The Type II isotherm is the most common form of adsorption, and represents the unrestricted adsorption in monolayer-multilayer systems. The point B (Fig. 5-7) is indicative of the stage at which a monolayer coverage is complete and multilayer coverage is about to begin (Sing et al., 1985). The only difference between the Type II and Type III is the non-existence of a Point B. All systems conform more strongly to the Type II isotherm as there is, at best, a faint existence of a point B, and the curves are not convex at low relative pressures. The hysteresis loops (Figs. 5-7 and 5-8), are an evidence of different types of capillary condensation in mesopores structures. The samples tend to exhibit the H3 hysteresis loop. The H3 hysteresis loops is indicative of slit-shaped pores associated with aggregates of plate-like particles (Sing et al., 1985). The H3 hysteresis loop also shows the limit of investigation for the N_2 technique, as the

isotherm shows no limit of adsorption at higher relative pressures. One factor that must

be taken into account when using the N_2 physisorption method is that it can be limited to

investigating pores of size 0.3 nm to 200 nm (Kuila and Prasad, 2012). The upper limit

is later quantified in the MICP results, and further proves the need for different types of

analyses.
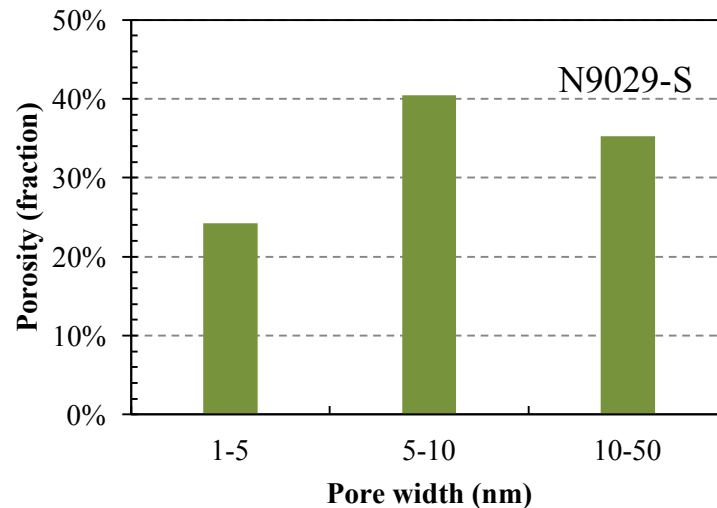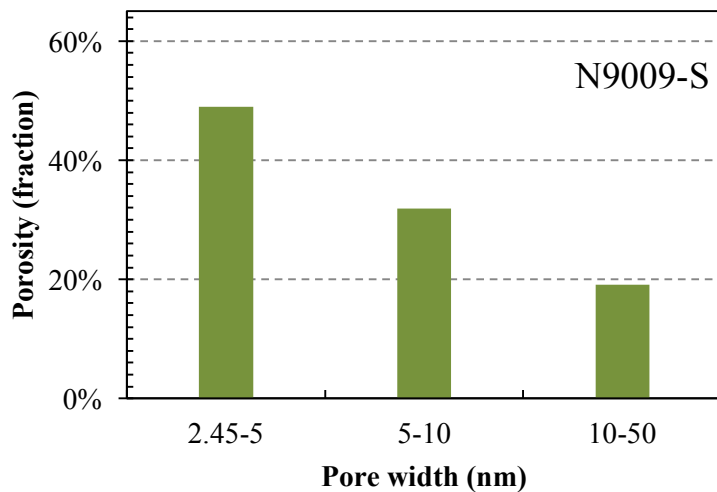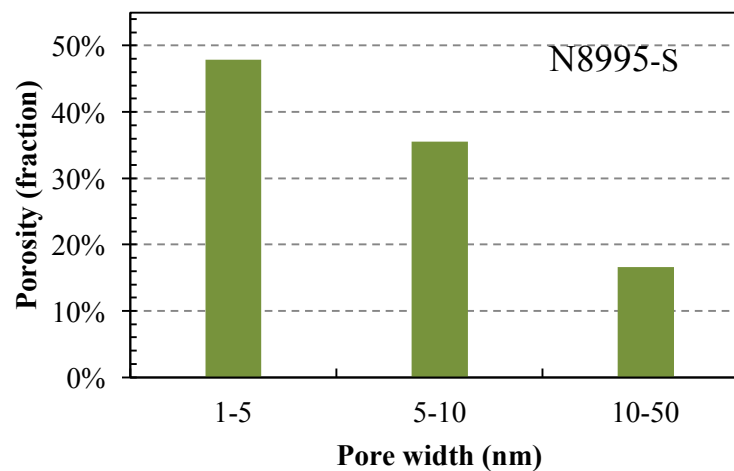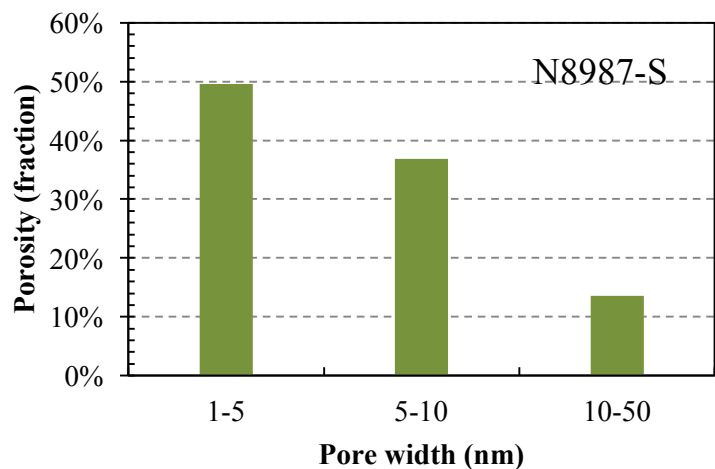
Figure 5-6 Pore size distribution from N_2 physisorption analysis.
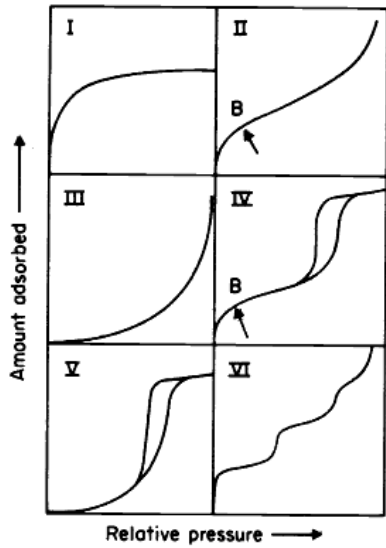
Fig. 2.   Types of physisorption isotherms
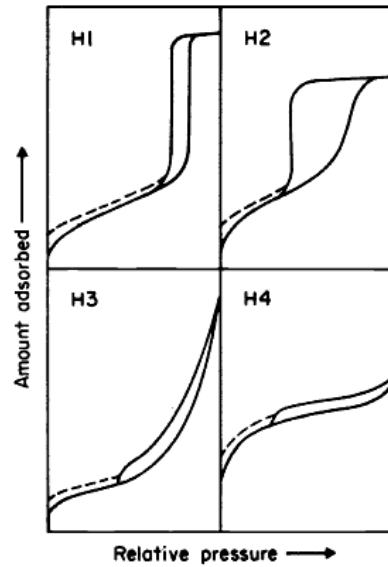
Fig. 3.   Types of hysteresis loops

Figure 5-7 Classification of physisorption isotherms and hysteresis loops (from Sing et al., 1985).
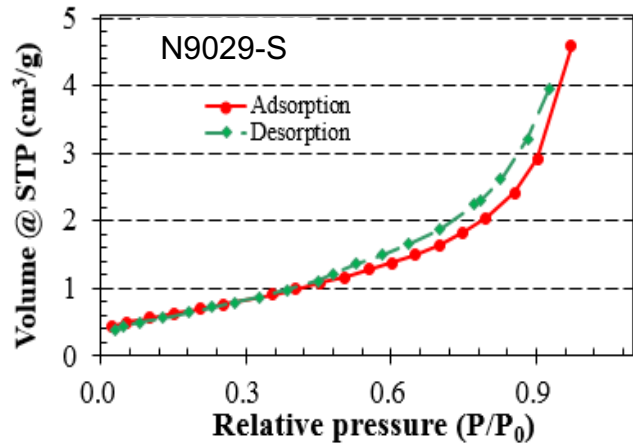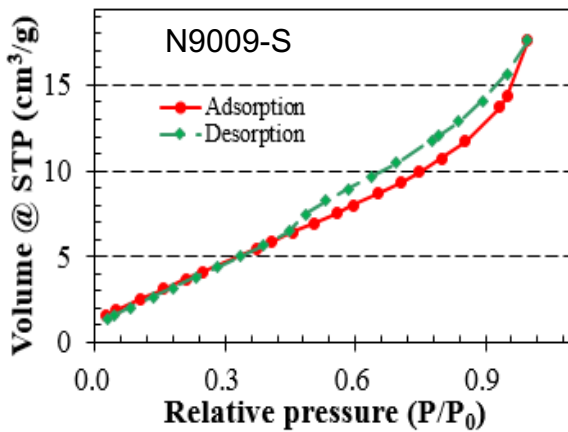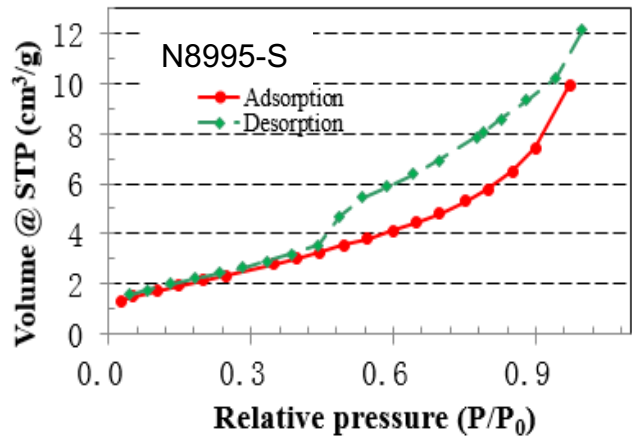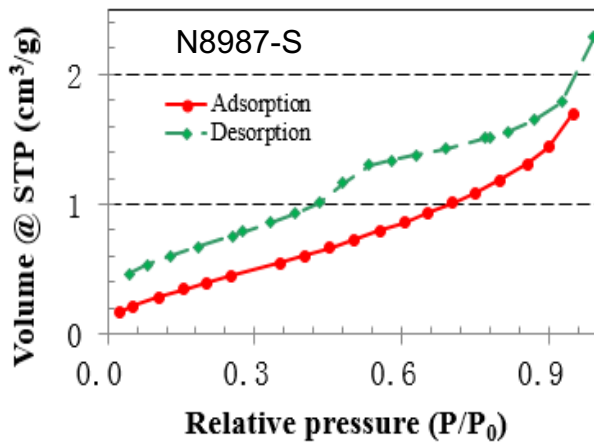
Figure 5-8 Adsorption and desorption isotherms for the Nobles 3202 samples.

Mercury Injection Capillary Pressure (MICP)

Mercury intrusion porosimetry gives, perhaps, the most comprehensive set of results in regards to the overall pore characteristics of the samples. The results yielded from this experiment (Table 5-5) include the bulk density, porosity, total pore volume, total pore area, average pore diameter, pore diameter medians in volume and area, permeability, and tortuosity. The permeability and tortuosity were quantified from the directly measured features such as the pore volume, porosity, density, and pore size distribution of the Nobles 3202 samples. The patterns of mercury intrusion, when related to pressure fluctuation, illuminate the distribution and behavior of the pores and pore throats in the samples.
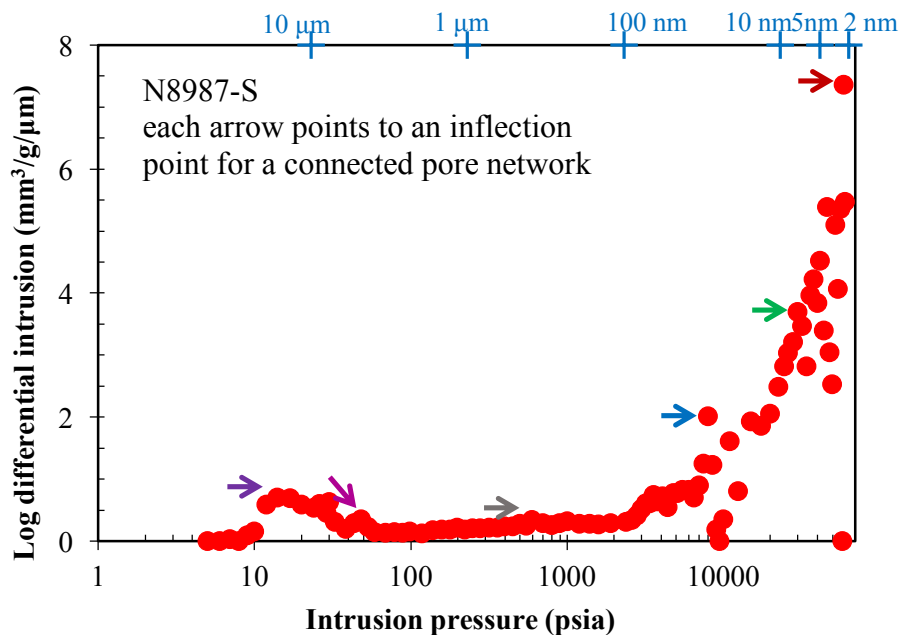
Figure 5-9 MICP intrusion profile for N8987-S; arrows indicate multiple connected pore networks across μm-nm pore-throat spectrum, with each networking having its porosity and permeability.
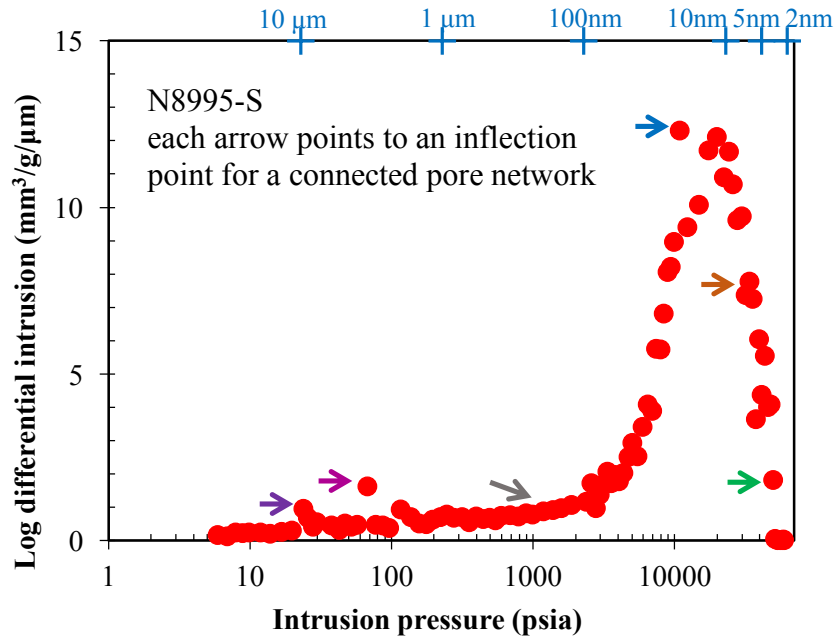
Figure 5-10 MICP intrusion profile for N8995-S.
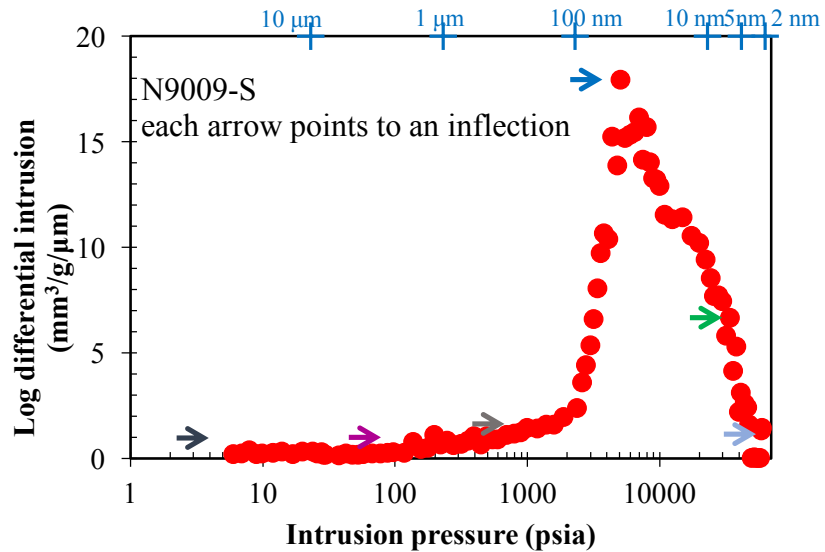
Figure 5-11 MICP intrusion profile for N9009-S.

The intrusion profiles in Fig. 5-9-Fig. 5-11 show the relationship between the intrusion pressure increase and the resulting intrusion of mercury into the samples. The peaks or inflection points, defined as the highest point in the log differential intrusion, are indicative of the threshold pressure for the specific pore size system in which they are found (Gao and Hu, 2013). The largest inflection point seen in each of the profiles

tends to occur in larger pore size ranges with an increasing depth (Fig. 5-9 to Fig. 5-11). The changes in total pore volume, pore diameter, overall porosity, and permeability increases with increasing depth, whereas the tortuosity does not show the same correlation (Table 5-5).

The relation of intrusion and extrusion curves (Fig. 5-13) yield hysteresis curves similar to those in the N_2 physisorption analysis. When a smaller amount of mercury is extruded from the samples, this suggests a network of pore spaces connected by narrow pore throats (Yang et al., 2017). As mercury is intruded into the sample pores at higher and higher pressures, the pore bodies and throats are filled. When the mercury is extruded, the pressure is not high enough for the total extrusion of mercury, resulting in the trapping of mercury and subsequent hysteresis curves (Stegemeier, 1977) (Fig. 5-13).

As stated earlier, the classification for pore sizes can vary when investigating different lithology. A well-developed classification for pore sizes in shale systems is one that includes macropores (>50 nm), mesopores (2-50 nm), and micropores (<2 nm) (Zdravkov et al., 2007). Only mesopores and macropores can be seen in the MIP analysis, as the lower limit reaches 2.8nm (Fig. 5-14). Many different mineralogical and structural variances can be responsible for the different pore sizes in the Spraberry samples. Most commonly, three categories emerge when defining the pore types, such as interparticle, intraparticle, and organic matter pores (Loucks et al., 2012). In general and in previously observed research, pore networks in specific size ranges observed in MICP tend to correspond to the following mineralogical and structural characteristics (Hu, 2016; Hu et al., 2017):

Micro-fractures: ~ >1 μm

Interparticle pores: ~ 0.05 -1 μm

Intraparticle pores: ~ 101- 50 nm

Organic matter-hosted pores: ~5-10nm

Inter-clay platelet pores: ~ <5 nm

The more voluminous intrusion of the smaller scale mesopores (2.8-10nm) in N8987-S shows that the pore network can largely be attributed to pores associated with the conversion of organic matter into hydrocarbons, and spaces within the clay mineral framework p (Fig. 5-13). N8987-S also shows the greatest cumulative intrusion into 10-50μm sized pore throats, suggesting the possible presence of micro-fractures within the sample as well as well-developed pore networks along bedding planes (Fig. 5-9). The N8995-S and N9009-S samples exhibit the 70% of pores with a diameter of 5-50 nm, which suggests the prevalence of intragranular mineral framework hosted pores from ~ 0.01-0.05μm, as well as some organic matter-hosted pores from 0.005μm-0.01μm.

In particular, the large cluster of inflection points near the 10μm mark in the N8987-S sample (Fig. 5-9) points to the intrusion of mercury into these micro-fractures, or along bedding planes. This pore throat size range exceeds the upper limit of the N_2 sorption technique (>200 nm) (Kuila and Prasad, 2012), and again reaffirms the need for multiple methods of investigation. In general, Fig. 5-14 shows that the pore throat range 0.0028-0.01μm, in terms of cumulative intrusion, is most abundant in the N8987-S sample and the size range 0.01-1.0μm is most abundant in the N8995-S and N9009-S samples.

The MICP method also generated a distribution of particle sizes for each sample based on the Mayer-Stowe (1965) theory relating particle size to the breakthrough pressure of mercury. Using the U.S. Department of Agriculture Soil Texture Classification system, the sand-silt distinction is made at the 0.05 mm particle size. From Fig. 5-12, it is seen that the majority of the particle size distribution lies in the clay to silt size range. Another factor that can be taken into account is the packing structure of the grains. Hu (2016) showed that a rhombohedral packing structure can reduce pore size diameter by 37% when compared to a cubic packing structure. This difference could drastically affect the porosity in the Nobles 3202 samples. Using Fig. 5-12, the particle size distribution can be evaluated against the MICP results for porosity, permeability, and pore size distribution.
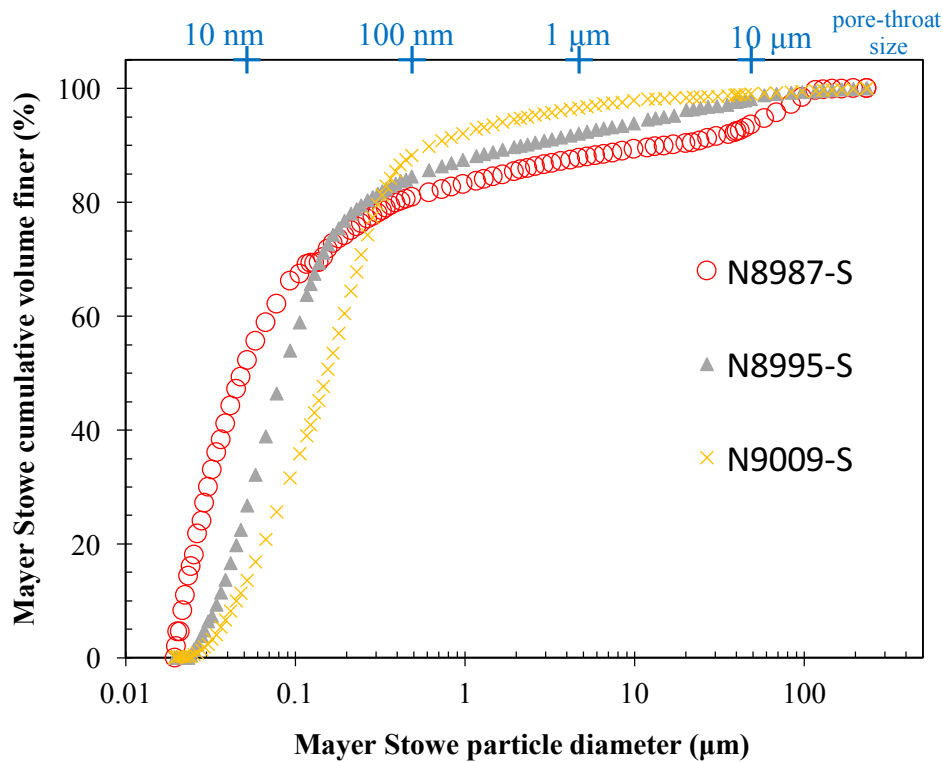
Figure 5-12 MICP derived Mayer-Stowe particle size distribution for the Nobles 3202 samples.
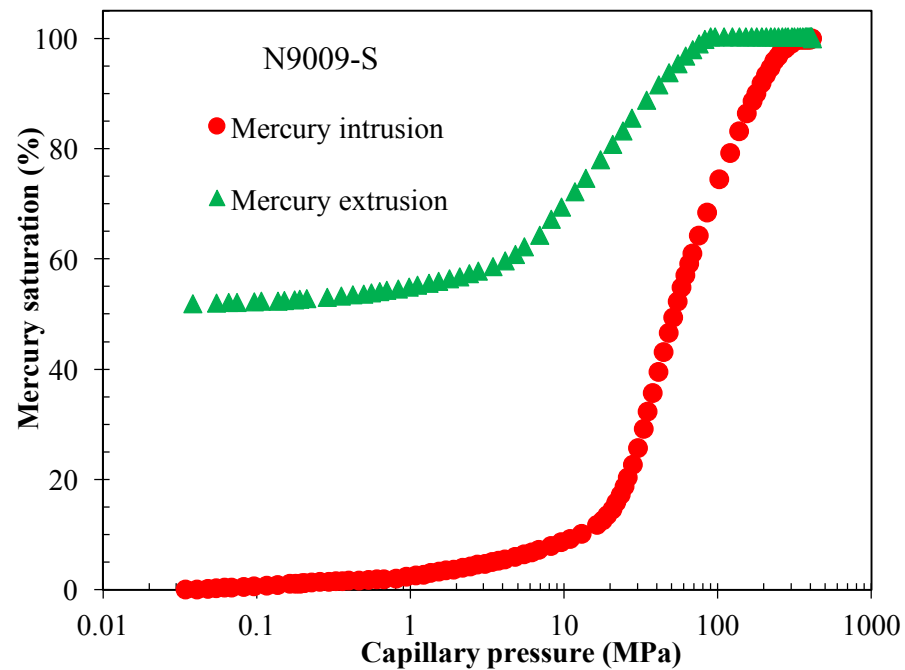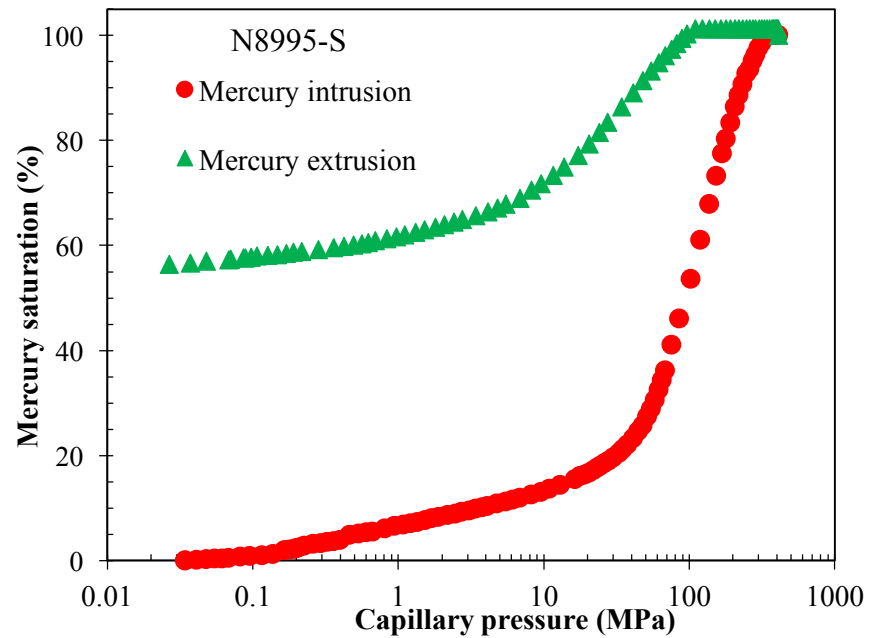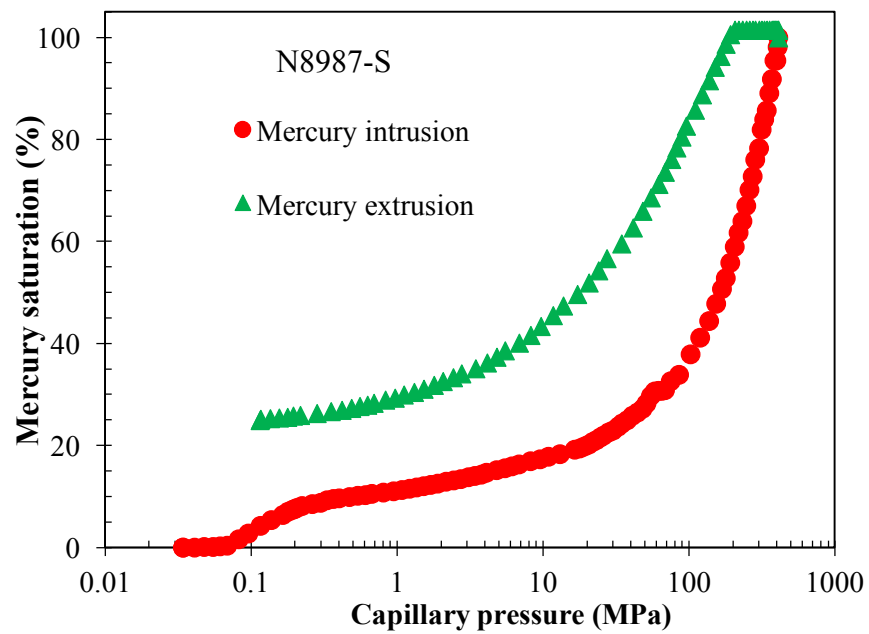
Figure 5-13 MICP intrusion and extrusion hysteresis for Nobles 3202 samples.

Table 5-5: MICP results.

Sample ID	N8987-S	N8995-S	N9009-S
Bulk density (g/cm^3)	2.55	2.56	2.52
Apparent (skeletal) density (g/cm^3)	2.57	2.63	2.63
Porosity (%)	0.99	2.78	3.89
Total Pore Area (m^2/g)	2.15	3.79	3.79
Total Pore Volume (cm^3/g)	0.00	0.01	0.02
Mercury Entrapment (%)	24.87	56.70	51.91
Median Pore Diameter (Volume)(nm)	7.50	13.10	23.80
Median Pore Diameter (Area)(nm)	4.40	7.60	10.00
Average Pore Diameter (nm)	7.30	11.50	16.30
Pore-throat diameter % (0.0028-0.005 μm)	24.07	3.76	1.37
Pore-throat diameter % (0.005-0.01 μm)	28.16	23.01	12.18
Pore-throat diameter % (0.01-0.05 μm)	24.08	52.74	57.28
Pore-throat diameter % (0.05-0.1 μm)	4.60	5.02	17.41
Pore-throat diameter % (0.1-1 μm)	6.83	7.48	8.27
Pore-throat diameter % (1-10 μm)	5.88	6.11	2.47
Pore-throat diameter % (10-50 μm)	6.38	1.88	1.02
Permeability (Harmonic mean, nD)	1.87	13.01	40.47
Permeability (Geometric mean μD) (1st 3 infl. points)	49.38	60.53	26.71
Tortuosity (Harmonic mean τ)	3.55	5.84	3.28
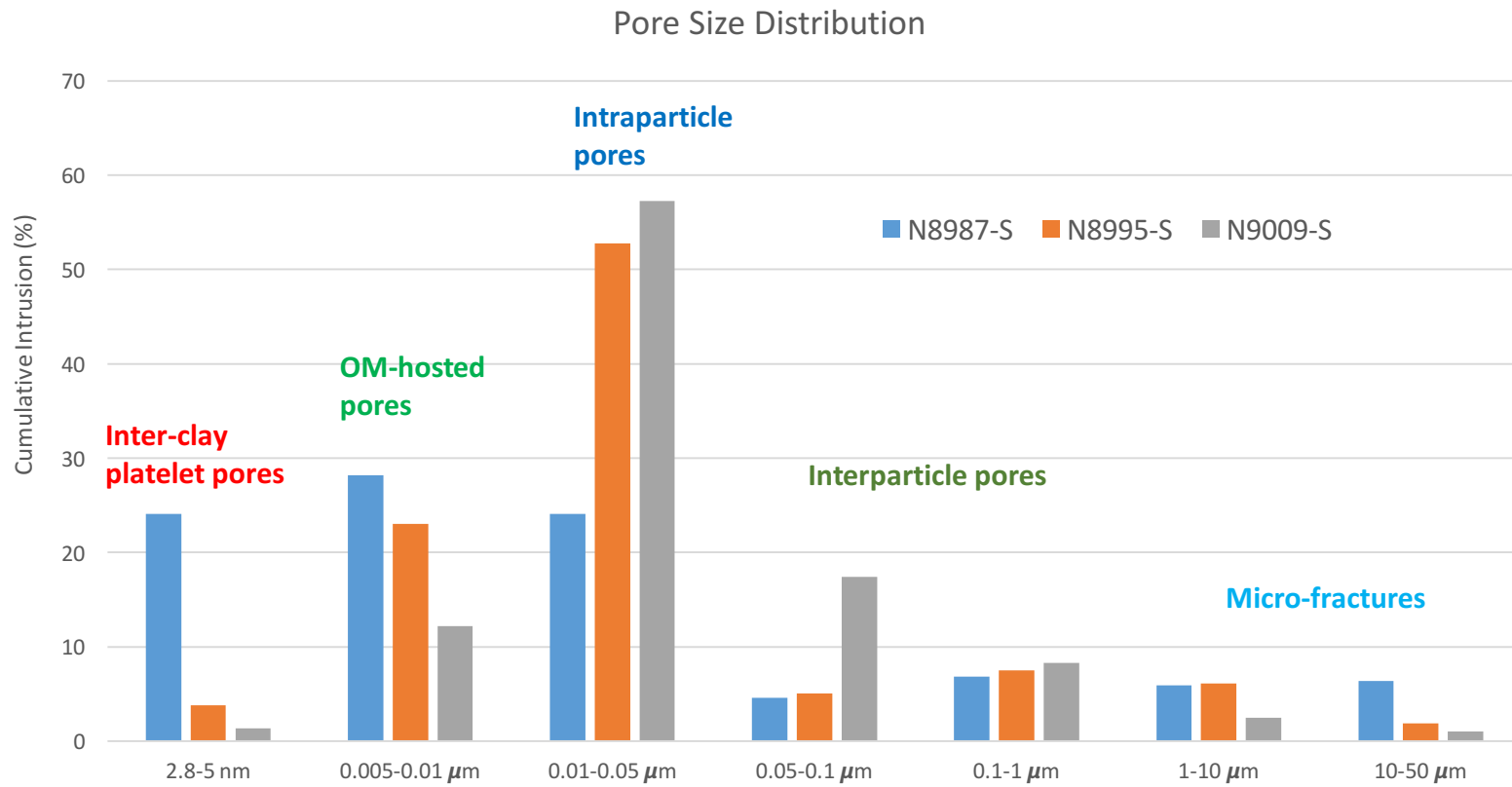
Figure 5-14 Pore throat diameter distribution vs. cumulative intrusion for the Nobles 3202 samples.

Spontaneous Fluid Imbibition

Imbibition is a dominant mechanism for spontaneous fluid movement in the subsurface, and this process has been investigated for the Nobles 3202 samples. Observed and quantified in the imbibition experiment is the cumulative imbibition as related to time, which yields the relationship between the pore network and the fluid under investigation. Using n-decane and DI water as proxies for hydrophobic and hydrophilic fluids, the different slopes of imbibition vs. time are observed (Table 5-6) (Figs. 5-15 to 5-18). With low permeability and porosity being regular properties of the Spraberry lithology, understanding the pore-fluid relationship is crucial to predicting the production behavior of these reservoirs.

The stages and slopes represent specific time periods during the imbibition process. These stages can be described as the initial imbibition stage (Stage I), the linear imbibition stage (Stage II), and the late imbibition stage (Stage III) (Yang et al., 2017). Individual slopes, in this case, Slope I, Slope II, Slope III, and Slope IV represent these stages. Slope I represents the initial imbibition seen in the early stage of the experiment, which is affected by boundary conditions and can lead to unstable fluctuations in the sample's weight gain. Slope I is also identified by a curved imbibition front, due to the adherence of the external liquid menisci of the fluid (Kiepsch and Pelster, 2016). The steep behavior of Slope I is due to the rapid intrusion of fluid into edge accessible porosity of the sample (Figs. 5-15 to 5-18). According to percolation theory discussed by Ewing and Horton (2002), the connectivity of the accessible pores acts in accordance to the proportional relationship between the root-mean-square of the distance (L) from the starting point and the square root of time ($T^{0.5}$). This relationship

characterizes the behavior of fluid flow in well-connected pore spaces. For well-connected pore spaces, the wetting front advances with the square root of time, and for poorly connected pore spaces the front advances approximately one-fourth the power of time (Hu et al., 2012).   Slope I then transitions to Slopes II and III, which quantify the majority of the linear imbibition behavior in Stage II. The imbibition slopes seen in Table 5-6 are representative of the Stage II connectivity slopes. Slopes II and III represent the majority of pore connectivity throughout the rock. Finally, Slope IV represents a very slow uptake of the fluid due to either the low permeability and poor connectivity of the shale matrix in regards to the particular fluid, or due to the fluid reaching the top of the sample in Stage III (Yang et al., 2017). These causes must be understood based on the wetting characteristics of the rock as well as other characteristics found in previous analysis. The predicted permeability values (Table 5-6) (nD) show little variations between the high connectivity slopes of the n-decane experiments.

Overall, the n-decane experiments yield higher connectivity slopes, anywhere from 0.3 to 0.8 (Table 5-6), which suggests a well-connected hydrophobic pore network. The DI water results yielded lower connectivity slopes, only up to 0.4, which suggest a low to intermediate connectivity of hydrophilic pore networks. While the Slope IV was evident in 3 out of the four samples for n-decane, when the permeability (nD) and porosity values (≤5%) of minute scale are taken into account, these slopes can be attributed to the low pore connectivity of the shale matrix (Yang et al., 2017), and not to the fluid reaching the top of the sample. Microstructural front broadening and impartial filling heights of the rock (Kiepsch and Pelster, 2016) can also explain Stage III or Phase III.

Table 5-6: Nobles 3202 individual slope values for fluid imbibition analysis.

Sample	Fluid	Sample Dimensions (cm)	Connectivity Slope	n-decane Predicted k (µD)
N8987-S	DI water	1.039 L x 0.957 W x 1.080 H	0.265	-
	n-decane	1.172 L x 1.12 W x 0.910 H	0.819	2.29
N8995-S	DI water	0.941 L x 1.056 W x 1.075 H	0.169; 0.330	-
	n-decane	1.075 L x 1.160 W x 0.881 H	0.295	-
N9009-S	DI water	1.200 L x 1.168 W x 0.900 H	0.356; 0.204	-
	n-decane	1.117 L x 1.057 W x 0.906 H	0.736	2.47
N9029-S	DI water	1.102 L x 0.962 W x 1.195 H	0.448; 0.264	-
	n-decane	1.111 L x 1.161 W x 0.883 H	0.692	2.47
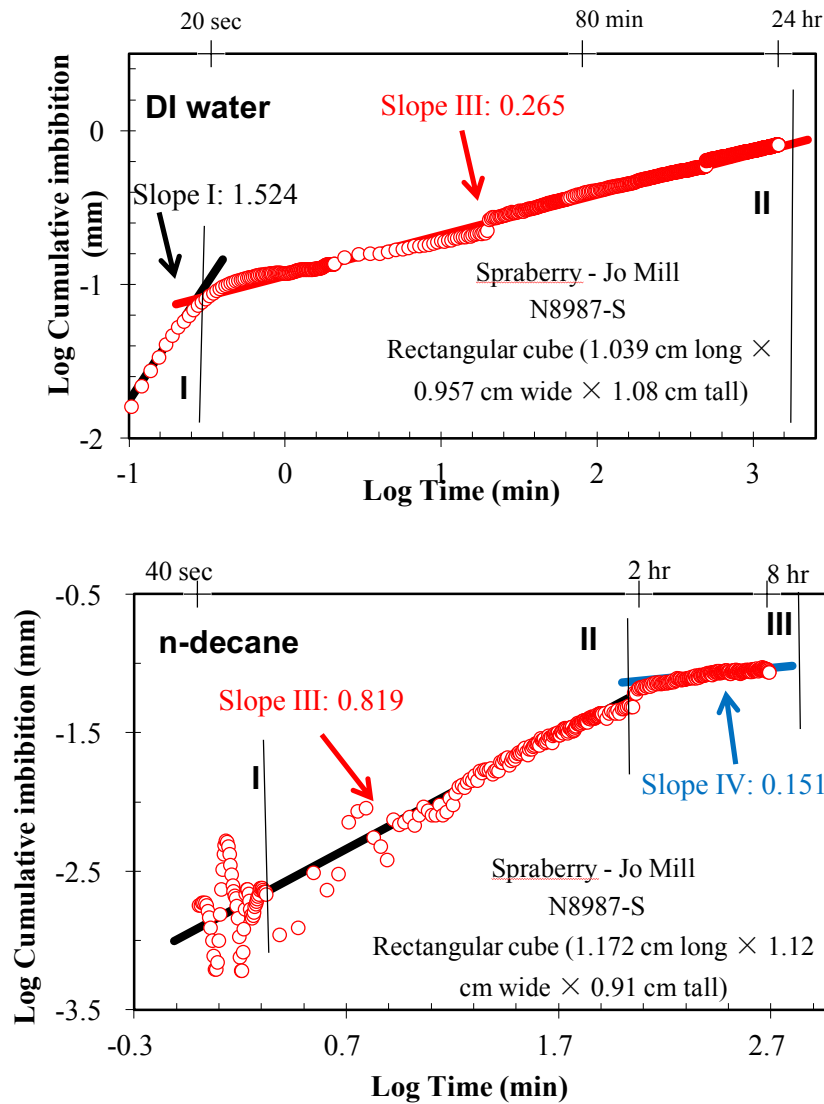
Figure 5-15 N8987-S spontaneous fluid imbibition vs. log time for DI water and n-decane.
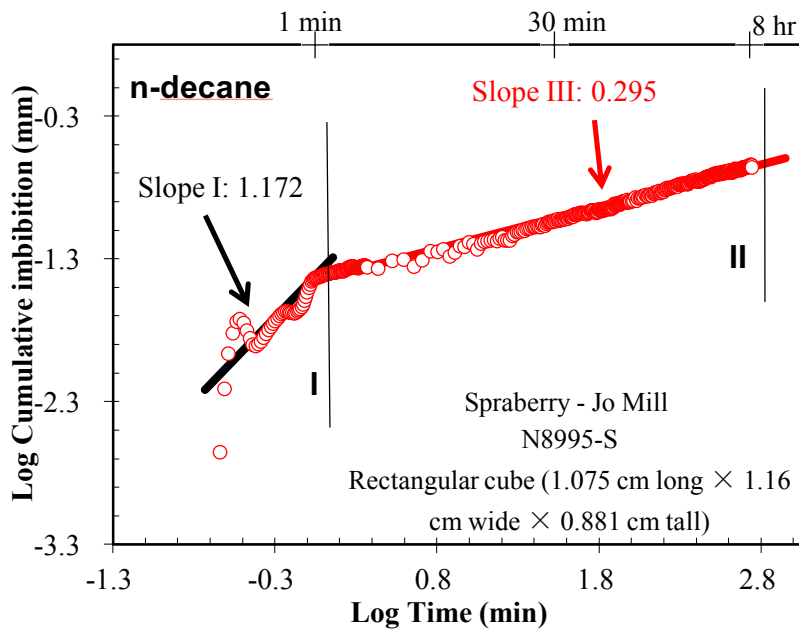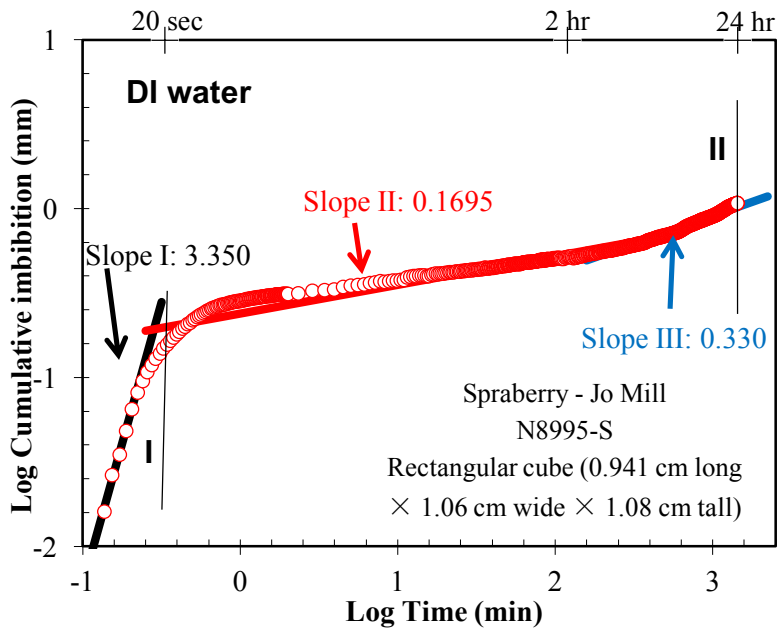
Figure 5-16 N8995-S Spontaneous fluid imbibition vs. log time for DI Water and n-decane.
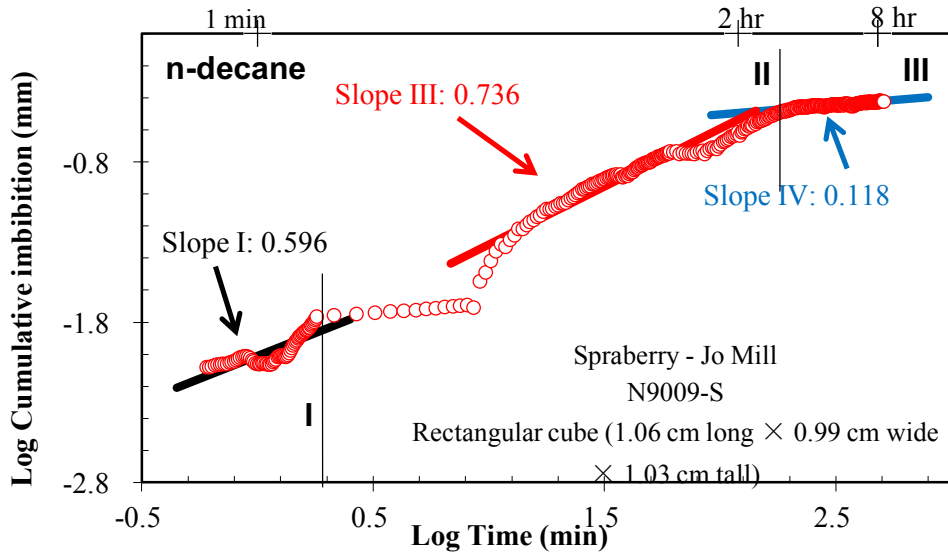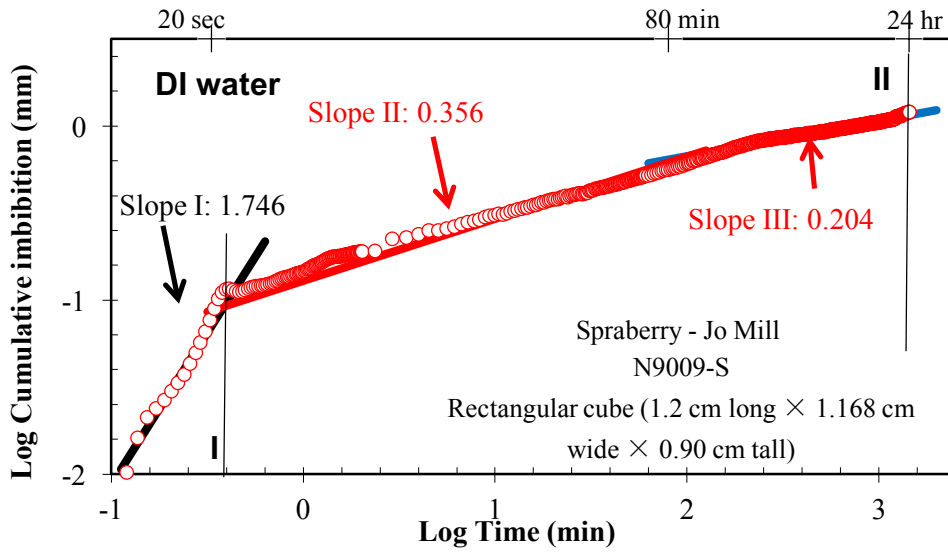
Figure 5-17 N9009-S Spontaneous fluid imbibition vs. log time for DI Water and n-decane.
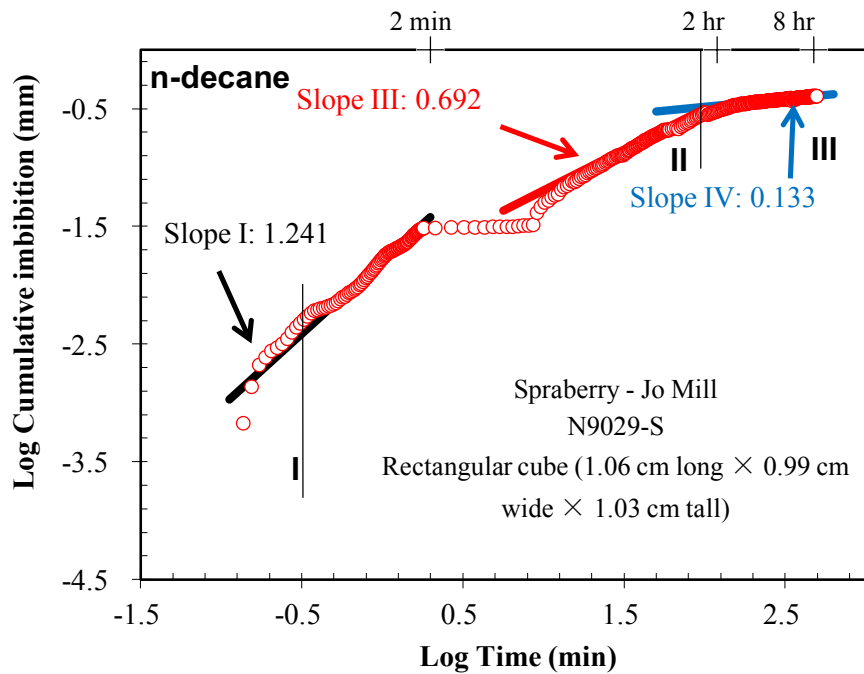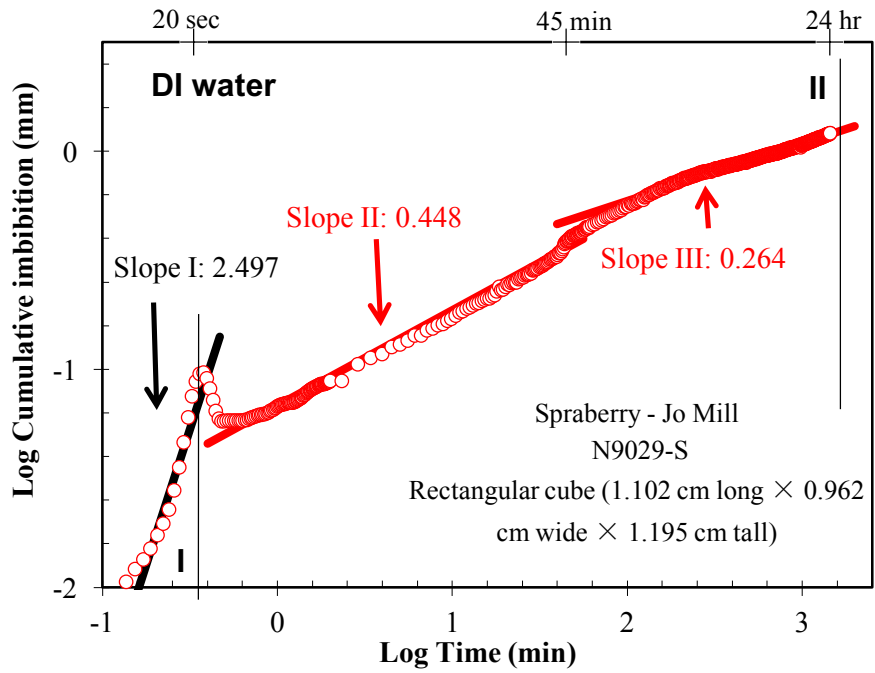
Figure 5-18 N9029-S Spontaneous fluid imbibition vs. log time for DI Water and n-decane.

Chapter 6. Discussion

TOC and Pyrolysis

The Jo Mill zone of the Nobles 3202 well exhibits various hydrocarbon properties from organic maturity, TOC, to overall potential for hydrocarbon generation. These values also show variances between the three different methods used to obtain the TOC weight percentage. While the average values such as T_{max}, TOC, vitrinite reflectance, and genetic potential (Table 5-2) show the source rock potential of the Nobles 3202 samples, there are then ways to quantify the current producible oil potential for the samples.

The three different methods used to obtain TOC were the Rock-Eval loss on ignition (LOI) technique, the ΔlogR log curve (Fig. 6-1), and the wet chemistry technique done at the SIRT (Table 6-1). The variances in TOC are evidence of the strengths and weaknesses of each method. The ΔlogR method requires a LOM value that is determined by the combination of vitrinite reflectance, thermal alteration index, Tmax, and burial and thermal alteration history. If the values listed previously are not in agreement with each other, the absolute TOC values from the log curve will be somewhat in error (Passey et al., 1990). The wet chemistry method used at the SIRT also is susceptible to variances in iron (II) (Fe^{2+}) or chromium (Cr), which can represent a direct relationship with positive errors in TOC estimations (Schumacher, 2002).

Shales within the Spraberry have previously shown to be excellent potential source rocks, with average TOC values of 2.5% and genetic potential averages of 14.31 kg/ton (Scott and Hussain, 1988) (Table 6-1). The one shale sample within the Nobles 3202 samples, N8987-S, exhibited similar values such as a TOC wt. percentage of

74

4.43% (CUG) and a genetic potential of 12.61 kg/ton, which is exemplary of a good

source rock (Tissot and Welte, 1978). This potential of the N8987-S sample, however,

is different from the other Nobles 3202 samples. The N8995-S, N9009-S, and N9029-S

samples all display TOC wt. percentage below 1% (LOI values), and genetic potential

values below 2 kg/ton, which is evidence of no oil, with some potential for gas (Tissot

and Welte, 1978). Additionally, criteria for oil prone kerogen used in Magoon et al.,

(1999) study of Alaska's North Slope used a minimum of 1.0 wt. percentage TOC, an

S2 value of at least 6 mg HC/g rock, and HI value of 400 mg HC/(g TOC). While the

N8987-S sample displays characteristics of a good source rock, the kerogen content of

the remainder of the samples in the Jo Mill zone show little to no evidence for potential

oil generation in regards to their TOC, S2, R_o, and HI values (Table 5-2).

Table 6-1: Comparison of TOC values from the CUG, Shimadzu Institute for Research
Technologies (SIRT), and well-log analysis.

Sample ID	CUG TOC (wt. %)	SIRT TOC (wt. %)	ΔLogR TOC (wt. %)	Kerogen Type	Scott and Hussain (1988) TOC Avg. wt. %
N8987-S	4.43	3.23	4.33	Type II-III	
N8995-S	0.98	0.81	3.10	Type II-III	
N9009-S	0.27	0.34	0.75	Type III	2.50
N9029-S	0.22	2.30	0.54	Type IV (Inert)	

The spectral gamma ray log (Fig. 6-1) also contributes to the evaluation of

hydrocarbon potential in the Jo Mill zone. Uranium occurrence can be an indicator of the

presence of increased organic matter (Klaja and Dudek, 2016). The Jo Mill zone

displays an even distribution of radioactive elements, and due to the stable and

relatively larger amounts of thorium compared to the others, the zone exhibits

characteristics that do not strongly indicate the ideal depositional environment or the

burial conditions necessary for hydrocarbon generation. In general, continental deposits

are identified by a Th/U ratio >7 and marine deposits are identified by a Th/U ratio of <7.

In terms of burial conditions, there is a high probability of reducing conditions if the Th/U

ratio is <2, and a high probability of oxidizing conditions if the Th/U ratio is >7 (Klaja and

Dudek, 2016). The Th/U relationship generally falls between the two reducing and

oxidizing conditions and between the continental and marine deposits, and therefore do

not reveal a specific depositional environment or burial condition. Literature and

previous discussion of the lower Spraberry and the Jo Mill zone reveal that it is a sea

level lowstand, deep-water deposit, which is characterized by terrestrial sediment input

from the north and east of the Midland Basin (Hamlin and Baumgardner, 2012)

(Guevara, 1988).
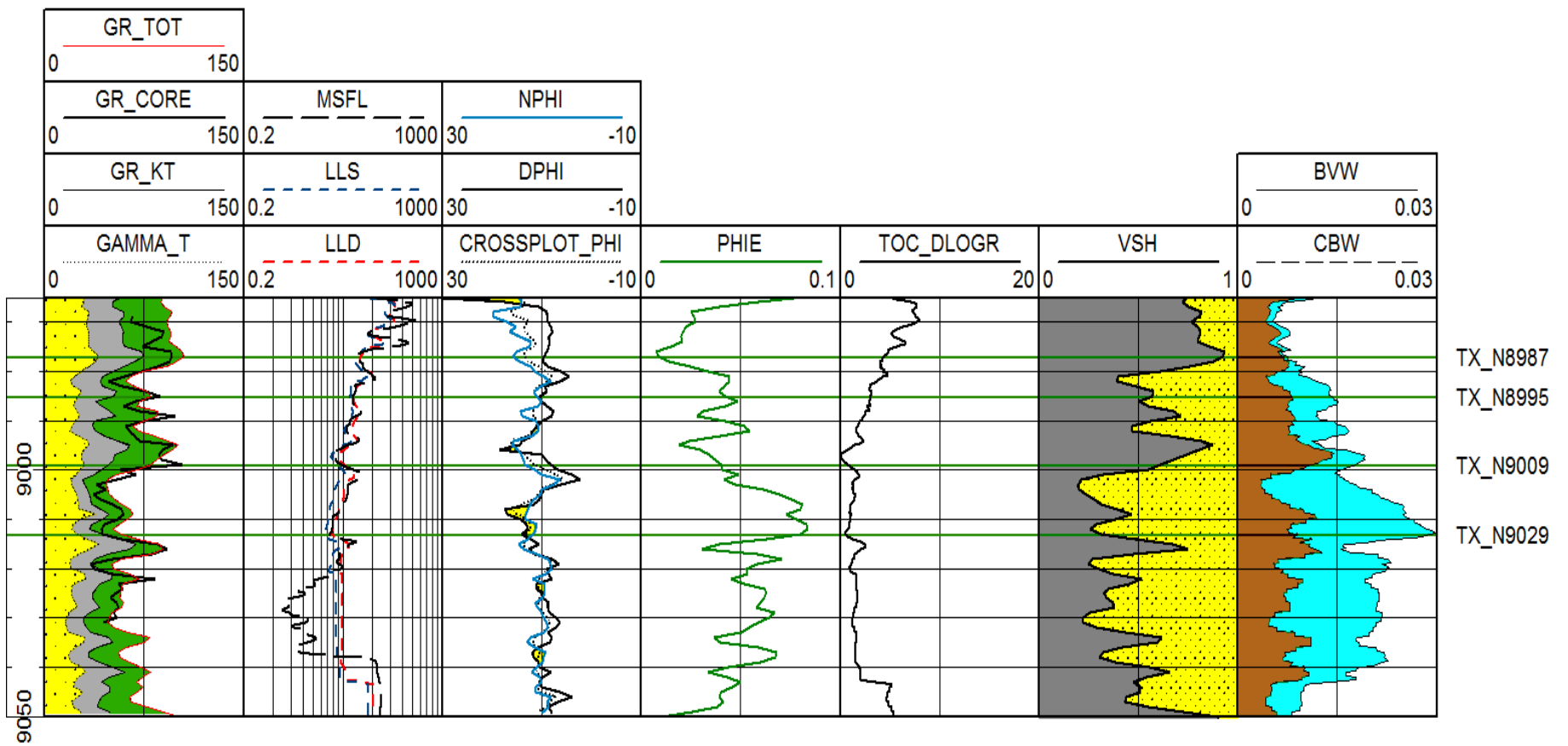
Figure 6-1 Comprehensive log analysis of the Nobles 3202 well.

Porosity and Permeability

To investigate the nature of the porosity and permeability within the Jo Mill zone of the Spraberry formation, the inherent properties such as mineralogy, grain size, and pyrolysis data are evaluated against the measured porosity and permeability from the various methods.

The values obtained are low when considering the Spraberry sandstone and siltstone average matrix porosities and permeabilities of 5-18% and 0.05-3.0 mD (Montgomery, 2000). To analyze the effectiveness of the methods used, the values from each can be compared, as well as the values observed in previous studies (Table 6-2). The helium method yields higher porosity values than the other methods, while the permeability can be evaluated on a similar basis as MICP. The geometric mean of permeability is taken of the first three intrusion inflection points in MICP, which correlate to the parameters and condition thresholds of the helium plug permeability. The difference in permeability values may be due to the difference in direction; while the helium method is unidirectional, the MICP method is multidirectional. The difference in porosity estimation is due, mainly, to factors such as bedding planes and fractures of all sizes that are incorporated in the method sample size. Average fracture apertures in the Spraberry are typically around 0.0025 inches with an average separation lower than 1.62 ft., which contribute to the secondary porosity in the Spraberry. Fracture occurrence also plays a role in the secondary matrix permeability of the rock (Schechter, 1998). The permeability was also found from the fluid imbibition analysis and these values were much smaller, but still within the same order of magnitude, as the MICP permeability results.

The well log analysis (Fig. 6-1) provides for the most contact with the surface area of the formation and thus will provide a different scope of investigation for the Jo Mill zone. One factor that can cause a discrepancy between log porosity values and true porosity values is the matrix density used to calculate the log derived porosity. In this case, the log matrix density used (limestone: 2.71 g/cm^3) is larger than the true density of the formation matrix, which is somewhere in the sandstone range of 2.644 g/cm^3. In this case, the log shows a calculated porosity that is higher than the actual porosity of the formation (Asquith and Krygowski, 2004). The porosity values measured using the density porosity logs were, on average, within ~1% of the values from other methods and followed the same relative pattern (Table 6-2). Considering the overestimation from matrix density differences, the porosity values end up being much closer to the experimentally measured porosities. The low difference in values is largely due to the corrections made for shale volume in the effective porosity curve (Fig. 6-1; Table 6-2).

As the sample size analyzed decreases in surface area, the pore system measured becomes more focused on the rock matrix and the primary porosity established during deposition and early compaction, rather than secondary porosity such as fractures. The MICP method, yielding the lowest overall porosity values, is a powerful tool for characterizing nanometer sized pore systems (Gao and Hu, 2013). The MICP measured cubed samples of 10 mm x 10 mm x 10 mm, which greatly reduced the effect of secondary porosity, and permeability factors observed in the helium and log-analysis methods.

Table 6-2 Comparison of porosity and permeability values from MICP, helium analysis, and well-log analysis.

Sample ID	MICP		Imbibition	Plug Porosity & Permeability		Well-Log Analysis		(Lorenz et al., 2002; Mohan and Leonard, 2013)		(Montgomery, 2000)		Guevara, 1988	
	Porosity (%)	Permeability Geometric mean (µD)	n-decane Predicted k (µD)	Porosity (%)	Permeability (µD)	Porosity (Effective) (%)	Permeability (µD)	Avg. Matrix Porosity (%)	Avg. Matrix Permeability (mD)	Avg. Matrix Porosity (%)	Avg. Matrix Permeability (mD)	Avg. Porosity (%)	Avg. Matrix Permeability (mD)
N8987-S	0.990	49.37	2.288	-	-	0.878	-	6-15	<0.1; <10	5-18	0.05-3.0	<10	<1
N8995-S	2.780	60.53	-	3.314	0.600	4.223	-						
N9009-S	3.890	26.71	2.473	6.125	1.00	4.030	-						
N9029-S	-	-	2.472	-	-	5.340	-						

The spectral gamma ray log (Fig. 6-1) provides insight into the radioactive signature of the Jo Mill zone, and can provide information on fracture presence, and lithologic correlations. The presence of uranium spikes, seen in the space between total gamma ray and the potassium and thorium gamma ray curve (Fig. 6-1), can be an evidence of fractures in the formation. This is because uranium salts are soluble in the formation and can be transported and precipitated after deposition (Asquith and Krygowski, 2004).

When analyzed against the TOC present in the samples, the porosity shows an inverse relationship (Fig. 6-2). The generation of organic matter in the samples, therefore, does not generate enough space to affect the total porosity of the sample. This could be due to the immaturity of the organic matter, or the possible filling of the pore space by cementation or migrated organic matter.
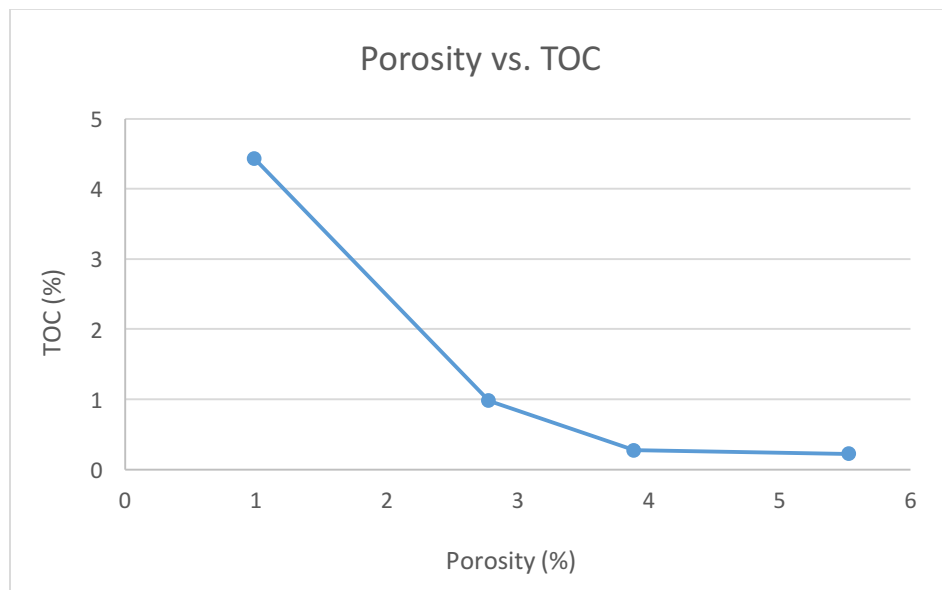
Figure 6-2 Relationship between total porosity and TOC weight percentage.

The factors such as cementation and interstitial clays, which contribute to low permeability and porosity in the Spraberry formation (Montgomery, 2000), can be

compared to the values obtained for the Nobles 3202 Jo Mill zone. The effects of mineralogy on porosity produces a correlation when analyzing the clay and phyllosilicate presence (Fig. 6-3), and the quartz content (Fig. 6-4). The clay percentage measured from XRD, which in this case included the other phyllosilicate minerals, produces an inverse relationship when analyzed with overall porosity from MICP (and well-log analysis for the N9029-S sample). The N9029-S sample displays no phyllosilicate or clay minerals, and has the highest porosity measured from well-log analysis. This relationship suggests the minimizing of overall pore space in the rock when the pore size ranges due to clay content are increasing.
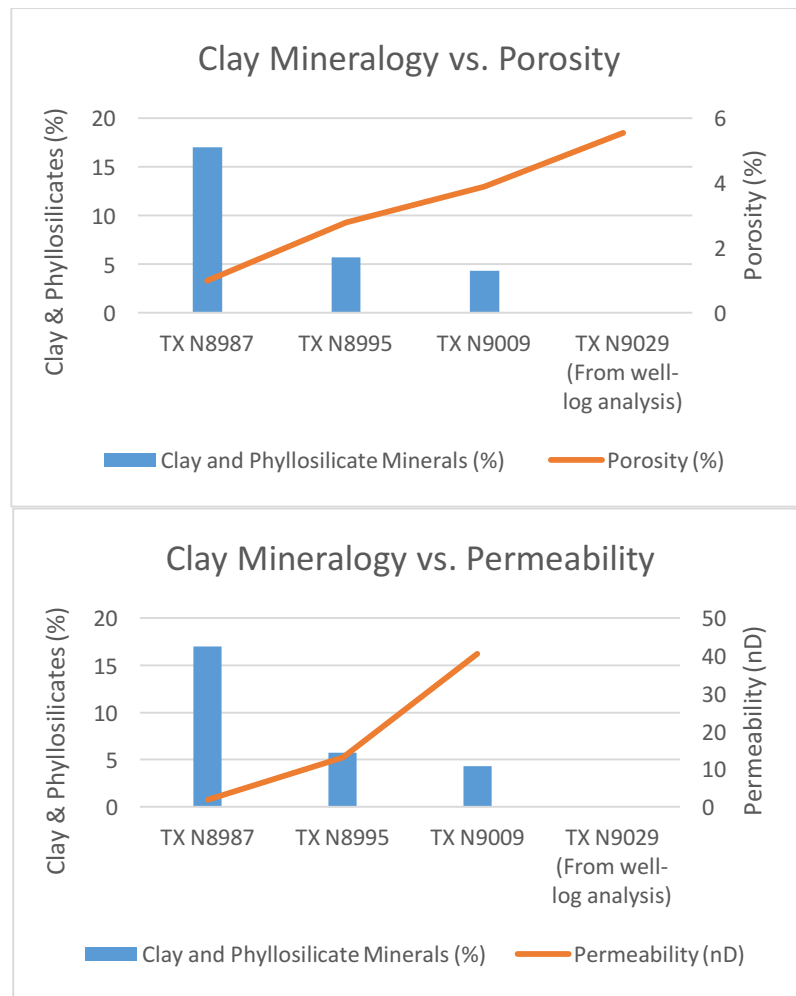
Figure 6-3 Clay mineralogy vs. total porosity and permeability.

82

On the other hand, the quartz content displayed a more direct relationship with the porosity, excluding the N9029-S sample (Fig. 6-4). The N9029-S sample contains the highest amount of carbonate minerals (~20%), when compared with the other samples (≤ 10%). The abundance of carbonate minerals suggests a possible difference in cementation in the N9029-S sample. The N8987-S, N8995-S, and N9009-S samples all contain a dominantly quartz cementation, and therefore exhibit different intergranular frameworks than the possible carbonate cementation of the N9029-S sample. This difference in mineral framework due to different cements could be the cause of the discrepancy in the otherwise direct relationship between quartz and porosity. Another cause of the discrepancy is a change in the source of silica in the N9029-S. Gamero-Diaz et al. (2012) found that there was a direct relationship between porosity and biogenic silica, and an inverse relationship between porosity and detrital silica. The N9029-S sample could display a shift from biogenic sources to detrital sources of silica in the area. Overall, the effects of cementation and clay percentage are in agreement with Montgomery (2000).

The Jo Mill zone is noted for the presence of "sands" in the Lower Spraberry, and with sand, it is often assumed higher porosity and permeability. From the results in the Nobles 3202 well samples, the samples with more quartz and phyllosilicate presence that display the characteristics of a siltstone, do have slightly higher porosity and permeability. However, the overall the porosity and permeability of the samples is very close in value, and this is consistent with the observation from Elkins (1953), in which

the Spraberry sand and shale sections measured about the same porosity and
permeability.
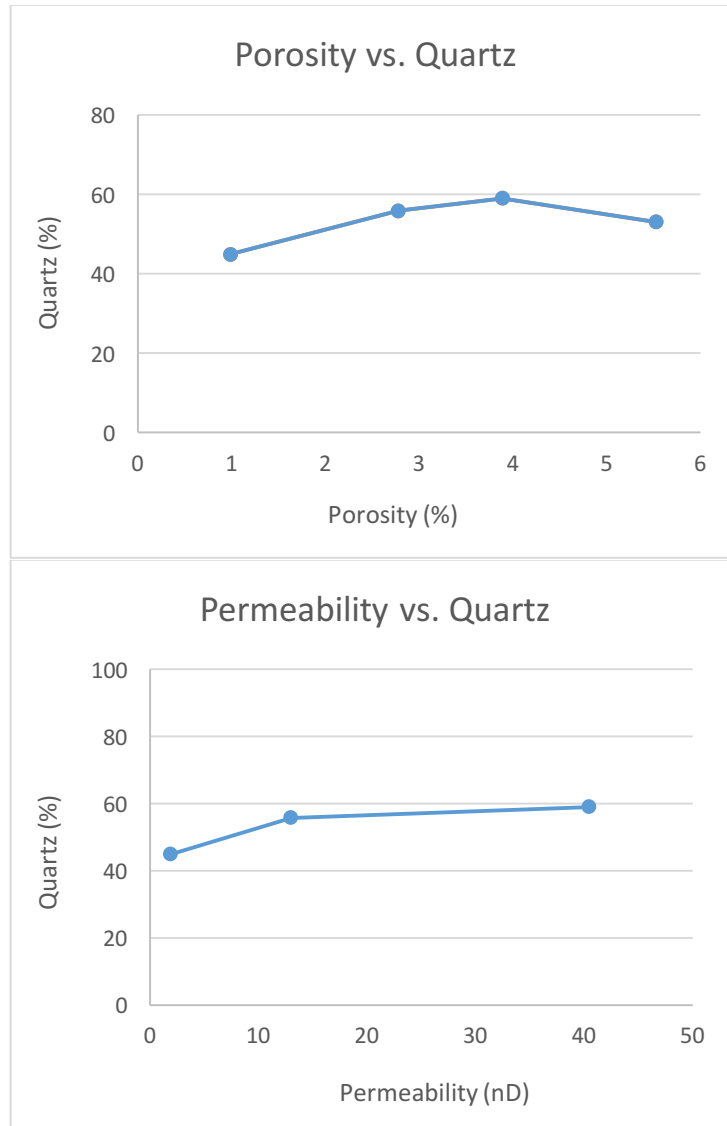
Figure 6-4 Total porosity and permeability vs. quartz percentage.

Pore Size Distribution

The distinction between the pore body and pore throat is investigated with the
MICP method, where the entrapment of mercury (Table 5-5) is quantified during the
extrusion process. The presence of ink-bottle pores, characterized by larger pore

bodies being connected to smaller pore throats, is evident due to the hysteresis curves in Fig. 5-12 (Hu et al., 2017). The N8995-S and N9009-S samples showed much larger percentages of mercury entrapment. Anovitz and Cole (2015) concluded that the pore bodies in shale decrease in size as they approach the pore throat, while coarser grained clastic rock, with more inter-granular pores, has a higher contrast between the size of the pore throat and the pore body. The higher quartz and feldspar weight percentages (Table 5-1), as well as the large contrast between the 50-100nm pore network and the 2.8-5nm pore networks in the N8995-S and N9009-S samples, correlates with the large mercury entrapment in these samples and with the findings of Anovitz and Cole (2015).

The pore size categories as observed by Hu (2016) and Hu et al. (2017) can be further analyzed using the patterns that emerge between the pore size distribution and the measured mineralogical and organic properties of the Nobles 3202 samples. The use of GRI sample size for the N_2 method helps to eliminate the effects of micro-fractures and bedding planes, and closely investigate the matrix properties of the rock. Therefore, the N_2 physisorption method has an upper limit of around 200nm (Kuila and Prasad, 2012). The MICP method results exceed this limit, extending into the 10-50μm range (Table 6-3). Using both of these methods helps to accurately measure the entire range of pore sizes in the samples. Between both methods for pore size distribution, all of the samples display more than 50% of pore volume percentage in the 1-50 nm range, which encompasses inter-clay platelet pores (2.8-5 nm), organic-matter hosted pores (5-10 nm), and intraparticle pores (10-50 nm) (Fig. 5-13).

Between methods, the N8987-S sample yielded similar results, showing the majority of pore volume to be in the 1-10 nm, inter-clay platelet, and organic matter-

hosted pores. The N8987-S sample also showed, from MICP, to have pore sizes in the

micro-fracture range (10-50nm) (Table 6-3). Along with N8987-S, the N9029-S sample

showed some distinctions from the rest in the nitrogen physisorption method, with the

most pore volume percentage in the organic matter and intra-particle hosted pore size

range (Table 6-3). Overall, the MICP method helped shed light on micro-fracture

presence, as well as intra-clay platelet pores. The nitrogen physisorption method

showed an in depth analysis of the inter-clay, organic matter pore volume and the intra-

particle pore size range. One distinction between methods was the amount of inter-clay

pore volume seen in the nitrogen method, while not as prevalent in the MICP method.

Grain size distribution from MICP results, using the Mayer-Stowe method,

yielded results that showed a correlation between the volume of larger grain sizes and

larger porosity and permeability, as well as larger volume percentage of intra-particle

and inter-particle pores. Fig. 5-12, Fig. 5-14 and Table 5-5 show that as the samples

increase in depth from 8987' to 9029', the volume of grains from 1-100μm increases, as

well as the porosity and permeability of the samples and the volume of intra-particle and

inter-particle pores.

Organic matter hosted pores show a direct relationship with the TOC in the

samples (Fig. 6-5), which is in agreement with the pore size range categorization from

Hu, 2016 and Hu et al., 2017. Schieber (2010) categorizes organic matter hosted pores

to be in the range of 10 nm to 100 nm, and pores due to the presence of platy

phyllosilicates to be from 5 nm to more than 1000 nm, however, later states that the

range for phyllosilicates can begin at just a few nanometers. The method Schieber

(2010) used was transmission electron microscopy (TEM) and scanning electron

microscopy (SEM). This allows for the detailed analysis of the mineral and pore

relationship, yet cannot measure the entirety of larger samples sizes. The smaller end

of the phyllosilicate pore size range described by Schieber (2010) is observed in the

Nobles 3202 samples. However, the larger end of the spectrum observed by Shieber

(2010) needs further investigation using TEM and SEM analysis for the Nobles 3202

samples.
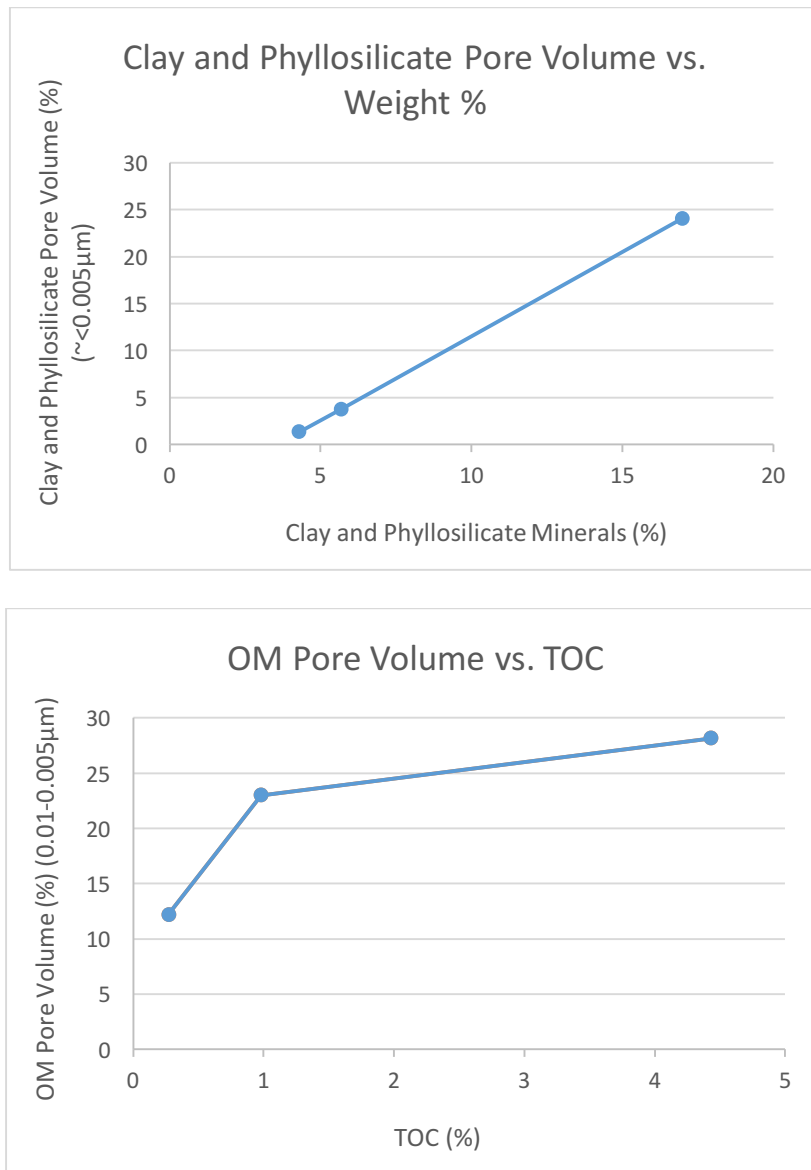
Figure 6-5 Pore size volume vs. mineral and TOC percentages.

Table 6-3 Comparison of pore and pore throat size distributions from N_2 physisorption and MICP analysis.

Nitrogen Physisorption Results

N8987-S		
Pore width (µm)	pore volume (ml/g)	pore volume (%)
0.001-0.005	0.0072	49.58
0.005-0.01	0.0053	36.81
0.01-0.05	0.0020	13.61
0.05-0.1	-	-
0.1-1	-	-
N8995-S		
Pore width (µm)	pore volume (ml/g)	pore volume (%)
0.001-0.005	0.0072	47.85
0.005-0.01	0.0053	35.53
0.01-0.05	0.0025	16.62
0.05-0.1	-	-
0.1-1	-	-
N9009-S		
Pore width (µm)	pore volume (ml/g)	pore volume (%)
0.0025-0.005	0.0111	48.99
0.005-0.01	0.0072	31.88
0.01-0.05	0.0043	19.13
0.05-0.1	-	-
0.1-1	-	-
N9029-S		
Pore width (µm)	pore volume (ml/g)	pore volume (%)
0.0028-0.005	0.0014	24.27
0.005-0.01	0.0023	40.46
0.01-0.05	0.0020	35.27
0.05-0.1	-	-
0.1-1	-	-

MICP Results

N8987-S		
Pore throat width (µm)	Cumulative Intrusion (mm3/g)	pore volume (%)
0.0028-0.005	0.940	24.07
0.005-0.01	1.100	28.16
0.01-0.05	0.940	24.08
0.05-0.1	0.180	4.60
0.1-1	0.267	6.83
1-10	0.230	5.88
10-50	0.249	6.38
N8995-S		
Pore throat width (µm)	Cumulative Intrusion (mm3/g)	pore volume (%)
0.0028-0.005	0.409	3.76
0.005-0.01	2.503	23.01
0.01-0.05	5.738	52.74
0.05-0.1	0.546	5.02
0.1-1	0.814	7.48
1-10	0.665	6.11
10-50	0.205	1.88
N9009-S		
Pore throat width (µm)	Cumulative Intrusion (mm3/g)	pore volume (%)
0.0028-0.005	0.211	1.37
0.005-0.01	1.879	12.18
0.01-0.05	8.837	57.28
0.05-0.1	2.686	17.41
0.1-1	1.276	8.27
1-10	0.381	2.47
10-50	0.157	1.02

Wetting Characteristics and Fluid Movement

The wettability of the Nobles 3202 samples is analyzed by combining the results from the contact angle analysis, the spontaneous fluid imbibition tests, and log analysis. The contact angle results yield that, overall, the samples are weakly oil wet on their surface, except for the N9009-S sample, which has contact angles that are more evenly distributed between the fluids (Table 5-3). The contact angle analysis yielded very low angles for n-decane when compared to the other fluids. This could be due to the differences in surface or edge accessible pores being dominated by organic matter pores or the possible coating of organic matter on the surface. The response to the DI water and the n-decane showed important distinctions in the wetting characteristics of the samples. The steep slopes for the Stage II linear imbibition stage for the n-decane experiment (Table 5-6) shows, in general, the intermediate to well-connected hydrophobic pore networks, while the DI water results showed low to intermediate connectivity of the hydrophilic pore networks.

The N8987-S sample showed the highest contrast between the n-decane slopes and the DI water slopes in Stages II and III, suggesting the dominance of hydrophobic pore connectivity, and low hydrophilic pore connectivity. The N9029-S sample exhibits the closest relationship between the n-decane and DI water slopes in Stages II and III, with the DI water having a Stage II slope of 0.448 and the n-decane having a Stage II slope of 0.692. The N9029-S sample, therefore, exhibits the most connectivity for hydrophilic pore networks, when compared with other samples. The N8995-S and N9009-S samples fell somewhere in between the N8987-S and N9029-S samples, yet still showing relatively higher Stage II slopes for n-decane and lower Stage II slopes for

DI Water. These observations in the Nobles 3202 samples can also be better understood when comparing their mineralogy. The only sample with a recognizable percentage of illite, N9029-S, showed the highest slope for the DI water fluid imbibition. This observation is in agreement with Yang et al. (2017), in that negatively charged clay layers have a tendency to adsorb polar water molecules.

Using the water saturation, the effective porosity, and the shale volume curves, the bulk volume water (BVW) and clay bound water (CBW) curves (Fig. 6-1) are generated. These curves provide another way to analyze the wetting characteristics and the production potential of the reservoir through log analysis. The separation between CBW and BVW represents a portion of moveable water that illustrates a tendency towards mixed wettability in much of the formation. The N8987-S marker exhibits the closest relationship between CBW and BVW, suggesting either the water-wet character of the matrix or the lack of sufficient permeability for the mobility of the water. Most likely, it is the latter, as the imbibition results showed that the N8987-S sample had the largest disparity between the high Stage II slope of the hydrophobic pore networks and the low Stage II slope of the hydrophilic pore networks. The N9029-S sample had the largest Stage II slope for DI water among the samples, and showed the largest separation between the BVW and CBW curves (Fig. 6-1).

Using the three methods for the wettability analysis, the samples exhibit a more rapid behavior of fluid flow through hydrophobic pore networks when compared to the behavior of hydrophilic pore networks, in spite of the presence of moveable water in the log analysis. The imbibition showed that, while the volume of oil-wet pores compared to water-wet pores is not quantified, the oil-wetting pores showed better connectivity than

the water-wetting pores. This weakly-oil wet behavior is slightly different than previously observed weakly water-wet (Mohan and Leonard, 2013) to very weakly water-wet (Montgomery et al., 2000) behavior, yet is consistent with the observation of low displacement efficiency and poor performance of long term water flooding (12-15yr.) seen in the Spraberry (Montgomery et al., 2000). These observations are crucial to the recovery of hydrocarbons in the Spraberry, as the wettability of the rock is responsible for not only the spontaneous imbibition process, but also the brittleness of the rock. Morsy et al. (2014) found that by altering the wettability of Mancos Shale samples by regulating the pH of the water imbibed, oil recovery could be improved by up to 53% and rock hardness could be increased by up to 143%.

Production

When analyzing the production potential of the Jo Mill zone in the Nobles 3202 well, the pyrolysis results can be used to understand the potential for free oil flow. The ratio of free hydrocarbons in the rock (S1) to the TOC produces an oil saturation index (OSI) that is simply a crossover effect when the S1 value exceeds more than 100 mg of oil/g of TOC (Jarvie, 2012). From the OSI (Fig. 6-6), none of the samples displays the oil crossover effect and, therefore, do not indicate the geochemical potential for producible oil. The TOC and pyrolysis experimental results obtained, as well as the secondary kerogen typing and OSI analysis show that, while the Jo Mill samples contain hydrocarbons, they do not exhibit excellent properties in terms of maturity or producibility. The discrepancy between the producibility findings and well production history (Fig. 6-7) is further substantiation of the discrepancy between the organic

91

maturity of the Spraberry shales and the oil present within them (Scott and Hussain, 1988). Stimulation of the Nobles 3202 well spanned from 8,240 ft. to 10,750 ft. which shows the large volume of rock encountered other than the samples herein, and proves the need for further investigation of the other Spraberry shales in the section.

Jarvie (2012) identified three different shale resource systems based on the occurrence and position of organic-rich facies and organic-lean facies, and it is important to note the classification of the Lower Spraberry and the Jo Mill zone when assessing the reservoir quality. The three systems are classified as (1) organic-rich mudstones without open fractures, (2) organic-rich mudstones with open fractures, and (3) hybrid systems that have juxtaposed, continuous organic-rich and organic-lean intervals (Jarvie, 2012). The Spraberry in general, as well as the Jo Mill zone seen in the Nobles 3202 well, can be classified as a hybrid system that has juxtaposed, continuous, organic-rich and organic-lean intervals. The Nobles 3202 samples, even in their scarcity, portray this system; with the N8987-S sample exhibiting higher source rock potential than the other more organic-lean samples seen directly below. This classification helps contextualize the results and understand the role that these organic-lean facies play in reservoir development.

The oil-wetting to mixed wetting characteristics, and the low permeability and porosity of the Nobles 3202 samples are some of the main contributors to lower recovery efficiency in the Spraberry. These factors are observed in the Nobles 3202 samples, and by Elkins (1953), who concluded that recovery of the oil bound in the sand matrix was due largely to the vertical fractures in the formation, even though they make up less than 1% of the void volume.
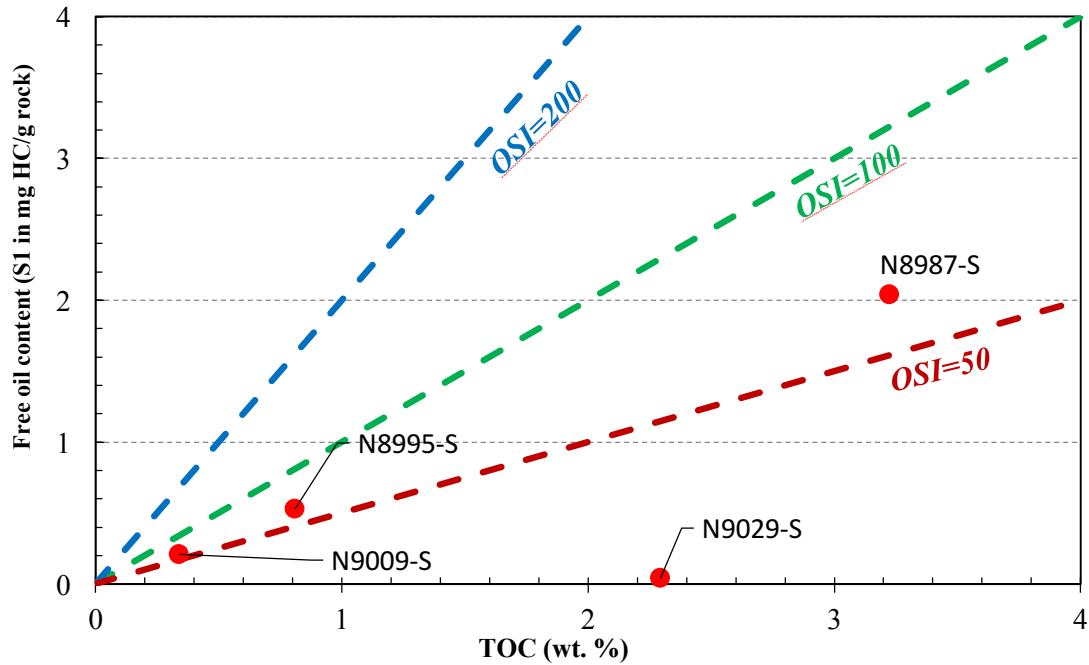
Figure 6-6 Oil saturation index plot based on Jarvie (2012).
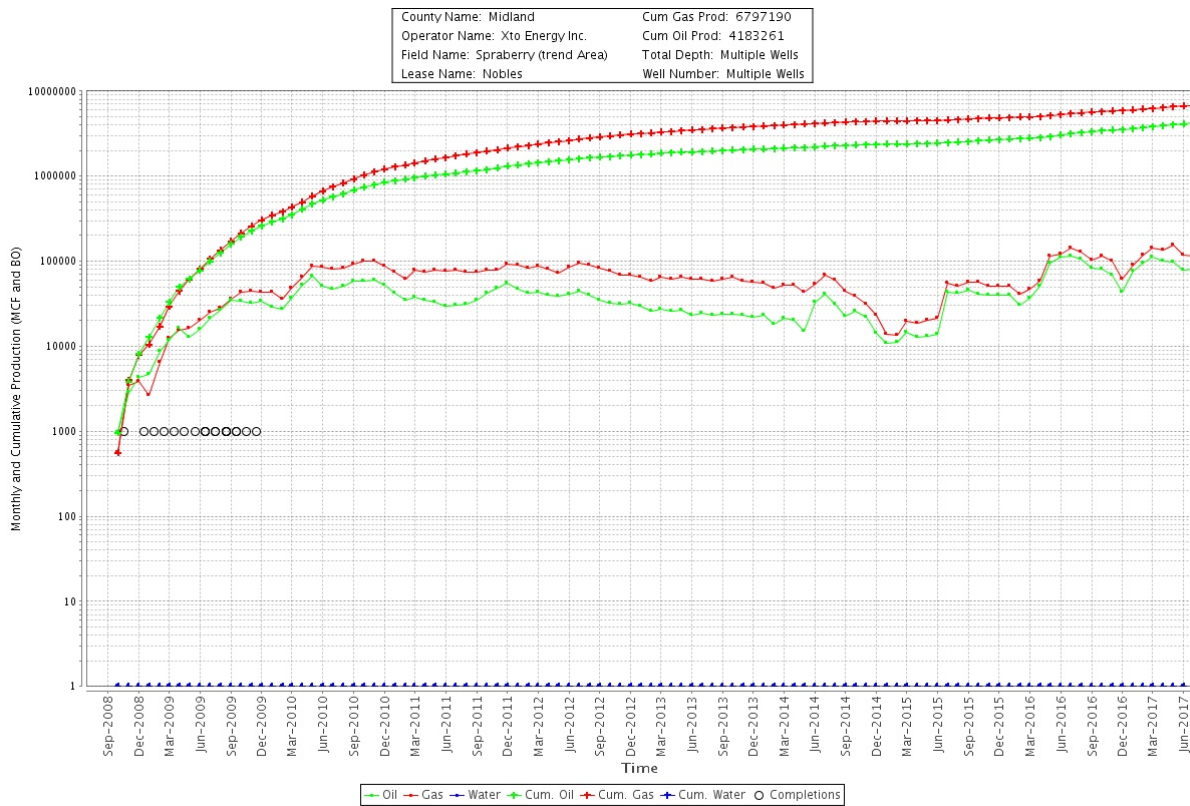
Figure 6-7 Production history in cumulative and total oil and as for the Nobles lease.

Chapter 7. Conclusions and Recommendations

Conclusions

The Jo Mill zone of the Lower Spraberry exhibits important patterns when summarizing the mineralogical and organic properties, as well as the petrophysical properties, such as porosity, permeability, and wettability, seen in the Nobles 3202 samples. There are various conclusions that can be made with respect to each of these properties, and their relationship to one another.

- The Nobles 3202 samples exhibit relatively low porosity (0.8%-6%) between all methods of investigations (MICP, helium, well-log analysis), and low matrix permeability, in the 1-40 nD range (from MICP analysis). The methods showed a slight increase in porosity values when sample size was increased.

- The average pore size range in the samples, between the MICP and helium methods, was in the 0.01µm-0.05µm range, which can be classified as mesoporous (2-50nm).

- Pore volume percentage in pores from 0.01-0.005µm showed a direct correlation with TOC presence, further contributing to the micro-nano pore type categorization for organic matter hosted pores from Hu (2016) and Hu et al. (2017).

- Pore volume percentage in pores <5nm showed a direct correlation with clay and phyllosilicate mineral weight percentage, further contributing to the micro-nano pore type categorization for inter-clay platelet pores from Hu (2016) and Hu and Hu et al. (2017).

- Porosity and permeability values showed a direct correlation with quartz percentage, and an inverse relationship with clay content, further contributing to the main factors of decreased permeability and porosity in the Spraberry found by Montgomery (2000).

- MICP analysis showed a direct correlation between larger Mayer-Stowe grain size distribution and larger porosity and permeability in the samples, as well as an increase in the volume of intra-particle and inter-particle pores.

- Wettability and imbition tests revealed the mixed wettability of the samples within different pore systems. The well-connected pore systems exhibited oil-wet characteristics from the n-decane experiments, while the low connectivity of the DI water tests showed the more constricted water-wet pore networks. This evidence proves useful when evaluating the waterflooding performance seen to plateau in efficiency after roughly 12-15 years (Montgomery et al., 2000).

- TOC and pyrolysis results provided evidence for the onset of maturity and moderate source rock potential for the Jo Mill zone shale sample, while the other samples exhibited little to no source rock potential.

- The low oil saturation index (OSI) showed the lack geochemical potential for producible oil. This is consistent with the observation of varying source rocks (Spraberry and Wolfcamp) for the vertically stratified Spraberry reservoirs (Scott and Hussain, 1988). The findings help classify the zone as a hybrid system that has juxtaposed, continuous organic-rich and organic-lean intervals (Jarvie, 2012).

Recommendations

In relation to the experimental techniques used, the different limits of the experiments, seen in nitrogen physisorption, as well as discrepancies in TOC values between methods, further proves the need for multiple methods of investigation when evaluating rock matrix properties in the nanoscale. Careful attention must be made when determining the source rock potential using the ΔlogR log curve method in regards to the LOM value used, while the wet chemistry technique must be analyzed in regards to the amount of iron (II) (Fe^{2+}) or chromium (Cr) present. Recommendations for further investigation of the Jo Mill zone involve the corroboration of more data in line with the lithological examples of the Nobles 3202 samples. Larger data sets of core samples from similar stratigraphic location must be analyzed to further test the observed relationships between mineralogy and organic properties, with the measured petrophysical properties of the Nobles 3202 samples. This is especially important because of the major vertical stratification of the Spraberry reservoirs, and the ineffectiveness of averaging petrophysical properties such as matrix permeability and porosity outside of the operational units (Guevara, 1988). Continued analysis of the wettability of the Spraberry Formation is highly recommended, as the alteration from weakly-water wet lithology to strongly water-wet lithology could drastically increase recovery efficiency (Morsy et al., 2014). Further investigations into the topographical nature of the pore types in the Jo Mill require additional methods such as field emission scanning electron microscopy (FE-SEM) and Micro-CT scanning.

Appendix A

XRD Standard Operating Procedure

MaximaX XRD-7000: Shimadzu X-ray Diffractometer

Sample Preparation
- Prepare your sample by compacting the sample into the sample holder using a glass slide
- Avoid vertical loading by removing excess sample with the edge of the glass slide
- Attempt to make your sample as flat and homogenous as possible; once this is completed your sample is ready to be analyzed.

Power Operations
- Turn the chiller on by pressing the power button (on the face of the chiller), a green light will illuminate.
    - Allow the chiller to sit for ~20 minutes to adjust to the proper temperature.
- Turn the XRD on by pressing the power button on the left hand side. The green power button will illuminate on the front panel of the XRD.

XRD Calibration:
- Locate and open the [PCXRD] program on the desktop. The main "XRD-6100/7000" panel will display.
- Click the [Display and Setup] icon, a "door alarm check" window will pop up. Follow the prompt to open and close the XRD door, once complete click "Close". An "IOcon" window will pop up with the message "Now Calibration! If ready OK", Click "OK".
- The XRD is officially calibrated and ready to process your sample.

Setting Analysis Conditions:
- To set the processing conditions go to the "XRD 6100/7000" panel.
- Click on the [Right Gonio Condition] icon to open the [Analysis Condition Edit] window
- Click the blue bar under [Measurement Mode: Standard] to open the [Standard Condition Edit] window.
- Most of the settings in the [Standard Condition Edit] window will be preset. Only a few conditions will need to be changed.
- The following general condition settings will work for a wide array of materials.
  It's very important to follow these next steps, double check any settings you change ensuring to follow these guidelines precisely. This will minimize minor mistakes when processing materials and will prevent damage to the detector.
    - Scanning condition: Scan Range (deg) = 2°-70° •
        - Optional Condition: Check the box [Option Enable]
    - Beta Attachment: Control Mode: Rotation
        - Rotation Speed (rpm): 6

- Slit Condition: Slit Conditions are preset, and must be verified on the XRD to ensure the proper slit sizes match the settings listed under the Slit Conditions.
- Checking the Slits:
  - Open the XRD door, on the left side of the XRD is the X-ray tube, the Divergence Slit is attached to the left side of the divergence soller slits.
  - On the right hand side will be the detector arm which contains a set of Scattering soller slits, the Scattering Slit faces the sample (Left) and the Receiving Slit faces the detector (Right).
  - If they are not the same sizes as what is preset in the [Slit Condition] box change the slit's so they do match.
- Standard Slit Settings:
  - Divergence Slit: 1.0°
  - Scattering Slit: 1.0°
  - Receiving Slit: 0.3 mm

- Double check your settings and make sure they are correct, if they are click [OK].
- A [File & Sample Condition Edit] window will display; change the [Group name] to match your destination folder name and change [File name] and [Sample Name] to match your sample name, click [New].
  - Later samples can be created by simply changing the file and sample names and clicking [Modify].
- Click [Close] on the [Standard Condition Edit] window.

Starting the XRD Processing:
- Locate and click the [Right Giono Analysis] icon on the [XRD-6100/7000] panel.
- Your current sample name should appear highlighted blue in the upper portion of the [Right Gonio System: AnalysisCondition Edit Program] window. Highlight your sample and click [Append], this adds your sample to the list in the bottom portion of the window labeled [Entry for Analysis], click [Start]. Your sample should appear in the bottom of the [Right Giono Analysis & Spooler Program] window, click [Start] in this window. This officially starts the analysis process.
  - Indicators for Analysis: A clicking sound will come from the XRD when the locking mechanism on sliding door locks. On the face of the XRD a yellow light should illuminate under [X-RAYS ON].
- Leave all software windows open and allow the XRD to process your sample, this should take ~30 minutes.

Completed XRD Processing:
- A complete peak spectrum should appear in the [Right Giono Analysis & Spooler Program] window upon completion.

- The green [Analyzing!] Box should disappear and the yellow [X-RAYS ON] light should turn off.
- If you have more samples to analyze, continue to run your samples in the same manner listed above.

Opening Peak Profile Spectrum:
- Locate and open the icon for the [MDI jade 9] software on the Desktop.
- Under [file], click [Read], locate the folder [xddat] under [favorites]. Locate the folder where your samples are saved.
- In your folder, each sample should have a [.RAW] file, use this file to open your selected spectrum in the [Jade 9] software.

Identifying Minerals in Peak Spectrum:
It's important to have an educated background on the sample you're analyzing. Knowledge regarding the bulk composition and what you're searching for will greatly reduce the amount of time spent IDing the various peaks in the spectrum.
- Locate the [Find Peaks] icon on the main tool bar next to the [Floppy Disk/Save] icon, this will identify and mark any statistically significant peaks within the spectrum
- Choose a mineral database: At the top of the panel to the right of the spectrum window, there will be a drop down menu choose the [RDB-Minerals] as the database. The RDB-Mineral database should be predominately used to identify most minerals in your spectra.
    - If you cannot find a mineral in the RDB-Minerals database change to the [PDF+4 Minerals] database library, but be sure to change back to the RDB database once the mineral is located.
- Begin searching for minerals based on your pre-existing knowledge regarding the sample. When you identify minerals that fit your peak spectrum hit [Enter] on the keyboard, this process will add the minerals to a compiled list of those minerals which you identified in the spectrum.
- Once you have exhausted your initial hypothetical list of minerals, a helpful tool to use is the [Line Based Search/Match]. Go to the main tool bar and locate [Identify] and select the [Line Based Search] option.
    - This tool will compile a list of minerals by searching a selected PDF database for entries with peaks which are statistical matches for the peaks identified within your spectrum.
    - Settings:
        - [Two-Theta Error Window] max setting should be no more than 0.24%
        - [Top Hits to List] max setting 80
    - Set the parameters and click the blue [Play] icon next to the [X] to run the search and generate a list of possible phases that might fit your spectra. *Note: the line based search should not be used as a primary way to identify the bulk mineral mode of the sample as the software is not consistent when generating phases and will possibly leave out important phases for the spectrum*.

Model Analysis:
- Once all minerals have been ID'd, check that they have been added to the mineral list by pushing [Enter] on the keyboard.
- Click the [%] icon next to the drop-down mineral list located on the toolbar in the middle of the window to begin modal analysis.
  - An overlay will appear with different chart configurations of the modal results, to change the configurations of the chart use the drop down menu in the chart window.
- To view the modal analysis in text format: locate and click the […] icon near the [%] icon. This will list the minerals by name, chemical formula, and the normalized weight percent for each mineral. It will also state if the mineral is a [major], [minor], [trace], or [absent] component in the sample.
- If you would like to remove a mineral from your mineral list at any time, highlight the mineral and press [Delete] on the keyboard. [Absent] phases should be removed from the list by this method.

Analysis Check with Pattern Deconvolution:
- A key indication that the peak spectrum has been fully fitted and identified is by using the [Pattern Deconvolution] tool which automatically runs with the modal analysis.
  - The pattern deconvolution tool will generate a red overlay spectrum on top of the original white spectrum.
  - This process is generating a [Best Fit Profile] composed of the selected mineral standards from the [Mineral PDF database library] with your sample spectrum.
  - If all minerals have been properly identified, then the red deconvolution overlay will match the peak spectra for each peak. If there are peaks that don't have the red deconvolution overlay then those peaks have not been identified.
  - Continue processing your spectrum until your original spectra and the deconvolution spectra match.

Saving Data:
To save your data,
- Go to [file] and [Save], save your data under [Current work as *.SAV]. This will save all analysis as a separate file.

Appendix B

TOC Standard Operating Procedure

The SSM-5000A is a solid sample module which can run two types of analysis, Total Carbon (TC) and Inorganic Carbon (IC), both of which are analyzed by a nondispersive infrared detector (NDIR). By subtracting the IC values from TC values, the Total Organic Carbon (TOC) of a sample can be quantified.

Methods

The TC method
- Uses the electric furnace to heat the combustion tube to 900°C, this allows the carbon combustion oxidation reaction to occur and will yield carbon dioxide which will be analyzed through the NDIR.

The IC method
- Uses the electric furnace to heat the combustion tube to 300°C, and, by adding 0.4 mL of 33% Phosphoric Acid (H_3PO_4), for the carbonate acidification reaction to occur, will yield carbon dioxide which will be analyzed through the NDIR.

Sample Table

a. Open [TOC-V Sample Table Editor] icon and enter your initials

b. Click the [New] icon in the [Sample Table] window

c. Select [SSM-5000A] for the H/W System Settings

d. Select icon labeled [Connect] located on the top row of the window

e. Right click on the number 1 in the Sample Table window and select the [Insert Sample] tab

f. Select [Calibration curve] parameter and search in the Thawspace (T:) Drive for the folder labeled [SSM-5000A_CalCurve].

g. Depending on which type of analysis will be run you will choose the file "TC_CalCurve_SSM5000-A" for Total Carbon or the "IC_CalCurve_SSM5000-A" for Inorganic Carbon.

h. Select [Next], then specify your [Default Sample Name] (e.g., Bob-Shales) and specify your [Default Sample ID] (e.g., LS_1200)

i. Select [Next], then assure the units are in mg/L and leave the [Expected Conc. Range] as is, this number is negligible.

j. Select [Next] and assure your integration time is maxed out at 20:00 min, then select [Finish].

Sample Boat

There are two distinct Tupperware boxes with sample boats depending on which method is used.

a. When using the TC method, use the box labeled "Heat Treated Sample Boats".

b. When using the IC method, use the box labeled "Acid Treated Sample Boats".
  i. Use tweezers to grab a clean sample boat from its respective box and place it on the scale.

  ii. Once the scale has balanced out and a right directional arrow appears on the screen, press the [O/T] button to tare the scale.

  iii. Carefully use the scoopula to scoop a small amount of your sample into the boat. (ideal weight 30-70 mg)

  iv. Once the scale has balanced out, record the weight in mg. This value is used to calculate the concentration of carbon.

Collecting TC

a. Return to the [Sample Table] and click on row number 1 where you inserted your first sample and make sure it is highlighted.

b. Select the [Start] icon located to the left on the second row of the [Sample Table Editor] window.

c. To run your first sample you will be required to name your Sample Table in the Thawspace (T:) Drive (e.g., Bob_Shales_2017_05_01).

d. Next, you will be prompted to enter the weight (mg) of your sample obtained from the balance. DO NOT PRESS START.

e. Carefully open the TC chamber by turning the blue knob counter clockwise and slide the cover over to the right.

f. Place the boat on the metal sample boat holder, make sure it is aligned so that it fits securely in the boat holder.

g. Slid the cover back over the chamber and make sure it is tightened by rotating the blue knob in the clockwise direction.

h. Return to the Enter Sample Amount screen and once the weight is input select [Start].

i. If all background conditions are met, a green [Ready] icon will appear on the top right window and you will be prompted to [Push the sample boat into the measurement position] which you do by pushing the front blue knob all the way forward.

j. To view your measurements, click the second blue icon in your sample window, it has an icon of a graph and a syringe.

k. Once your measurement is complete, you will be prompted to pull the boat back to the cooling position, this is the position located between the [sample change] and [measuring] position on the top panel of the instrument.

l. Once the boat has cooled sufficiently, you will be prompted to pull the boat back to the preparation position.

m. Once the sample boat has reached the [sample change] position, a table with your Total Carbon Concentration will appear.

n. Open the chamber cover by rotating the blue knob counter clockwise and sliding it over to the right. o. *CAUTION* sample boat will still be extremely hot, use the tweezers and carefully pick up the boat and place it on the hot plate.

p. To run another sample for TC analysis, repeat the previous steps as necessary.

Collecting IC

a. Return to the [Sample Table] and click on row number 1 where you inserted your first sample and make sure it is highlighted.

b. Select the [Start] icon located to the left on the second row of the [Sample Table Editor] window.

c. To run your first sample you will be required to name your Sample Table in the Thawspace (T:) Drive (e.g., Bob_Shales_2017_05_01).

d. Next, you will be prompted to enter the weight (mg) of your sample obtained from the balance. DO NOT PRESS START.

e. Carefully open the IC chamber by turning the green knob counter clockwise and slide the cover over to the right.

f. Place the boat on the metal sample boat holder, make sure it is aligned so that it fits securely in the boat holder.

g. Slid the cover back over the chamber and make sure it is tightened by rotating the green knob in the clockwise direction.

h. Return to the Enter Sample Amount screen and once the weight is input select [Start].

i. If all background conditions are met, a green [Ready] icon will appear on the top right window. Although you will be prompted to [Push the sample boat into the measurement position], *WAIT* First, pull up on the white plastic nozzle attached to the bottle of phosphoric acid and allow it to fully inject 0.4 mL of acid into the sample boat so IC reaction can occur.

j. Once the acid has fully injected into the sample boat, push the front green knob all the way forward to the measuring position.

k. To view your measurements, click the second blue icon in your sample window, it has an icon of a graph and a syringe.

l. Once your measurement is complete, you will be prompted to pull the boat back to the cooling position, this is the position located between the [sample change] and [measuring] position on the top panel of the instrument.

m. Once the boat has cooled sufficiently, you will be prompted to pull the boat back to the preparation position.

n. Once the sample boat has reached the [sample change] position, a table with your Inorganic Carbon Concentration will appear.

o. Open the chamber cover by rotating the green knob counter clockwise and sliding it over to the right. p. *CAUTION* sample boat will still be extremely hot and may have residual phosphoric acid, use the tweezers and carefully pick up the boat and place it in the beaker with yellow tape labeled Dilute Phosphoric Acid.

q. To run another sample for IC analysis, repeat the previous steps as necessary.

Saving Results

a. Once all TC and IC sample analysis has been completed you can compile a comprehensive report of all your data to save.

b. Select the [File] tab in the top menu bar, scroll down and select [Print] and scroll to the right and select [Sample Report-All]

c. Ensure that the printer is set to [Microsoft XPS Document Writer] and click [OK]

d. Save your file to the Thawspace (T:) Drive so that you can email yourself the results for use the UTA Box sync cloud service.

e. Once all analyses are saved it would behoove you to open up an MS Excel spreadsheet and create a table of all of your samples with TC in one column and IC in another to easily subtract them to get the sample TOC values. Remember: TOC = TC - IC

References

Abdallah, W., Buckley, J.S., Carnegie, A., Edwards, J., Herold, B., Fordham, E., Graue, A., Habashy, T., Zeleznev, N., Signer, C., Hussien, H., Montaron, B., and Ziauddin, M. 2007. Fundamentals of wettability: *Oilfield Review*, 19(2): 44-61.

Adams, J. E. (1965). Stratigraphic-tectonic development of Delaware Basin. AAPG Bulletin, 49(11), 2140-2148.

Anovitz, L. M., and Cole, D. R. 2015. Characterization and analysis of porosity and pore structures. *Reviews in Mineralogy and Geochemistry*, 80(1): 61–164.

Asquith, G. B., and Krygowski, D., "Log Interpretation." Basic Well Log Analysis, American Association of Petroleum Geologists, 2004.

Blakey, R. 2011. *Regional Paleogeographic Views of Earth History.* Released 2011. Available at https://www2.nau.edu/rcb7/globaltext.html. Accessed February 20, 2017.

Buckley, J. S., Bousseau, C., and Liu, Y. 1996. Wetting alteration by brine and crude oil: from contact angles to cores. *Society of Petroleum Engineers*, 1(03): 341-350.

Chalmers, G. R., Bustin, R. M., and Power, I. M. 2012. Characterization of gas shale pore systems by porosimetry, pycnometry, surface area, and field emission scanning electron microscopy/transmission electron microscopy image analyses: Examples from the Barnett, Woodford, Haynesville, Marcellus, and Doig units. *AAPG Bulletin, 96*(6): 1099-1119.

Cheatwood, C. J. and Guzman, A. E. 2002. Comparison of reservoir properties and development history: Spraberry Trend Field, West Texas and Chicontepec Field, Mexico. Presentation at the SPE International Petroleum Conference and Exhibition held in Villahermosa, Mexico, 10–12 February 2002. SPE-74407-MS.

CoreTest Systems, Inc. 2012. AP-608 Automated Permeameter-Porosimeter: Operator's Manual. Morgan Hill, CA.

Clarkson, C.R., Solano, N., Bustin, R.M., Bustin, A.M.M., Chalmers, G.R.L., He, L., Melnichenko, Y.B., Radlinski, A.P., and Blach, T.P. 2013. Pore structure characterization of North American shale gas reservoirs using USANS/SANS, gas adsorption, and mercury intrusion. *Fuel*, 103: 606-616.

David, S. O., Rodolfo, S. B., Jonathan, S. O., Pasquel, O., and Arteaga, D. 2015. A universal equation to calculate shale volume for shaly-sands and carbonate reservoirs. *SPE Latin American and Caribbean Petroleum Engineering Conference.* SPE-177224-MS.

Davies, M. L. 2012. *The Oil and Gas Resource Play Revolution and how it affects the economy of the Rio Grande region*. Lecture. Available at https://www.slideshare.net/Reenergize/davies-2-a. Accessed August 2017.

Diaz-Campos, M., Akkutlu, I.Y., and Sondergeld, C.H. 2010. New pore-scale considerations for shale gas in place calculations. *SPE Unconventional Gas Conference*, 25 February, Pittsburgh, Pennsylvania, USA. SPE 131772.

EIA (Energy Information Administration). 2017. *Top 100 U.S. Oil and Gas Fields*. Released March 2015. Available at https://www.eia.gov/naturalgas/crudeoilreserves/top100/pdf/top100.pdf. Accessed February 20, 2017.

Ewing, R.P., and Horton, R. 2002. Diffusion in sparsely connected pore spaces: temporal and spatial scaling. *Water Resources Research,* 38(12): 1285.

Gamero-Diaz, H., Miller, C. K., & Lewis, R. 2012. SCore: a mineralogy based classification scheme for organic mudstones. Adapted from AAPG 2012 Southwest Section Meeting, Ft. Worth, Texas, 19-22 May 2012.

Gao, Z., and Hu, Q. 2013. Estimating permeability using median pore-throat radius obtained from mercury intrusion porosimetry. *Journal of Geophysics and Engineering,* 10(2): 1-7.

Gao, Z., and Hu, Q. 2012. Using spontaneous water imbibition to measure the effective permeability of building materials. S*pecial Topics & Reviews in Porous Media - An International Journal*, 3.3: 209-13.

Gharrabi, M., Velde, B., and Sagon, JP. 1998. The transformation of illite to muscovite in pelitic rocks: constraints from x-ray diffraction. *Clays and Clay Minerals,* 46(1): 79-88.

Guevara, E. H. 1988. Geological characterization of Permian submarine fan reservoirs of the driver waterflood unit, Spraberry Trend, Midland. *Bureau of Economic Geology,* 172: 1-44.

Habibi, A., Binazadeh, M., Dehghanpour, H., Bryan, D., and Uswak, G. 2016. Advances in understanding wettability of tight oil formations. *SPE Reservoir Evaluation & Engineering*. doi:10.2118/175157-ms.

Hager, J. 1998. Steam drying of porous media, PhD thesis, Department of Chemical Engineering, Lund Univ., Sweden.

Hamlin, H. S., Baumgardner, R. W. 2012. Wolfberry (Wolfcampian-Leonardian) deep-water depositional systems in the Midland Basin: stratigraphy, lithofacies, reservoirs, and source rocks. *Bureau of Economic Geology*, 277: 1-65.

Handford, C. R. 1981. Sedimentology and genetic stratigraphy of Dean and Spraberry formations (Permian), Midland Basin, Texas. *AAPG Bulletin,* 65(9): 1602-1616.

Heller, R., Vermylen, J., and Zoback, M. 2014. Experimental investigation of matrix permeability of gas shales. *AAPG Bulletin,* 98(5): 975-95.

Hoak, T., Jenkins, R., Ortoleva, P., Ozkan, G., Shebl, M., Sibo, W., Tuncay, K., and Sundberg, K. 1998. Naturally fractured reservoirs: optimized e and p strategies using a reaction-transport-mechanical simulator in an integrated approach. Annual report, 1996--1997.

Hu, Q.H. 2016. September 15. *Nanogeology Constrains Shale Revolution*. Lecture presented at UT Arlington in Texas, Arlington.

Hu, Q. 2016. November 24. *Grain size vs. pore size*. Lecture presented in UTA, Arlington.

Hu, Q.H., Persoff, P., and Wang, J.S.Y. 2001. Laboratory measurement of water imbibition into low-permeability welded tuff. *Journal of Hydrology,* 242(1-2): 64-78.

Hu, Q.H., Ewing, R.P., and Dultz, S. 2012. Low pore connectivity in natural rock. *Journal of Contaminant Hydrology*, 133: 76-83.

Hu, Q.H., Gao, X.B., Gao, Z.Y., Ewing, R.P., Dultz, S., and Kaufmann, J. 2014. Pore accessibility and connectivity of mineral and kerogen phases in shales. Presentation at the Unconventional Resources Technology Conference, Denver, Colorado, USA, 25–27 August 2014. URTeC 1922943.

Hu, Q.H., Zhang, Y.X., Meng, X.H. Li, Z., Xie, Z.H., and Li, M.W. 2017. Characterization of micro-nano pore networks in shale oil reservoirs of Paleogene Shahejie Formation in Dongying Sag of Bohai Bay Basin, East China. *Petroleum Exploration and Development*, 44(5): 720–730.

Jarvie, D. M. 2012. Shale resource systems for oil and gas: Part 2—Shale-oil resource systems, *in* J. A. Breyer, ed., Shale reservoirs—Giant resources for the 21st century: *AAPG Memoir* 97: 89–119.

Jarvie, D. M., Claxton, B., Henk, B., and Breyer, J. 2001. Oil and shale gas from Barnett Shale, Fort Worth Basin, Texas. Lecture presented at AAPG National Convention, Denver, Colorado, June 2001.

Katz A. J. and Thompson A. H. 1986. A quantitative prediction of permeability in porous rock. *Physics Review.* B 34 8179–81

Katz A. J. and Thompson A.H. 1987. Prediction of rock electrical conductivity from mercury injection measurements. *Journal of Geophysical Research,* 92: 599–607.

Kao, C. S., and Hunt, J. R.1996. Prediction of wetting front movement during one-dimensional infiltration into soils: *Water Resources Research*, 32: 55-64.

Kiepsch, S., and Pelster, R. 2016. Interplay of vapor adsorption and liquid imbibition in nanoporous Vycor glass. *Physical Review E*, 93(4).

King, R. R., Jarvie, D., Cannon, D., Smith, T. R., Weldon, D., and Maende, A. 2015. Addressing the caveats of source rock pyrolysis in the unconventional world: modified methods and interpretative ideas. Presentation at the Unconventional Resources Technology Conference, San Antonio, Texas, 20-22 July 2015.

King, H.E., Eberle, A.P., Walters, C.C., Kliewer, C.E., Ertas, D., and Huynh, C. 2015. Pore architecture and connectivity in gas shale. *Energy & Fuels*, 29(3): 1375–1390.

Klaja, J., and Dudek, L. 2016. Geological interpretation of spectral gamma ray (SGR) logging in selected boreholes. *Nafta-Gaz*, 72: 3-14.

Klikenberg, L. J. 1941. Permeability of porous media to liquid and gases. *American Petroleum Institute, Drilling and Production Practice*, 2: 200-213.

Kuila, U., and Prasad, M. 2013. Specific surface area and pore-size distribution in clays and shales. *Geophysical Prospecting*, 61(2): 341–362.

Li, T., Tian, H., Chen, J., and Cheng, L. 2016. Application of low pressure gas adsorption to the characterization of pore size distribution of shales: An example from Southeastern Chongqing area, China. *Journal of Natural Gas Geoscience* 1.3: 221-30.

Lorenz, J. C., and Sterling, J. L. 2002. Natural fractures in the Spraberry Formation, Midland Basin, Texas: The effects of mechanical stratigraphy on fracture variability and reservoir behavior. *AAPG Bulletin,* 86(2): 505-524.

Loucks, R. G., Reed, R. M., Ruppel, S. C., and Jarvie, D. M. 2009. Morphology, genesis, and distribution of nanometer-scale pores in siliceous mudstones of the Mississippian Barnett Shale. *Journal of Sedimentary Research*, 79(12): 848-861.

Loucks, R. G., Reed, R. M., Ruppel, S.C., and Hammes, U. 2012. Spectrum of pore types and networks in mudrocks and a descriptive classification for matrix-related mudrock pores. *AAPG Bulletin,* 96(6): 1071-1098.

Luffel, D. L., Guidry, F. K., and Curtis, J. B. 1992. Evaluation of Devonian shale with new core and log analysis methods. *Journal of Petroleum Technology*, 44(11): 1-192.

Mayer, R. P., & Stowe, R. A. (1965). Mercury porosimetry—breakthrough pressure for penetration between packed spheres. Journal of Colloid Science, 20(8), 893-911.

Milner, M., McLin, R., and Petriello, J. 2010. Imaging texture and porosity in mudstones and shales: Comparison of secondary and ion milled backscatter SEM methods. Presentation at the Canadian Unconventional Resources and International Petroleum Conference, Calgary, Alberta, Canada, October 19–21, 2010.

Mohan, K., and Leonard, P. A. 2013. Evaluating EOR techniques in the Spraberry. Unconventional Resources Technology Conference, Denver, Colorado, 12-14 August 2013: pp. 1855-1862.

Montgomery, S. L., Schechter, D. S., and Lorenz, J. 2000. Advanced reservoir characterization to evaluate carbon dioxide flooding, Spraberry Trend, Midland Basin, Texas. *AAPG Bulletin*, 84(9): 1247-1273.

Morsy, S., Gomaa, A., and Sheng, J. 2014. Improvement of Mancos shale oil recovery by wettability alteration and mineral dissolution. *SPE Improved Oil Recovery Symposium*, SPE-169033-MS.

Njobuenwu, O. D., Oboho, E. O., and Gumus, R. H. 2007. Determination of contact angle from contact area of liquid droplet spreading on solid substrate. *Leonardo Electronic Journal of Practices and Technologies,* 10: 29-38.

Passey, Q.R., Creaney, S., Kulla, J.B., Moretti, F.J. and Stroud, J.D. 1990. A practical model for organic richness from porosity and resistivity logs. *AAPG Bulletin*, 74(12): 1777-1794.

Philip, J.R. 1957. The theory of infiltration: 4. Sorptivity and algebraic infiltration equations. *Soil Science*, 84: 257–265.

RRC (Railroad Commission of Texas). 2017. *Top 50 Current Highest Producing Permian Basin Oil Fields*. Released on March 2013. Available at http://www.rrc.state.tx.us/media/1475/top_50_historical_fields_graph.pdf. Accessed February 16, 2017.

Ruppel, S. C. 2017. Applying sequence stratigraphic methods to mudrock systems: when, where, and how? Presentation at the Fort Worth Geological Society held in Fort Worth, Texas, 10 April.

Schieber, J. 2010. Common themes in the formation and preservation of intrinsic porosity in shales and mudstones - illustrated with examples across the Phanerozoic. *SPE Unconventional Gas Conference*. SPE 132370.

Schumacher, B. A. 2002. Methods for the determination of total organic carbon (TOC) in soils and sediments. *United States Environmental Protection Agency*.

Scott, A. R., and Hussain, M. 1988. Organic geochemistry, source rock potential, and oil-source rock correlation of the Permian Spraberry formation, northern Midland basin, Jo Mill field, Borden County, Texas, *in* B. K. Cunningham, ed., Permian and Pennsylvanian stratigraphy, Midland basin, west Texas: studies 1272 E & P Notes to aid hydrocarbon exploration: *SEPM Publication* 88-28: 33–52.

Scott, K. D., Chu, W., and Flumerfelt, R. W. 2015. Application of real-time bottom-hole pressure to improve field development strategies in the Midland Basin Wolfcamp Shale. *Unconventional Resources Technology Conference*. doi:10.15530/urtec-2015-2154675.

SEPM (Society for Economic Paleontologists and Mineralogists). 2017. The Geology of the Upper Permian. Released on February 13, 2013. Available at http://www.sepmstrata.org/page.aspx?pageid=136. Accessed February 20, 2017.

Shimadzu Corporation. 2014. UniBloc Analytical Balances; AUW-D/AUW/AUX/AUY Series [Brochure]. Japan, 2014.

Sing, K. S., Everett, D. H., Haul, R. A., Moscou, L., Pierotti, R. A., Rouquérol, J., and Siemieniewska, T. 1985. Reporting physisorption data for gas/solid systems with special reference to the determination of surface area and porosity. *Pure & Applied Chemistry; IUPAC*, 57(4): 603-619.

Slatt, R. M. 2006. Stratigraphic reservoir characterization for petroleum geologists, geophysicists, and engineers. Cubbit J. (Ed). Handbook of petroleum exploration and production No. 6 Elseveir, Amsterdam.

Sloss, L.L. 1988. Sedimentary cover, North American Craton, U.S. v. D-2, Boulder, CO, USA, *Geological Society of America*.

Thyne, G. 2013. A review of the measurement of wettability. *Science Based Solutions, LLC*, 2013: 1-35.

Tissot, B. P., and Welte, D. H. 1978. Petroleum Formation and Occurrence. Second Edition. Springer-Verlag, Berlin, Heidelberg, New York.

Tokunaga, T. K., and Wan, J. 2001. Surface-zone flow along unsaturated frock fractures. *Water Resource Research*, 84: 257-264.

Tyler, N., Gholston, J. C., and Guevara, E. H. 1997. Basin morphological controls on submarine-fan depositional trends, Spraberry Sandstone, Permian Basin, Texas. *Bureau of Economic Geology,* University of Texas at Austin, 97(6): 1-43.

Sing, K.S.W., Everett, D.H., Haul, R.A.W., Moscou, L., Pierotti, R.A., Rouquerol, J., and Siemieniewska, T. 1985. Reporting physisorption data for gas solid systems with special reference to the determination of surface-area and porosity (recommendations 1984), *Pure Applied Chemistry* 57(4): 603-619.

Washburn, E.W. 1921. Note on a method of determining the distribution of pore sizes in a porous material. *Proceedings of the National Academy of Sciences*, 7: 115-116.

Yang, R., Hao, F., He, S., He, C., Guo, X., Yi, J., Hu, C., Zhang, S, and Hu, Q. 2017. Experimental investigations on the geometry and connectivity of pore space in organic-rich Wufeng and Longmaxi shales. *Marine and Petroleum Geology, 84, 225-242.*.

Yang, R., Guo, X., Yi, J., Fang, Z., Hu, Q., and He, S. 2017. Spontaneous imbibition of three leading shale formations in the Middle Yangtze Platform, South China. *Energy & Fuels*, 31(7): 6903-6916.

Yang, L., Ge, H., Shen, Y., Ren, K., Sheng, M., Gao, Z., Qin, X. and Su, S. 2015. November. Experimental research on the shale imbibition characteristics and its relationship with microstructure and rock mineralogy. In *SPE Asia Pacific Unconventional Resources Conference and Exhibition*.

Zdravkov, B., Čermák, J., Šefara, M., & Janků, J. 2007. Pore classification in the characterization of porous materials: A perspective. *Central European Journal of Chemistry*, 5(4).

Biographical Information

Ben Rogers was born in Dallas, TX and raised in Frisco, TX where he attended Legacy Christian Academy. He was actively involved in athletics and academics until senior year, when he made the decision to study geology at Oklahoma State University (OSU) in the fall of 2010. Ben was involved in both social and academic organizations throughout campus, including the student chapters of AAPG and GSA at OSU. During his undergraduate studies, Ben worked as a geology intern for Netherland Sewell & Associates, Inc. in Dallas, TX. Upon graduation from OSU in 2014, Ben worked as a logging geologist for Horizon Well-Logging, LLC from 2014-2015. Ben plans to continue in geology and the oil and gas industry upon completion of his M.S. at the University of Texas at Arlington.